Dissertation presented
as a partial requirement for the degree of
Doctor of Science

# Measurement of Muon Neutrino Quasi-Elastic-Like Scattering on a Hydrocarbon Target at $E_\nu \sim 6$ GeV

Mateus F. Carneiro

Advisor:
Hélio da Motta Filho

Centro Brasileiro de Pesquisas Físicas

Rio de Janeiro, August 2016

*To my Mom and Dad*

# Acknowledgements

# Abstract

The MINER$\nu$A Experiment (Main Injector Experiment $\nu$-A interaction) is a highly segmented detector of neutrinos, able to record events with high precision using the NuMI Beam (Neutrino Main Injector) at the Fermi National Accelerator Laboratory. In this thesis, we present the first measurement of the charged current quasi-elastic-like $\nu_\mu$ interaction on polystyrene scintillator (CH) in the MINER$\nu$A detector at neutrino energies around 6 GeV. The dataset used was taken between 2013 and 2014 with a total of $1.17 \times 10^{21}$ protons on target. The interactions were selected by requiring a negative muon, a reconstructed and identified proton, no michel electrons in the final state (in order to get rid of soft pions decaying) and a low calorimetric recoil energy away from the interaction vertex. The final measurement reported is a differential cross section in terms of the muon quadratic transfered energy $Q^2$.

# Contents

# List of Figures

# List of Tables

# Glossary

**CCQE** Charged-current quasi-elastic scattering, when a neutrino scatters from a nucleon and exchanging a W boson. This turns the neutrino into a charged lepton (a muon, for our $\nu_\mu$ beam) and a neutron into a proton or vice versa: $\nu_\mu + n \to \mu^- + p$ or $\bar{\nu}_\mu + p \to \mu^+ + n$

**Charged-current** Any interaction wherein a neutrino exchanges a W boson, converting into its partner charged lepton.

**Cross talk** Current in a given channel can induce a small amount of current in the neighboring channel. The *weave* is used to protect us from false readings due to cross talk.

**DAQ** The system that receives raw data from the detector and stores it to disk.

**DIS** Deep inelastic scattering - occurs at high $Q^2$, where the neutrino scatters off a constituent quark in the nucleon, breaking it apart.

**Downstream** Further along the beamline, away from the target; MINOS is downstream of MINERvA.

**ECAL** Lead electromagnetic calorimeter downstream of the fiducial tracker volume and in the inner part of the outer detector. Designed to stop electromagnetic showers so that their energy can be measured.

**ECL** Electronic Control-room log, also known as Minerva Electronic Logbook. Used to log all shift tasks, hardware changes, or anything else that might affect the detector or data-taking.

**Electromagnetic calorimeter** See *ECAL*

**FEB** Electronics board attached on top of a PMT (one FEB per PMT) that outputs the signal from the PMT.

**Fiducial volume** The central scintillator tracker part of the detector.

**Final-state interaction** When an interaction with a nucleus knocks out a nucleon, this nucleon can re-interact with other particles in the nucleus. This is known as a final-state interaction or FSI.

**Frame** HCAL equivalent of a module. One frame per module.

**Front-End Board** See *FEB*

**FSI** See *Final-state interaction*

**GAUDI** The C++ framework used to run our production and analysis jobs. Configured

using options files, which live in Tools/SystemTests. Run using Gaudi.exe or SystemTestsApp.exe, to which you pass an options file - that file includes a list of algorithms you want to run, as well as various configuration parameters.

**GEANT** The program used to create our detector simulation

**GENIE** Our Monte Carlo generator

**HCAL** See *Hadron calorimeter*

**Hadron calorimeter** Iron calorimeter on the downstream and outside parts of the calorimeter. Designed to stop hadrons so that all their energy will be deposited and can be measured by the

**Horn** Parabolic magnets used to focus positive or negative pions (depending on current direction) produced when the proton beam collides with the beam target. These pions will decay to create our neutrino beam (they also create muons, which are filtered out by rock).

**ID** The inner detector, with respect to the beamline, including the scintillator tracker, nuclear targets, and downstream calorimeters.

**Inner detector** See ID.

**Michel electron** The electron produced when a muon decays at rest.

**Module** In the inner detector, a module consists of two planes of scintillator strips: one in the U or V direction, and one in the X. The U,V and X configurations are all at 60 ° to each other.

**Muon monitor** Four muon monitors are located upstream of the

$\nu$ Energy of the incoming lepton minus energy of the outgoing lepton. Also the symbol for a neutrino.

**Nuclear target** Passive materials interspersed between the active scintillator planes in the downstream part of the detector. MINERvA has graphite, lead, iron, water and liquid helium targets. Some planes are divided into sections of C, Pb and Fe.

**OD** the outer detector, around the sides of the fiducial tracker region.

**Outer detector** See *OD*

**Photoelectron** When light from the detector's optical fibers arrives at the PMT, it hits a photocathode to produce photoelectrons via the photoelectric effect.

**Photomultiplier tube** (*PMT*)s receive light from the detector's optical fibers, which hit a photocathode to produce electrons. This signal is then amplified (typical gain is around 500,000) to produce the output signal. MINERvA has around 500 PMTs, each with 64 channels.

**Plane** Hexagonal sets of parallel scintillator strips that make up the detector. Arranged in X, U, or V configurations, which are at 60° to each other and all (almost) at right angles to the beam.

**Playlist** A list of MINERvA runs/subruns that correspond to a specific detector config-

uration. Analyses will typically process data from one or more playlists, depending on what the analysis is looking for (for example, an antineutrino analysis will look at a playlist of data taken in antineutrino mode).

**PMT** See *photomultiplier tube*

$\mathbf{Q}^2$ The square of the four-momentum transferred to the nucleus in a neutrino interaction. This is a popular variable for differential cross section measurements, as different interaction mechanisms are favored at different values of $Q^2$.

**Resonant** An interaction that produces an excited state of a nucleon (typically the delta resonance $\Delta_{1232}$). These typically decay to a pion and a nucleon.

**Rock muon** A muon created by a neutrino from the beam interacting in the rock upstream of the detector. Creates a track from the front to the back of the detector. As muons behave as minimum-ionizing particles, these are used for calibration.

**Scintillator** The material used for our tracker, consisting of doped polystyrene. When a charged particle passes through the scintillator, it generates blue light, which is shifted to green by our wavelength-shifting fibers, and travels to our PMTs where it is converted to electrical current.

**Strip** Long, triangular prism of scintillator, used to construct the active part of the inner detector.

**Target** Could refer to a *nuclear target* or the *beam target*.

**Tower** The 6 sides of the HCAL outer detector.

**Veto wall** The most upstream subdetector of MINERvA, used to tag rock muons for helium and target 1 analyses.

**Upstream** Less far along the beam line, closer to the beam target. The veto wall is upstream of the MINERvA detector.

$\mathbf{x}_F$ Feynman x.

# Chapter 1

# Introduction

Since the dawn of times humankind seeks to understand nature; to understand what makes the matter around us; how things are all connected and if there are fundamental components in everything. Particle Physics is the modern version of this same quest. What once was explained as gods playing with creation is now understood as fundamental particles interacting with each other. At first we used our own eyes to detect light scattered off of objects and our brains to interpret it. The scale of this search has changed a lot with time and now we manipulate particles to have our own beams scattering in our own man made detector. Results are interpreted by machines that we program to do such. The idea is still the same though: we want to see deeper and deeper into matter and its components.

Neutrinos are the most elusive of this fundamental components of matter. Originally postulated by Pauli in 1930, neutrinos have come a long way from *undetectable particles* to one of the main players in the game of understanding nuclear and particle physics. Neutrino experimental physics is known mostly as trying to understand neutrino properties since there are, still, a great number of questions unanswered from flavor oscillation to CP violation or even the origin of its mass.

To find new physics one needs to have the better possible understanding of neutrino cross sections with hadronic matter. This understanding is important not just to aid neutrino oscillation experiments but also to comprehend how much we know about the nucleus itself. The MINER$\nu$A experiment is a collaboration created and designed to study neutrino cross sections. This thesis describes how we achieve such goal for the Charged Current Quasi Elastic (CCQE) channel.

Chapter 2 introduces the relevant neutrino physics theory. Chapter 3 explains all the relevant concepts and components of the MINER$\nu$A detector. Chapter 4 shows how we use Monte Carlo distributions to simulate data. Chapter 5 gives a short summary of how we reconstruct and interpret the data collected in the detector. Chapter 6 describes the process of

selecting the signal sample we need for our analysis. Chapter 7 shows step by step the process of cross section measurement as well as the first measurement of the single differential cross section for muon neutrino CCQE-like interaction in the MINER$\nu$A detector in the medium energy NuMI Beam configuration and, finally, Chapter 8 presents the conclusions and future perspectives. Appendix A briefly describes the work done in the experiment.

# Chapter 2

# Neutrino Physics

Cross section measurements are crucial for neutrino oscillation experiments and also provide a probe for studying the structure and behavior of atomic nuclei. In this chapter we introduce the phenomenon of neutrino oscillations, give an introduction to the theory of neutrino-nucleus cross sections and the basic theory of quasi-elastic scattering from a free nucleon.

## 2.1  Neutrino Oscillations

Neutrinos are described in the Standard Model (SM) as massless particles that come in three flavors: the electron neutrino $\nu_e$, the muon neutrino $\nu_\mu$, and the tau neutrino $\nu_\tau$. Each neutrino flavor is characterized by the fact that it is produced in conjunction with its charged lepton partner; the electron, the muon or the tau. All three flavors are electrically neutral, interacting only via the weak interaction. The beta decay of a neutron produces an electron and an electron antineutrino:

$$n \to p + e^- + \bar{\nu}_e \tag{2.1}$$

but it will never produce, for example, an electron and a *muon* antineutrino:

$$n \not\to p + e^- + \bar{\nu}_\mu \tag{2.2}$$

Meanwhile, charged pion decay produces anti-muons or muons, and thus, muon neutrinos or antineutrinos:

$$\pi^+ \to \mu^+ + \nu_\mu \tag{2.3}$$

Because all of the detector technologies that we use to detect particles are based on electromagnetic interactions, none of our detectors can directly observe neutrinos. However we can identify what type of neutrino has interacted in a detector by looking at what charged lepton is created in that interaction. Just as before, a muon neutrino will produce a muon in the final

state, an electron neutrino will generate an electron, and so on. So if we have a neutrino source produced by beta decay we expect it to be a source of electron antineutrinos and, consequently, we expect to see a positron in the final state . If we have a neutrino beam produced by $\pi^+$ decay, we expect it to be a beam of muon neutrinos, so we will be looking for a muon in our final state.

This simple concept of lepton generation number conservation was however, defied by experimental data. Cases were observed where a beam of muon neutrinos produced an electron in the final state, rather than a muon. The only neutrino that can create an electron is an electron neutrino $\nu_e$. The Standard Model strictly forbids a $\nu_\mu$ to interact and produce an electron.

One could theorize an alternative possibility where the $\nu_\mu$ has somehow transformed into a $\nu_e$ on its way to the detector, but this is also forbidden by the Standard Model, at least for massless particles. This oscillatory behavior was proposed by Pontecorvo [1] as a neutrino-antineutrino transition. Although such matter-antimatter oscillation has not been observed, this idea formed the foundation for the quantitative theory of neutrino flavor oscillation, which was first developed by Maki, Nakagawa, and Sakata in 1962 [2], further elaborated by Pontecorvo in 1967 [3] and confirmed by the Super Kamiokande experiment [4]. In 2015 the Super Kamiokande collaboration was granted the Physics Nobel prize for the determination that the relative flux of muon and electron neutrinos generated by cosmic ray interactions in the upper atmosphere had an angular dependence, indicating that the rate at which neutrinos changed from one flavor to another was dependent on the distance they had traveled since creation. This shows that the effect must be something that occurred as the neutrino propagated, rather than at the point of interaction. These so called *oscillations* between neutrino flavors were later observed by a great number of different experiments.

### 2.1.1 Flavor state mixing

Each flavor of neutrino $\nu_l$ is coupled to its equivalent lepton $l$: electron neutrino to electron and so on. In other words, all interactions involving a neutrino involve a particular flavor or "weak interaction" eigenstate. In the case of massive neutrinos though, it's easy to build a theory were freely propagate neutrino states are not these flavour eigenstates. Each one of this different set of states $\nu_m$ have a definite mass. Flavor eigenstates could then be constructed as a linear combination of these individual mass eigenstates:

$$\nu_l = \sum_m U_{lm}\nu_m \tag{2.4}$$

and conversely, one could also express a mass eigenstate as a combination of flavor states:

$$\nu_m = \sum_{l'} U^*_{l'm}\nu_{l'} \tag{2.5}$$

The idea of mixing flavor is not a strange concept in quantum mechanics. In terms of experimental particle physics this was first observed in the quark sector, where small amounts of cross-generational couplings were seen, leading Glashow, Iliopoulos and Maiani [5] to propose that instead of a $d$ quark (mass state), the weak interaction coupled to a combination of $d$ and $s$ quarks, defined by the Cabibbo angle $\theta_C$: $d' = d\cos\theta_C + s\sin\theta_C$. With the discovery of a larger number of quark species, this was extended to produce the CKM (Cabibbo-Kobayashi-Maskawa) [6, 7] matrix combining the mass states into weak interaction flavor states:

$$
\begin{pmatrix} d' \\ s' \\ b' \end{pmatrix} = \begin{pmatrix} V_{ud} & V_{us} & V_{ub} \\ V_{cd} & V_{cs} & V_{cb} \\ V_{td} & V_{ts} & V_{tb} \end{pmatrix} \begin{pmatrix} d \\ s \\ b \end{pmatrix}
\tag{2.6}
$$

The neutrino-sector analogy of the quark-sector CKM matrix is known as the neutrino mixing matrix, or the *Pontecorvo-Maki-Nakagawa-Sakata (PMNS) matrix* [8][9]:

$$
\begin{pmatrix} \nu_e \\ \nu_\mu \\ \nu_\tau \end{pmatrix} = \begin{pmatrix} U_{e1} & U_{e2} & U_{e3} \\ U_{\mu 1} & U_{\mu 2} & U_{\mu 3} \\ U_{\tau 1} & U_{\tau 2} & U_{\tau 3} \end{pmatrix} = \begin{pmatrix} \nu_1 \\ \nu_2 \\ \nu_3 \end{pmatrix}
\tag{2.7}
$$

which we can substitute into the plane-wave wave function for a neutrino propagating through space and time to give

$$
\psi(x,t) = \nu_l e^{ip_\nu x - iE_m t} = \sum_m U_{lm} \nu_m e^{ip_\nu x - iE_m t}
\tag{2.8}
$$

where the energy $E_m$ is related to the neutrino's momentum $p_\nu$ and the mass $M_m$ of the eigenstate by the special relativity relation

$$
E_m^2 = p_\nu^2 + M_m^2
\tag{2.9}
$$

If we assume that (as it is the case for neutrinos) the particle is moving at high speed, close to the speed of light, such that $p_\nu \gg M_m$, we can Taylor expand the energy relation, resulting in

$$
E_m \simeq p_\nu + \frac{M_m^2}{2p_\nu}
\tag{2.10}
$$

For a better notation, we use natural units (where $c = 1$). Using the mentioned approximations the neutrino has a speed $\simeq 1$, so $x \simeq t$, giving

$$
\psi(x) \simeq \sum_m U_{lm} \nu_m e^{-i(M_m^2/2p_\nu)x}
\tag{2.11}
$$

Rewriting the wave function as a superposition of all the flavor states $\nu_{l'}$:

$$
\psi(x) = \sum_{l'} \left[ \sum_m U_{lm} e^{-i(M_m^2/2p_\nu)x} U_{l'm}^* \right] \nu_{l'}
\tag{2.12}
$$

We can then calculate the probability of a muon neutrino to be detected as an electron neutrino after traveling a distance $x$. Each mass eigenstate $m_i$ has a related amplitude in a flavor eigenstate $m_l$. Inverting the relation one can say also that a mass eigenstate that traveled a distance $x$ have an amplitude in a different flavor state. The combination of this two amplitudes gives us the probability of flavor change.

Since we are adding amplitudes rather than probabilities we get a kind of oscillation of probabilities, which are equivalent to the absolute value of the squared amplitudes. Mathematically we can write this as:

$$
\begin{aligned}
P(\nu_l \to \nu_{l'}, x) &= \left[ \sum_{m'} U_{lm'}^* e^{-i(M_{m'}^2/2p_\nu)x} U_{l'm'} \right] \times \left[ \sum_{m} U_{lm} e^{-i(M_m^2/2p_\nu)x} U_{l'm}^* \right] \\
&= \sum_{m} |U_{lm}|^2 |U_{l'm}|^2 \\
&+ \sum_{m' \neq m} Re(U_{lm} U_{lm'}^* U_{l'm'} U_{l'm}^*) \cos\left( \frac{M_m^2 - M_{m'}^2}{2p_\nu} x \right) \\
&+ \sum_{m' \neq m} Im(U_{lm} U_{lm'}^* U_{l'm'} U_{l'm}^*) \sin\left( \frac{M_m^2 - M_{m'}^2}{2p_\nu} x \right)
\end{aligned}
$$

The sinusoidal behavior of the quantity $\frac{M_m^2 - M_{m'}^2}{2p_\nu} x$ leads to a characteristic oscillation length $L_{mm'}$, corresponding to the ratio of the momentum and the difference between the squares of the masses:

$$
L_{mm'} = 2\pi \frac{2p_\nu}{M_m^2 - M_{m'}^2} = 4\pi \frac{p_\nu}{\Delta M_{mm'}^2} \tag{2.13}
$$

Using the simplification above and taking $U$ to be real (which is allowed if we ignore the possibility of CP violation), the oscillation probability is given by:

$$
P(l \to l', x) = \sum_{m} U_{lm}^2 U_{l'm}^2 + \sum_{m' \neq m} U_{lm} U_{lm'} U_{l'm'} U_{l'm}) \cos\left( 2\pi \frac{x}{L_{mm'}} \right) \tag{2.14}
$$

### 2.1.2 Mixing fractions and the PMNS matrix

Oscillation experiments have the power to measure the extend to which the mixing of flavor states occurs. The approximate values of the PMNS matrix are (from [10]):

$$
\begin{pmatrix} U_{e1} & U_{e2} & U_{e3} \\ U_{\mu 1} & U_{\mu 2} & U_{\mu 3} \\ U_{\tau 1} & U_{\tau 2} & U_{\tau 3} \end{pmatrix} = \begin{pmatrix} 0.8 & 0.5 & 0.1 \\ 0.5 & 0.6 & 0.7 \\ 0.3 & 0.6 & 0.7 \end{pmatrix} \tag{2.15}
$$

Several experiments have been playing a role in measuring these matrix elements with higher precision.

We assume that the PMNS matrix is unitary[1]. Since the total probability of a neutrino being in *some* flavor eigenstate must be equal to 1. It is possible to parameterize the mixing matrix with just four parameters: three mixing angles, $\theta_{12}$, $\theta_{23}$ and $\theta_{13}$, and a single phase $\delta_{CP}$. This phase creates an imaginary part in some of the matrix elements, that would indicate the presence of CP violation. Using these parameters, the matrix looks like [11]

$$
\begin{pmatrix} U_{e1} & U_{e2} & U_{e3} \\ U_{\mu1} & U_{\mu2} & U_{\mu3} \\ U_{\tau1} & U_{\tau2} & U_{\tau3} \end{pmatrix} = \begin{pmatrix} c_{12}c_{13} & s_{12}c_{13} & s_{13}e^{-i\delta_{CP}} \\ -s_{12}c_{23} - s_{23}c_{12}s_{13}e^{i\delta_{CP}} & c_{12}c_{23} - s_{23}2_{23}s_{13}e^{i\delta_{CP}} & s_{23}c_{13} \\ s_{12}s_{23} - c_{23}c_{12}s_{13}e^{i\delta_{CP}} & -c_{12}s_{23} - s_{12}c_{23}s_{13}e^{i\delta_{CP}} & c_{23}c_{13} \end{pmatrix} \quad (2.16)
$$

Here, $c_{ij}$ and $s_{ij}$ are shorthand for $\cos\theta_{ij}$ and $\sin\theta_{ij}$, respectively. Neutrino oscillation experiments attempt to determine these mixing angles and phase shift, as well as the mass differences between the different states.

The current best fits for the mixing angles are (from [12] normal ordering values):

- $\theta_{13}/° = 8.50^{+0.20}_{-0.21}$; $\sin^2\theta_{13} = 0.0218^{+0.0010}_{-0.0010}$ from $\bar{\nu}_e$ disappearance at reactor experiments Double Chooz [13], RENO [14] and Daya Bay [15]).

- $\theta_{23}/° = 0.452^{+0.052}_{-0.028}$; $\sin^2\theta_{23} = 0.452^{+0.052}_{-0.028}$, from T2K [16] measurements. It is unknown which quadrant it falls into.

- $\theta_{12}/° = 33.48^{+0.78}_{-0.75}$; $\sin^2\theta_{12} = 0.304^{+0.013}_{-0.012}$ from KamLAND [17] data.

and mass mixing:

- $\Delta m^2_{21} = 7.50^{+0.19}_{-0.17} \times 10^{-5}\ eV^2$ and $\Delta m^2_{31} = 2.457^{+0.047}_{.-0.047} \times 10^{-3}\ eV^2$, also from the global fits at [12].

## 2.2 Neutrino interactions and cross sections

Experiments rely on charged particle detection. It is necessary to understand through which processes neutrinos interact with matter and which particles are created in these processes.

Neutrinos scattering with heavy nuclei can occur in different interaction channels. Figure 2.1, reproduced from [18], shows how processes come into play as neutrino energy $E_\nu$ increases. The plot shows charged-current neutrino and antineutrino scattering cross sections respectively and represents the predictions of the NUANCE neutrino interaction generator [19] for the quasi-elastic (QE), resonant (RES) and deep inelastic scattering (DIS) processes, as well as the total charged-current inclusive cross section. This section points out the importance of the

---

[1]this may not be the case if there is one or more sterile neutrinos. This has not been observed and will not be discussed in this thesis
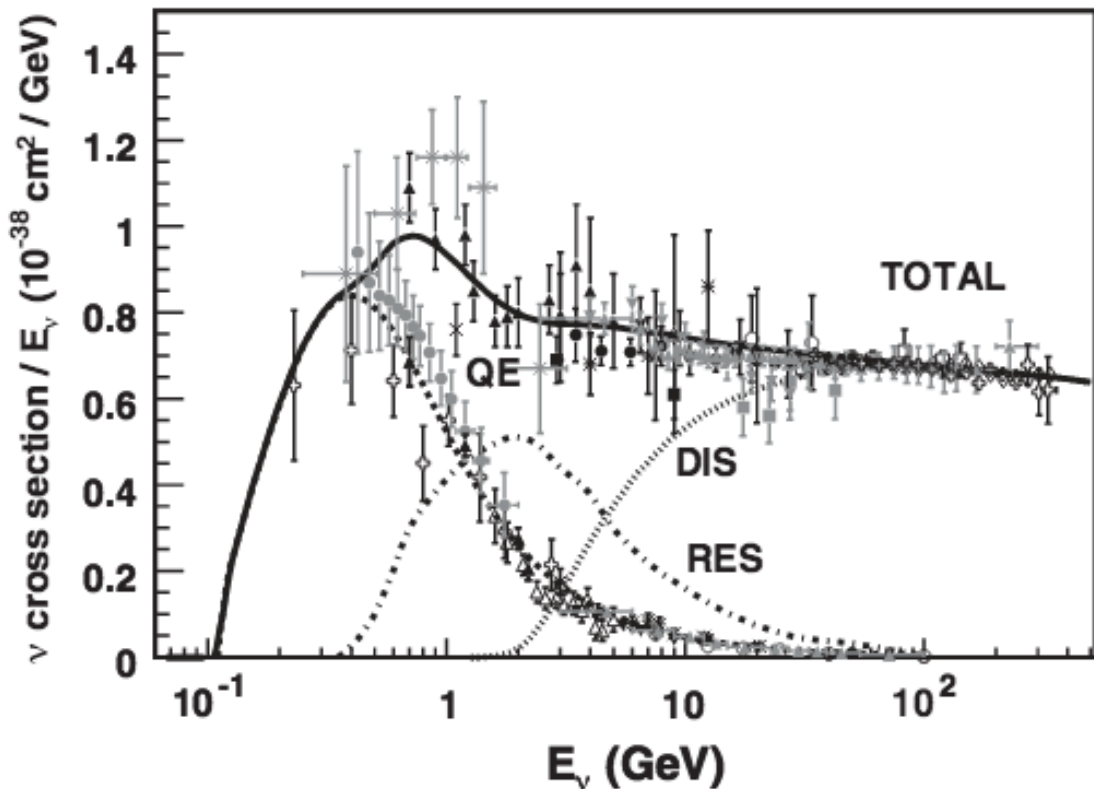
Figure 2.1: Processes contributing to the total charged-current neutrino-nucleon scattering cross section, from [18]. 'QE' refers to quasi-elastic scattering, 'RES' to resonant pion production, and 'DIS' to deep inelastic scattering.

measurement of this cross sections, explains the CCQE mechanism and, briefly, points out the other relevant interaction channels.

## 2.2.1 Quasi-elastic scattering cross-sections

This analysis looks at charged-current quasi-elastic (CCQE) scattering of muon neutrinos on the material of MINER$\nu$A tracker region, which is made up of strips of doped polystyrene scintillator, with a titanium dioxide coating. The composition of the strips is part of the discussion in Chapter 3; the main constituents are carbon and hydrogen atoms, of which there are almost equal numbers.

CCQE scattering, in a simplistic description, refers to cases when the incoming neutrino interacts with a target proton within the nucleus, exchanging a $W$ boson to knock out a neutron, also leaving a negatively charged muon in the final state:

$$\nu_\mu + n \to \mu^- + p$$

In the quasi-elastic case, the neutrino can be considered to be scattered off of the nucleon,

rather than of one of its constituent quarks (this case is known as "deep inelastic scattering" and will be briefly addressed in section 2.2.3).

In the case of pure quasi-elastic scattering, it is possible to reconstruct certain characteristics of the interaction using only the kinematics of the outgoing charged lepton - particularly useful as muons tend to be relatively easy to reconstruct in current neutrino detectors. In particular, the incoming neutrino energy and the four-momentum transfer $Q^2$ can be estimated.

In the process of estimating the scattering amplitudes one must has in mind that nucleons are not point-like particles, but that they have finite size and complex internal structure. The main material used for this thesis' analysis is carbon;therefore, the protons from which neutrinos scatter are frequently bound within a nucleus consisting of twelve nucleons. The nucleons within a nucleus interact with each other in complicated ways that are not fully understood. This can affect the initial state of the target proton in a scattering experiment, as well as modify the final state as the ejected neutron may interact with other nucleons while escaping the nucleus. It is also suspected that incident neutrinos may interact with bound multi-nucleon states within the nucleus. These effects are complicate and not fully understood and can cause significant modifications to the free-nucleon scattering cross section.

**Quasi-elastic neutrino scattering**

Neutrinos, having no electric charge, do not undergo electromagnetic interactions; however, neutrinos do undergo weak interactions what makes it possible for neutral-current elastic scattering to take place via exchange of a Z boson, as shown in figure 2.2.
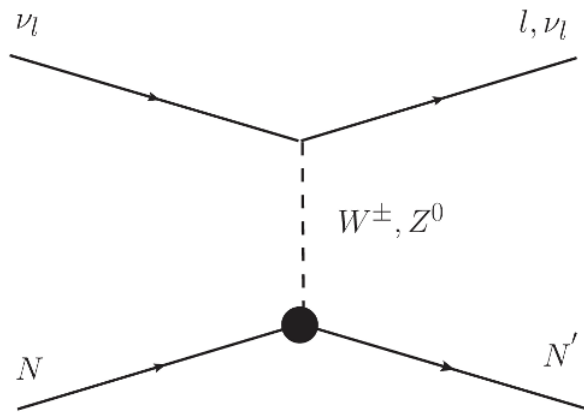


Figure 2.2: Elastic and quasi-elastic scattering of neutrinos from nuclei

Figure 2.2 shows also the charged-current quasi-elastic process for neutrinos. The process produces a charged lepton in the final state, that can be detected and have its charge and momentum analyzed. In this case, the mediating particle is the charged $W$ boson, which causes a neutrino to change to its charged leptonic partner, while simultaneously changing the

flavor of the target nucleon. Neutrinos interact with neutrons, with a $W^+$ being exchanged from the lepton to the hadron :

$$\nu_l + n \rightarrow l^- + p$$

Oscillation experiments have reasons to be interested in CCQE interactions: they dominate at energies in the GeV range, a common energy range for neutrino beams[2]; T2K's beam is centered at 0.6 GeV [21]; MINOS [22] and NOvA [23] are situated, along with MINERvA, in the NuMI beam [24] which, in its low energy configuration, has a mean energy around 3 GeV and now delivers 1-3 GeV neutrinos to NOvA's off-axis detector and a broad-spectrum beam peaking around 6 GeV to MINOS and MINERvA).

We use conservation of energy and momentum to reconstruct both the energy of the incoming neutrino, $E_\nu$, and the negative square of the 4-momentum transferred from the leptonic to the hadronic system, $Q^2$.

$$E_\nu^{QE} = \frac{m_p^2 - (m_n - E_b)^2 - m_\mu^2 + 2(m_n - E_b)E_\mu}{2(m_n - E_b - E_\mu + p_\mu \cos\theta_\mu)} \tag{2.17}$$

$$Q_{QE}^2 = 2E_\nu^{QE}(E_\mu - p_\mu \cos\theta_\mu) - m_\mu^2 \tag{2.18}$$

where, $E_\mu$ is the neutrino muon energy. Muon momentum is represented by $p_\mu$, and $\theta_\mu$ represents the angle between the outgoing muon and the incoming neutrino. As the neutrino mass is negligible (less than 1eV), we take $m_\nu = 0$, meaning $E_\nu = |\vec{p}_\nu|$. The neutron, proton and muon masses are represented by $m_n$, $m_p$ and $m_\mu$ respectively. We recall that $E^2 = m^2 + p^2$ in natural units (where the speed of light is set to 1). These formulae are valid for a quasi-elastic interaction neutrino incident upon a neutron at rest within a nucleus, with a binding energy $E_b$. The interaction produces a negative-charged muon and a recoil proton. Under the quasi-elastic assumption, no energy is lost to the rest of the nucleus - its only effect is to provide the binding energy that lowers the initial state energy of the stationary proton.

Muons typically behave as minimum-ionizing particles in detectors, meaning that their kinematics are relatively easy to reconstruct. This makes this interaction especially appealing for oscillation experiments that wish to compare measured to theoretical cross-sections.

**The Relativistic Fermi Gas model**

According to the the Pauli exclusion principle, two identical fermions cannot occupy identical states. Since protons and neutrons are fermions their number in a given energy state is dictated by Fermi-Dirac statistics:

$$n_i = \frac{1}{e^{\beta(E_i - \mu)} + 1} \tag{2.19}$$

---

[2]Fermilab booster beam, for instance, used by MiniBooNE has a mean energy of 0.5 GeV [20].

where $n_i$ denotes the number of protons or neutrons in a given energy state, $E_i$ is the energy of the state, $\mu$ is the chemical potential and $\beta = 1/kT$ where $k$ is Boltzmann's constant and $T$ is the temperature. In the limit where the temperature goes to absolute zero, this results in a distribution where all energy states are filled up to the Fermi energy $E_F = \mu_{(T=0)}$ while all states above $E_F$ are empty. As temperature rises, the distribution smears, with some states above $E_F$ being filled, and some below becoming empty. We can model the nucleus as a gas consisting of nucleons moving in "Fermi motion", each one having energy and momentum satisfying the Fermi-Dirac distribution.

In the Relativistic Fermi Gas (RFG) model, proposed by Smith and Moniz [25], quasi-elastic scattering from a nucleon in a nucleus is treated as if the incoming lepton scatters from an independent not stationary nucleon that has a momentum consistent with the Fermi distribution. Thus the cross section for scattering off the nucleus is replaced by a coherent sum of cross sections for scattering off of each individual nucleon, with the remaining nucleus (depleted by 1 nucleon) as a spectator.

In this case with a four-momentum transfer $q$, energy transfer $\nu$, nucleon mass $M$, and nucleon initial and final momenta $p_i$ and $p_f$ respectively

$$\text{Initial nucleon kinetic energy, } \text{KE}_i = \vec{p_i}^2/2M$$
$$\text{Final nucleon kinetic energy, } \text{KE}_f = \vec{p_f}^2/2M = (\vec{q}+\vec{p_i})^2/2M$$
$$\text{Energy transfer, } \nu = \text{KE}_f - \text{KE}_i = Q^2/2M + \vec{q}.\vec{p}/M \tag{2.20}$$

We expect the distribution of $\nu$ at fixed $Q^2$ to be centered around $\nu = Q^2/2M$, with a width corresponding to the average momentum in the direction of energy transfer, which is a function of the Fermi momentum. Fitting these distributions yields a measurement of the Fermi momentum, which for carbon-12 has been measured to be $221\pm5\,\text{MeV}$ [26]. This is the value used by our Monte Carlo event generator, GENIE [27].

As mentioned before, protons and nucleons are subjected to Pauli blocking so a struck nucleon cannot be raised to a momentum state that is already occupied; that is, it must have a final-state momentum above $k_F$. This has the effect of, for a given energy transfer, setting a lower limit on the possible energy range of target nucleons for which an interaction is allowed. Therefore, for a pure Fermi distribution where all states up to the Fermi level, and none above it, are occupied, the range of energies allowable to a target nucleon is:

$$E_{max} = \sqrt{k_F^2 + m_N^2}$$
$$E_{min} = \sqrt{k_F^2 + m_{N'}^2} - E_B - \nu \tag{2.21}$$

where $m_N$ is the proton mass, $m_{N'}$ is the neutron mass and $E_B$ the proton binding energy ($30\,\text{MeV}$ in carbon) for a quasi-elastic interaction on a proton. As before, $k_F$ is the Fermi

momentum and $\nu$ the energy transfer. In a real nucleus, in which there is not a strict Fermi momentum cutoff, the Pauli blocking mechanism is more complex [28]. In GENIE, Pauli blocking is implemented via a modification to the Fermi momentum.

**The Llewellyn-Smith model for quasi-elastic cross-section**

We are unable to make a precise analytical calculation of the neutrino-nucleon quasi-elastic cross-section; due to the internal structure of the nucleon, our cross-section depends on nucleon form factors. In 1972, C. Llewellyn-Smith [29] used these form factors to calculate the differential quasi-elastic cross-section. He regroups the form factors in the following way:

$$\frac{d\sigma}{dQ^2}_{QE}\left(\begin{matrix}\nu_l n \to l^- p \\ \bar{\nu}_l p \to l^+ n\end{matrix}\right) = \frac{M^2 G_F^2 \cos^2\theta_C}{8\pi E_\nu^2}\left\{A(Q^2) \mp B(Q^2)\frac{s-u}{M^2} + C(Q^2)\frac{(s-u)^2}{M^4}\right\} \quad (2.22)$$

where:

$G_F$ is the Fermi coupling constant, $1.166 \times 10^{-5} GeV^{-2}$

M is the nucleon mass; $M_{proton} = 938.27\,MeV/c^2$; $M_{neutron} = 939.57\,MeV/c^2$

$\theta_C$ is the Cabibbo angle, $13.04°$

s, u are the Mandelstam variables; $s - u = 4ME_\nu - Q^2 - m_l^2$

$E_\nu$ is the incoming neutrino energy which, in the quasi-elastic hypothesis, can be calculated from the angle and energy of the final state lepton.

$Q^2$ is the square of the four-momentum transferred from the lepton to the hadron which, in the quasi-elastic hypothesis, can be calculated from the angle and energy of the final state lepton.

(Constants from [30].) The coefficients A, B and C are functions of the nuclear form-factors:

$$\begin{aligned}A(Q^2) &= \frac{m_l^2 + Q^2}{M^2}\{(1 + \frac{Q^2}{4M^2})|F_A|^2 - (1 - \frac{Q^2}{4M^2})F_1^2 + \frac{Q^2}{4M^2}(1 - \frac{Q^2}{4M^2})(\xi F_2)^2 \\ &+ \frac{Q^2}{M^2}Re(F_1^*\xi F_2) - \frac{Q^2}{M^2}(1 + \frac{Q^2}{4M^2})(F_A^3)^2 \\ &- \frac{m_\mu^2}{4M^2}[|F_1 + \xi F_2|^2 + |F_A + 2F_P|^2 - 4(1 + \frac{Q^2}{4M^2})((F_V^3)^2 + F_P^2)]\}\end{aligned} \quad (2.23)$$

$$B(Q^2) = \frac{Q^2}{M^2}Re\left[F_A^*(F_1 + \xi F_2)\right] - \frac{m_l^2}{M^2}Re\left[(F_1 - \tau\xi F_2)F_V^{3*} - (F_A^* - \frac{Q^2}{2M^2}F_P)F_A^3\right] \quad (2.24)$$

$$C(Q^2) = \frac{1}{4}\left\{F_A^2 + F_1^2 + \tau(\xi F_2)^2 + \frac{Q^2}{M^2}(F_A^3)^2\right\} \quad (2.25)$$

12

| Experiment | Material | Energy (GeV) | $Q^2$ cut (GeV$^2$) | $M_A$ (GeV) |
|---|---|---|---|---|
| K2K [37] | Oxygen | 0.3-5 | $Q^2 > 0.2$ | $1.20 \pm 0.12$ |
| K2K [38] | Carbon | 0.3-5 | $Q^2 > 0.2$ | $1.14 \pm 0.11$ |
| MINOS [39] | Iron | $\approx 3$ | None | $1.19 \pm 0.17$ |
| MINOS [39] | Iron | $\approx 3$ | $Q^2 > 0.2$ | $1.26 \pm 0.17$ |
| MiniBooNE [40] | Carbon | $\approx 1$ | None | $1.35 \pm 0.17$ |
| MiniBooNE [40] | Carbon | $\approx 1$ | $Q^2 > 0.25$ | $1.27 \pm 0.14$ |
| NOMAD [33] | Carbon | $\approx 3 - 100$ | None | $1.05 \pm^{0.02(stat)}_{0.06(sys)}$ |
| T2K [41] | Carbon | $\approx 1$ | None | $1.26^{+0.21}_{-0.18}$ |
| T2K [41] | Carbon | $\approx 1$ | None (shape) | $1.43^{+0.28}_{-0.22}$ |

Table 2.1: Values of $M_A$ extracted from neutrino-nucleus scattering data

The form factors are associated with different physics processes, and all but $F_A$ are known to a good level of approximation from other processes, like electron scattering. Of these, $F_1$ and $F_2$ are vector form factors, $F_P$ pseudoscalar, and $F_A$ axial vector.

The axial component, represented by the axial form factor $F_A$, is therefore measured through either neutrino-nucleon scattering or pion electro-production. Using a dipole approximation:

$$F_A(Q^2) = \frac{g_A}{(1 + \frac{Q^2}{M_A^2})^2} \tag{2.26}$$

The constant $g_A$, the value of the axial form-factor at $Q^2 = 0$, has been measured through beta-decay experiments [31] to be 1.2756(30)[32], (GENIE uses 1.2670) leaving one free parameter, the axial mass $M_A$.

**Limitations of the RFG model**

Figure 2.3 shows measurements of CCQE $\nu_\mu$ and $\bar{\nu}_\mu$ scattering cross sections on carbon. (MiniBooNE subtracted the $\bar{\nu}_\mu$-hydrogen component of their cross section). The plot includes results from the NOMAD experiment at CERN [33], which operated in the 3-100 GeV range, as well as lower energy results from MiniBooNE [34] at around 1 GeV. In each case, the results were fitted to the Relativistic Fermi Gas model, extracting best fit parameters of the axial mass $M_A$. NOMAD data produced a value of $M_A = 1.05 \pm 0.02(stat) \pm 0.06(sys)$ GeV/c$^2$ in good agreement with the world average. MiniBooNE, however, extracted a value of $M_A = 1.35 \pm 0.17$ GeV/c$^2$ for scattering from mineral oil (CH$_2$) - far above the world average. Table 2.1 (adapted from [35]) summarizes recent measurements of $M_A$, extracted from various experiments' fits to the RFG model.
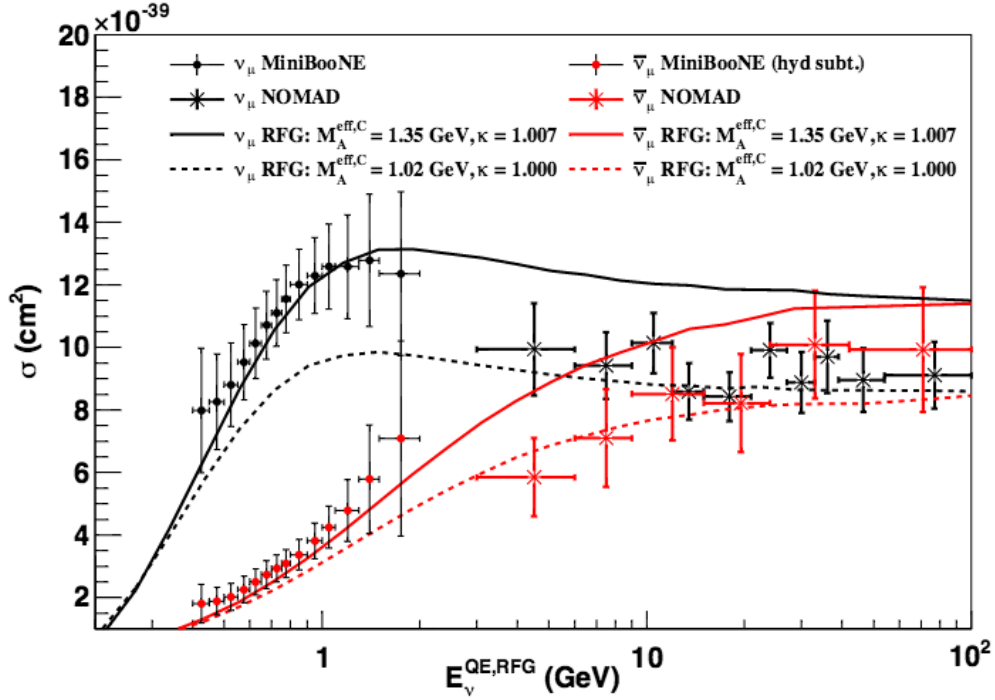
Figure 2.3: Flux-unfolded $\nu_\mu$ and $\bar{\nu}_\mu$ CCQE cross sections per neutron in carbon, as a function of neutrino energy, from the MiniBooNE and NOMAD experiments, compared to the world average and MiniBooNE best-fit RFG predictions. Reproduced from [36]

This indicates that the RFG model is insufficient for describing the behavior of scattering over the complete energy range. There are several likely explanations for this, including deficiencies in the simplistic model of the potential that nucleons experience in the nucleus, as well as the fact that the RFG model does not take account of correlation effects between nucleons.

### 2.2.2 DIS (Deep Inelastic Scattering)

This is the dominant channel at high neutrino energies (see Figure 2.1). The term "deep" is due to the fact that the interaction is produced at the quark level. Figure 2.4 shows a schemtic diagram for DIS interactions, the interaction of a neutrino with a quark component of the nucleon with subsequent several hadronic final states. DIS is characterized by a high momentum transfer $q$. The associated wavelength of the propagator $1/|q|$ is at the size scale of the nucleon constituents.

Neutrinos have the unique ability to probe particular flavors of quarks, hence playing an important role in the extraction of *Parton Distribution Functions* (PDFs), which represent probability densities to find a parton carrying a momentum fraction $x$ at a squared energy scale $Q^2$ [42]. In charged current DIS, neutrinos interact with quarks $d$, $s$, $\bar{u}$, $\bar{c}$ while antineutrinos
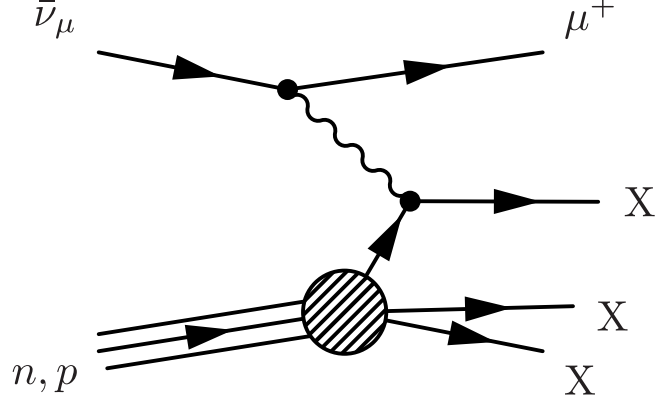
Figure 2.4: A schematic view of the Deep inelastic scattering. A antineutrino interact with a quark component of a nucleon with high energy transfer creating different $X$ hadronic final hadron states.

interact with $u$, $c$, $\overline{d}$ and $\overline{s}$. The main interactions can be expressed in equations as

$$\nu_l + N \rightarrow l^- + X \quad \text{and} \quad \overline{\nu}_l + N \rightarrow l^+ + X \tag{2.27}$$

for charged current interactions,

$$\nu_l + N \rightarrow \nu + X \quad \text{and} \quad \overline{\nu}_l + N \rightarrow \overline{\nu} + X \tag{2.28}$$

for neutral current, where $N = p, n$ and $X$ denotes any final hadron state

### 2.2.3 Resonant scattering

In this interaction process, a resonant state is produced due to the excitation of a nucleon during the interaction process. These excited states decay to their fundamental states producing a combinations of nucleons and mesons. The resonant production in neutrino interactions represents a significant fraction of the total cross section for the few GeV range as seen in Figure 2.1.

This channel is also the main background source for experimental quasi-elastic analyses. At low neutrino energies, these resonance states are composed mostly of $3/2\Delta$ states, which generally decay into a nucleon and a single pion final state (See Figure 2.5).

Resonance reactions in which intermediate resonance states like $\Delta(1232)$ are produced are given as

$$\begin{aligned}
\nu_\mu + p &\rightarrow \mu^- + p + \pi^+ \quad , \quad \overline{\nu}_\mu + p \rightarrow \mu^+ + p + \pi^- \\
\nu_\mu + n &\rightarrow \mu^- + n + \pi^+ \quad , \quad \overline{\nu}_\mu + n \rightarrow \mu^+ + n + \pi^- \\
\nu_\mu + n &\rightarrow \mu^- + p + \pi^0 \quad , \quad \overline{\nu}_\mu + p \rightarrow \mu^+ + n + \pi^0
\end{aligned} \tag{2.29}$$
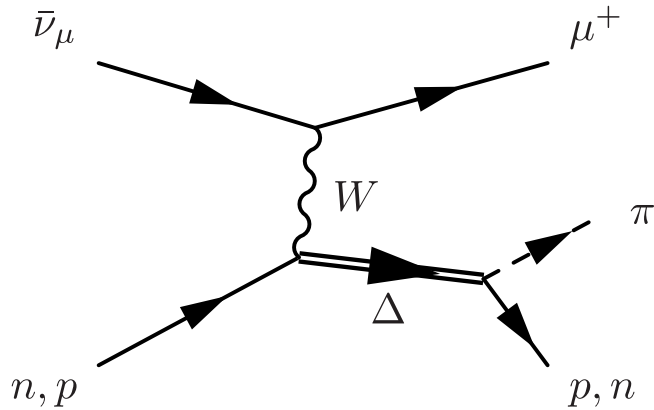
Figure 2.5: Resonant pion production

for charged current and

$$
\begin{aligned}
\nu_\mu + p \rightarrow \nu_\mu + p + \pi^0 \quad &, \quad \overline{\nu}_\mu + p \rightarrow \overline{\nu}_\mu + p + \pi^0 \\
\nu_\mu + n \rightarrow \nu_\mu + n + \pi^0 \quad &, \quad \overline{\nu}_\mu + n \rightarrow \overline{\nu}_\mu + n + \pi^0 \\
\nu_\mu + p \rightarrow \nu_\mu + n + \pi^+ \quad &, \quad \overline{\nu}_\mu + p \rightarrow \overline{\nu}_\mu + n + \pi^+ \\
\nu_\mu + n \rightarrow \nu_\mu + p + \pi^- \quad &, \quad \overline{\nu}_\mu + n \rightarrow \overline{\nu}_\mu + p + \pi^-
\end{aligned}
\tag{2.30}
$$

for neutral current.

The single pion production from baryonic resonances is predicted using the Rein and Sehgal model [43], which works well for high energy neutrino interactions, but are poorly constrained by neutrino data at lower energies (below 2 GeV) [44].

## 2.2.4 FSI (Final State Interactions)

DIS and Resonance processes are of interest to us because, when they occur on nucleons, the final states can mimic those of quasi-elastic interactions. This is because of the phenomenon known as "final-state interactions" or FSI.

Hadrons produced by interactions within the nucleus must traverse the rest of the nucleus in order to reach the final state. In some cases, the hadronic products of the initial interaction will rescatter or be absorbed, altering the kinematics and multiplicity of the hadronic final state. Of particular concern when measuring a quasi-elastic cross section is the case in which a pion is produced, but is then absorbed, leaving a quasi-elastic-like final state of a single muon and neutron.

A recent measurement of MINERvA's quasi-elastic-like neutrino-scintillator scattering cross section demonstrates the importance of modeling FSI effects when measuring CCQE cross sections [45]. Figure 2.6 shows the angle distribution between the neutrino-muon and neutrino-proton plane for fully-reconstructed quasi-elastic-like events ($\nu_\mu n \rightarrow \mu^- p$) on MINERvA's scin-
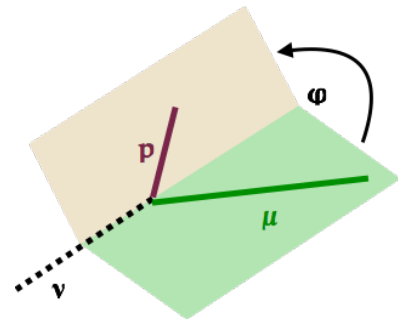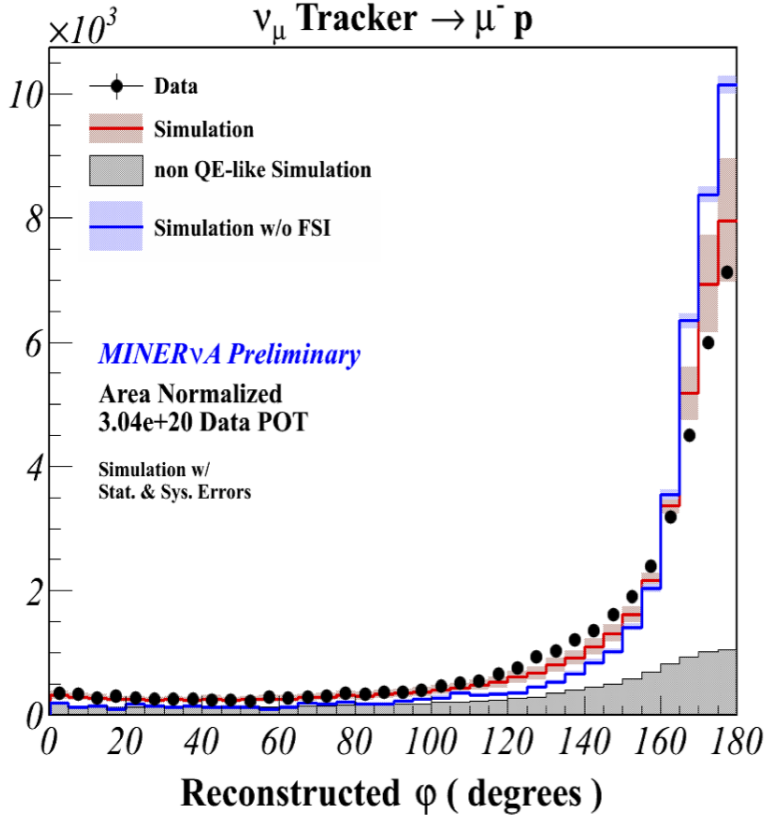
Figure 2.6: The picture in the right side defines the angle $\phi$, the angle beteen the planes defined by the muon and proton tracks. This is a distribution higly model dependent since it carries information of the FSI interactions. Comparison of MINER$\nu$A 's neutrino-scintillator scattering data with simulation with and without FSI effects (from [45]).

.

tillator tracker. This distribution is then compared to the predictions of the GENIE event generator with and without final-state interactions enabled. Each of the simulated distributions is normalized to the area beneath the data distribution; this serves to remove contamination from uncertainties in the measurement of the neutrino flux, allowing the shapes of the distributions to be compared. It can be clearly seen that the data agrees better with the simulation that includes FSI effects; however, the agreement is not exact, indicating that FSI modeling needs to be improved.

## 2.3    Importance of cross section measurements

There's a relative long way from the simple oscillation formula to an estimation of the actual number of events in a neutrino oscillation experiment. Two key pieces of information needed

for this translation are: the initial flux of unoscillated neutrinos and the probability that a neutrino (oscillated or otherwise) will interact within the detector. An accurate cross section model for neutrino scattering from heavy nuclei is vital for experiments to compare their event counts to models' predictions and extract physics information.

The next generation of experiments, from which we can cite DUNE [46] as the most ambitious project in planning phase, will need to keep systematic uncertainties to a minimum in order to meet their physics goals. DUNE has a goal of 2% uncertainty on its measurements [46]. Figure 2.7 shows the time (and therefore operating cost) savings of reducing the uncertainties: it details the exposure needed to measure CP violation for 75% of possible values of $\delta_{CP}$. One can see that the discovery of CP violation with $3\sigma$ significance will take approximately 1000kt-MW-years with their standard reference design if they can achieve 5% uncertainty on the total normalization and 1% on the relative normalization of $\nu_e$ to the other neutrinos (top line of blue hashed area); with $5 \oplus 2\%$ (middle line), it will take 1250kt-MW-years. Thus reducing uncertainty is key to saving time and expense.

The sources of uncertainty come from neutrino flux spectrum, which can be reduced by comparing near and far detector measurements; fiducial volume identification, which is expected be small ($< 1\%$) in such a large detector, energy scale, and interaction models for neutrinos and antineutrinos on nuclei. The goal of the measurement in this analysis is to reduce uncertainty on the interaction models, by constraining them with data from our cross section measurements. T2K currently has 5.3% interaction model uncertainty [10]; to meet its physics goals, DUNE must reduce this to 2%.

Investigating nuclear physics is another important motivation for cross section measurements. Neutrino scattering on free nucleons is well understood (the charged-current quasielastic scattering discussed in this paper was modeled in 1972 by Llewellyn Smith [29], and this model works well for scattering from hydrogen and deuterium). However, in heavy nuclei, interactions between the nucleons in the nucleus affect the scattering behavior. By examining the cross section distributions and comparing them to various models of these nuclear effects, we are able to increase our knowledge of the nature and strength of these behaviors.

The measurement presented in this thesis aim to provide data that can be used to reduce cross section uncetanties, help resolve the data discrepancy described in Section 2.2.1 and provide a deeper understanding of final state interactions as it's done in a broad band neutrino beam in a detector designed for ideal resolution in particle tracking.
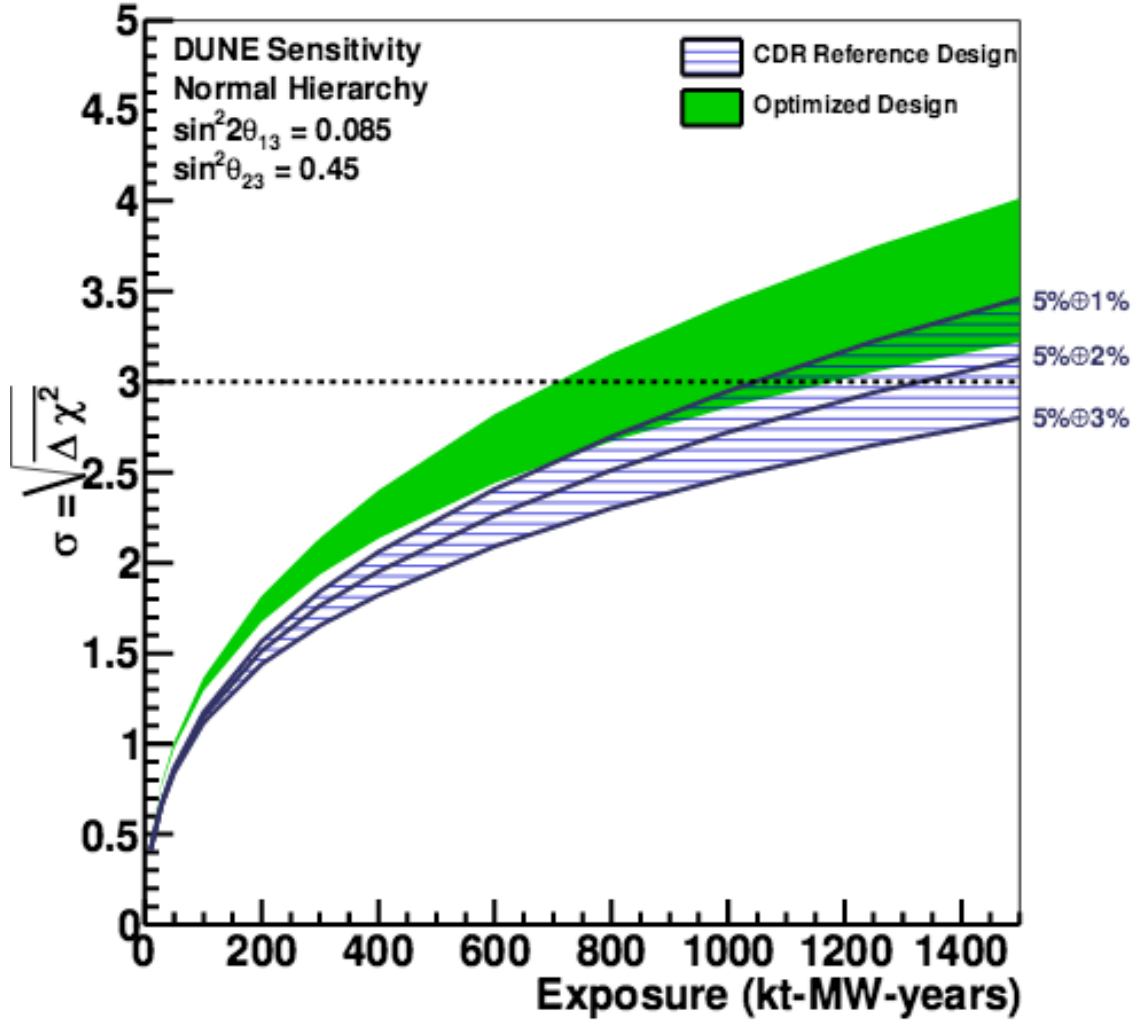
Figure 2.7: Exposure needed for DUNE to measure $\delta_{CP}$ for 75% of possible values of $\delta_{CP}$, with different levels of systematic uncertainty. The blue hashed area shows the sensitivity with the current beam design, with the three lines representing how long DUNE must run with uncertainties from $5 \oplus 3$ to $5 \oplus 1\%$, where the two numbers refer respectively to the uncertainty on $\nu_\mu$ normalization and $\nu_e$ normalization relative to $\nu_\mu$ and the antineutrinos. The dotted line shows the $3\sigma$ confidence level. The green colored area shows an equivalent for a new optimized design. Reprinted from [10]

# Chapter 3

# MINER$\nu$A Experiment

MINER$\nu$A (Main INjector ExpeRiment for $\nu$-A) is a dedicated neutrino-nucleus scattering cross-section experiment situated in the NuMI neutrino beam at Fermi National Accelerator Laboratory (FNAL, or Fermilab), Batavia, Illinois, US. The collaboration is composed by approximately 70 particle and nuclear physicists from 7 countries. The MINER$\nu$A experiment plays an important and potentially decisive role in helping the current and future precision oscillation experiments to reach their ultimate sensitivity. The experiment also uses a variety of target material to study nuclear effects and parton distribution functions (PDFs) .

The NuMI beam provides neutrinos and antineutrinos in the $1 - 20$ GeV range. The MINER$\nu$A detector employs fine-grained polystyrene scintillator for tracking and calorimetry. In addition to the active scintillator target, the detector contains passive nuclear targets of carbon, iron, lead, water, and liquid helium. The MINOS [22] Near Detector sits downstream of the MINER$\nu$A Detector and it is used as muon spectrometer and its magnetized detector provides data on the charge and momentum of muons exiting the back of MINER$\nu$A .

## 3.1   The $\nu_\mu$ at Main Injector (NuMI Beam)

Fermilab NuMI beamline provides an intense flux of either mostly $\nu_\mu$ or $\overline{\nu}_\mu$ to short and long baseline neutrino experiments like MINOS, MINER$\nu$A and NO$\nu$A [47]. NuMI neutrinos are the final decay product of charged mesons, most kaons and pions, generated by the collision of 120 GeV protons (extracted from the Fermilab Main Injector) with a graphite target. Two pulsed magnetic horns focus positive (negative) mesons that will decay to produce $\nu_\mu$ ($\overline{\nu}_\mu$). Figure 3.1 shows NuMI main parts and components. A detailed description may be found in [24] and [48].

During the process of acceeration, protons go through several stages before acquiring the energy of 120 GeV: the LINAC, the booster and the Main Injector. The linear accelerator
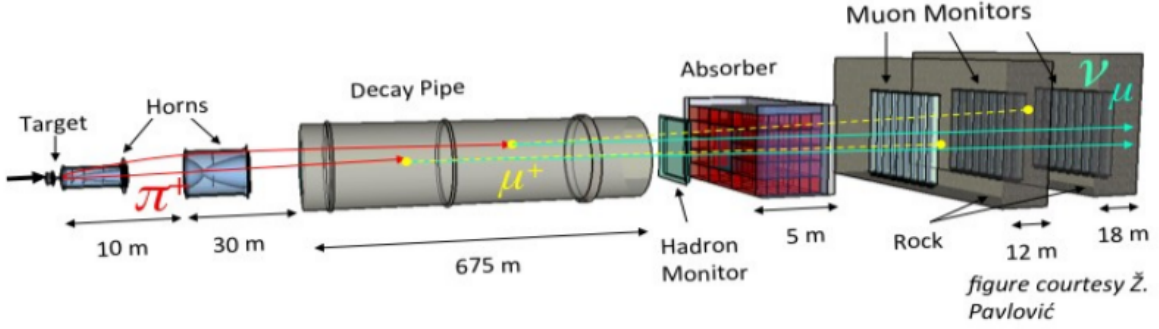
Figure 3.1: NuMI beamline components.[48]

(LINAC) takes the protons up to 400 MeV and sends them to the booster that accelerates them up to 8 GeV, which next send the protons to the Main Injector for the final boost until the 120 GeV target energy. At the final stage protons from the Main Injector are extracted to NuMI target (with a frequency of 0.53 Hz using a single turn extraction). Every 1.9 seconds a 8.4 $\mu s$ spill with about $3.5 \times 10^{13}$ protons is extracted and sent towards a 0.95 m long segmented water cooled graphite target. Around 15 cm prior to striking the target, the proton beam passes through a toroid that measures the number of protons, and the beam profile is monitored to guarantee an appropriate behavior.

Mesons produced in the target are focused by two 3 meter magnetic horns acting as parabolic magnetic lenses that create a toroidal field around 3 Teslas, these are located downstream of the target (see Figure 3.2).

The horns are water cooled and operated by a pulsed $\pm185$ kA current [48] to bend pions and kaons towards the proton beam path. It is possible to vary the current of the horns to make special studies and characterization of the beamline. If the target is moved 2.5 meters away from the horns there will be a change in the momentum spectrum of the focused particles resulting in a higher energy beam. Passing the horns, mesons decay and contribute to the neutrino flux in the MINOS detector cavern.

The decay region is a 675 m long and 2 m diameter cylinder kept filled with helium to minimize interactions. Protons and undecayed mesons still present at this stage at the end of the decay pipe are stopped at a hadron absorber consisting a water cooled aluminum core surrounded by a steel block and an external concrete chamber. The hadron absorber removes all the hadronic content of the beam, leaving only neutrinos and muons. After the hadron absorbers three muon monitors are separated by dolomite rock. The purpose of the muon monitors is measure the muon energy spectrum that can be used to predict the neutrino flux in situ. Between the hadron absorber and the detector hall there is around 240 meters of rock, enough to stop all muons present in the beam, leaving only neutrinos. Figure 3.1 also shows

21
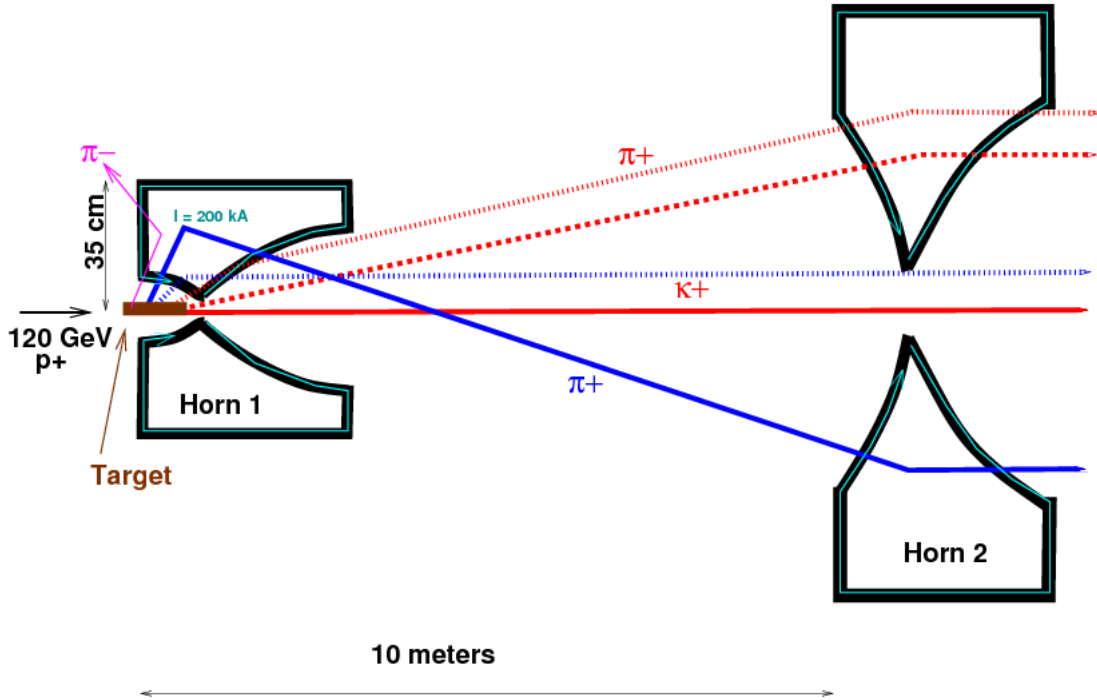
Figure 3.2: Schematic showing positions of the NuMI target, baffle and horns. [48]

the muon monitors and hadron absorbers location in the NuMI beamline.

Figure 3.3 shows the possible energy configurations of the NuMI beam: low energy (LE) and medium energy (ME). Different energies are achieved by changing the distance between the target and the second horn in a movement similar to the lenses of an optical system. Pions and kaons of different momenta are selected and focused in the decay region resulting in different energy spectra. The beamline has been constantly upgraded

The capability of changing the horn makes it possible to focus mesons of the opposite signal, so the NuMI beam is able to produce neutrinos or antineutrinos [1]. The NuMI neutrino beam is delivered to the experimental hall 100 m underground at FERMILAB grounds where the MINER$\nu$A detector is placed just upstream of the MINOS near detector. The beamline is constantly being upgraded to achieve greater intensities.

## 3.2 The MINER$\nu$A detector

The MINER$\nu$A detector is described in detail in [49]; this section summarizes its main features, with particular focus on the components relevant to this analysis. Figure 3.4 shows an schematic view of the MINER$\nu$A detector. It is composed of an inner detector (ID) and an outer detector (OD).

---

[1]This featured is well wanted so experiments can compare neutrino and antineutrino data produced by the
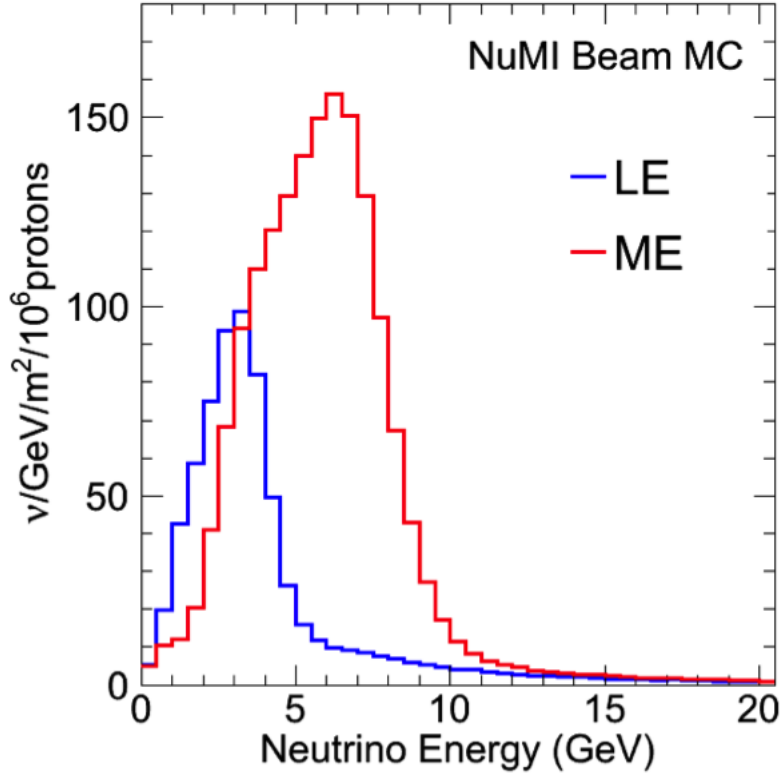
Figure 3.3: The figure show different possible fluxes for different configurations NuMI beam. Flux estimated by a GEANT4 based simulation of the beam line.

The ID consists of active scintillator planes interspersed with passive nuclear targets, followed by a tracking region of pure scintillator, a downstream electromagnetic calorimeter (ECAL), then a hadronic calorimeter (HCAL). The outer detector is mainly composed of a heavy steel frame, interspersed with scintillator bars, which serves both for calorimetry and as a support structure for the detector. Outside of this are the electronics and light collection systems. Upstream of the main detector are a steel shield, veto wall, and a liquid helium target. The MINOS near detector, which serves as a muon spectrometer, is located $2\ m$ downstream of the MINER$\nu$A detector.

### 3.2.1 The Veto wall

The Veto wall consists of alternating planes of steel and scintillator (5 cm steel, 1.9 cm scintillator, 2.5 cm steel, 1.9 cm scintillator) positioned upstream of the detector. This structure is designed to shield the detector from low energy hadrons and tag muons created by neutrino interactions in the surrounding cavern rock (such particles are referred to as *rock muons* in this thesis). These rock muons, if not vetoed, may be misidentified as muons produced in

same source.

23
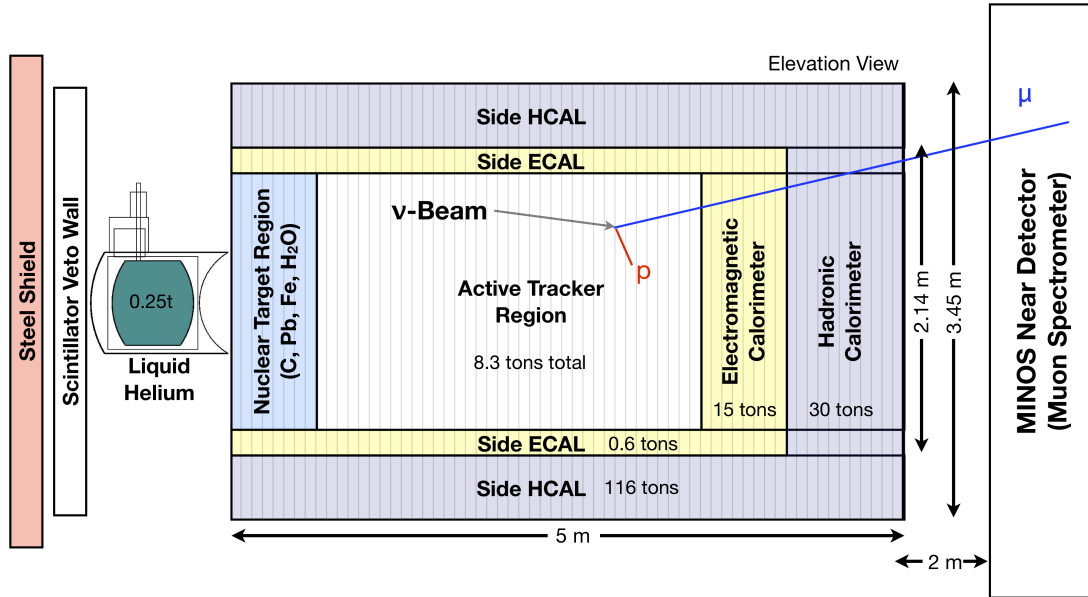
Figure 3.4: Schematic view of the MINER$\nu$A detector.

charged-current neutrino interactions in the first modules of the detector.

## 3.2.2 The Nuclear Targets

MINER$\nu$A nuclear targets are composed of Fe, C, Pb, water and liquid He (table 3.1) disposed as shown in Figure 3.5. The liquid helium target is placed just downstream of the Veto Wall. The four first modules of the MINER$\nu$A detector are active scintillator modules, making it possible the tracking of particles from events that happened inside the helium volume. The water target is positioned in the nuclear target region and consists of a circular steel frame with a diameter slightly larger than the MINER$\nu$A inner detector size, and Kevlar sheets stretched on the frame [2].

Just upstream of the first 4 scintillator modules the target region consists of five solid nuclear targets, plus the water target. There are four tracking modules between targets, (in a total of 22) which improves the reconstruction of tracks and showers. The nuclear targets are not used for the analysis described in this thesis, which only measures cross sections in the tracker.

---

[2] During the period when the data presented in this Thesis was taken both the liquid helium target and the water target had periods when they were empty or full. This does not influence the signal used for the presented analysis though.
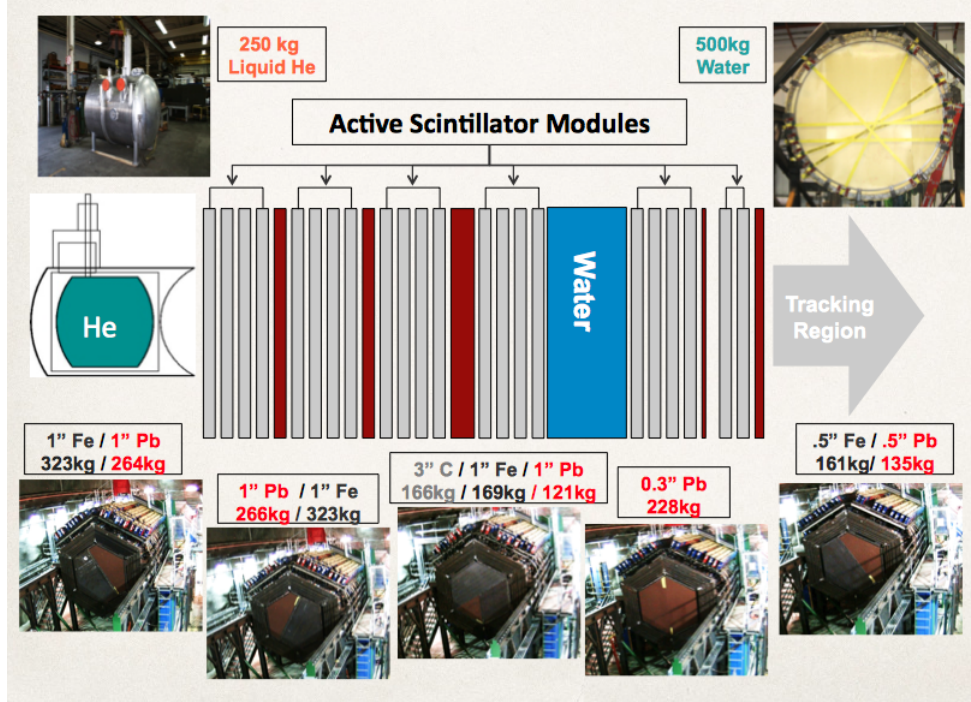
Figure 3.5: MINER$\nu$A Nuclear targets.

| Target material | Mass (ton) |
|:---:|:---:|
| Helium | 0.25 |
| Carbon | 0.12 |
| Iron | 0.99 |
| Lead | 1.02 |
| water | 0.39 |

Table 3.1: Material mass at each nuclear target.

### 3.2.3 The Active Tracker Region

The active target (the core of the detector) consists of strips of solid scintillator and is the primary volume where interactions happen and where all the analysis is centered. The modules in the active tracking region (the region of the detector in which the interactions studied in this analysis take place) are composed entirely of scintillator planes. Planes of the same design are also interspersed with the passive nuclear targets in the upstream region, and with the calorimeter materials in the ECAL and HCAL.

A scintillator plane is made up of 127 strips of doped polystyrene scintillator, with a titanium dioxide coating. The strips have a triangular cross section $17.0 \pm 0.5$ mm and $33.0 \pm 0.5$ mm wide (Figure 3.6) and are arranged in an alternating orientation as shown in Figure 3.7, in order to ensure that any charged particle passing through the plane will produce scintillation

| Material | Percentage (%) |
|----------|----------------|
| Hydrogen | 7.42 |
| Carbon | 86.6 |
| Oxygen | 3.18 |
| Aluminum | 0.26 |
| Silicon | 0.27 |
| Chlorine | 0.55 |
| Titanium | 0.69 |

Table 3.2: Composition by mass of a tracker plane

in at least two strips. The lengths of the individual strips vary from 122 to 245 cm, depending on their positions in the hexagonal plane. The strips are glued together with epoxy, and the planes are then covered in Lexan to prevent light leak between two adjacent planes.
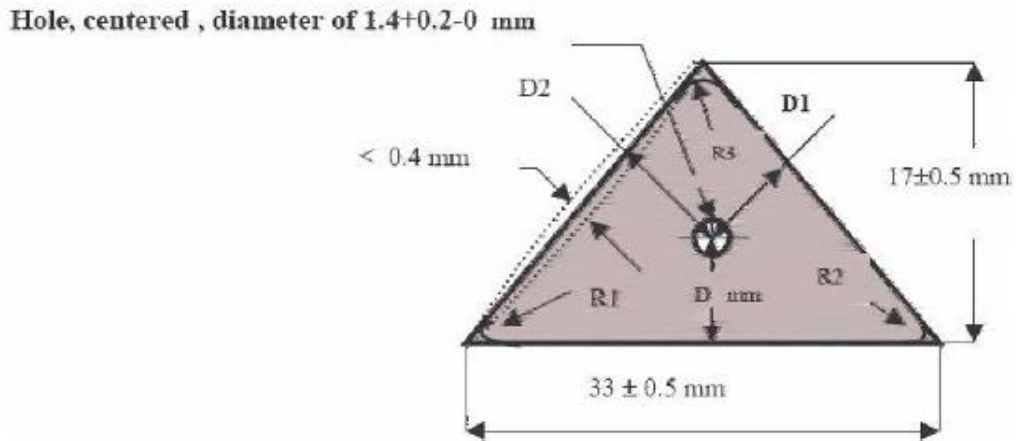


Figure 3.6: Transversal cut of the triangular scintillating prism used in the Inner Detector.[50]

While the polystyrene is a hydrocarbon with a $CH$ structure, the tracker also includes the $TiO_2$ coating, dopant and epoxy, leading to a composition as shown in Table 3.2. A 2.6 $\pm$ 0.2 mm hole drilled down the center of each strip contains a wavelength-shifting fiber, sealed in optical epoxy. The light collection system, including the function of the scintillator and wavelength-shifting fibers, will be explained in section 3.2.7.

Each plane is installed in one of three orientations, X, U or V. In the X orientation, the strips are vertical (parallel to the y axis) meaning that scintillation in a given strip gives information about the x position of a charged particle passing through the plane. Planes with a U or V orientation have the strips oriented at $60^o$ clockwise or counterclockwise, respectively,
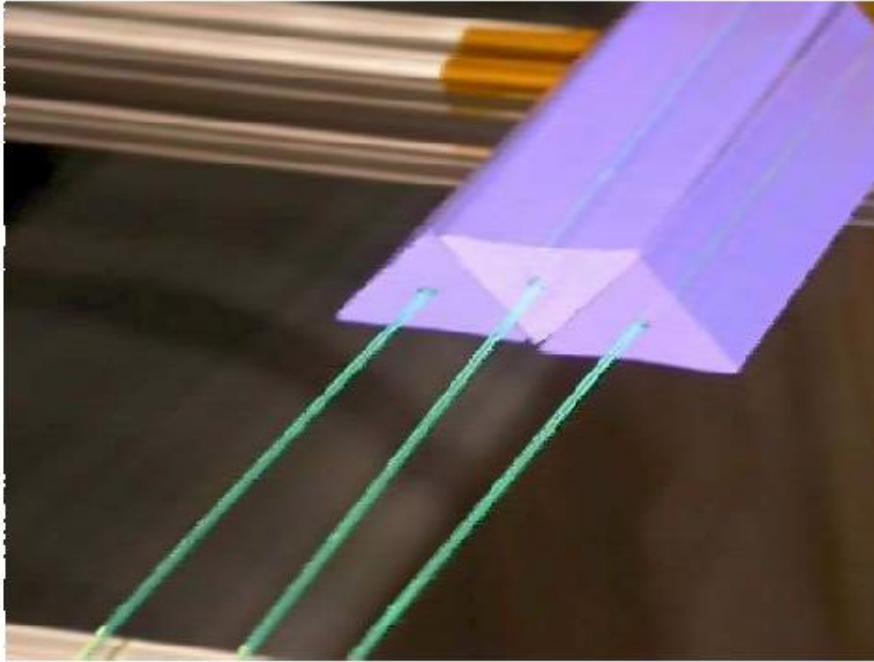
Figure 3.7: Scintillating prisms arranged to form a plane. Each prism holds an optical fiber along its full length.[50]

to the vertical (see Figure 3.8). By including planes with different orientation we are able to reconstruct three-dimensional tracks[3].

Each module in the active tracker region consists of two planes of scintillator strips that alternate between UX and VX configurations, with the X orientation always being downstream of the U or V. The central tracking region, in which this study is based, contains a total of 62 modules. A 2 mm-thick lead collar, colored pink in Figure 3.9, covers the outer 15 cm of each scintillator plane, on the downstream side; this is designed to contain electromagnetic showers in the ID, acting as a side electromagnetic calorimeter.

### 3.2.4 Electromagnetic Calorimeter

The Electromagnetic Calorimeter (ECAL) modules are very similar to the central tracking modules. Although, in order to have a calorimetric usage, it has a 0.2 cm thick sheet of lead covering the entire scintillator plane instead of the 0.2 lead collar present in the scintillator modules, as it can be seen in Figure 3.10. Transition modules are located between the tracking and ECAl regions. This region contains a 0.2 cm thick lead sheet on the downstream end of the

---

[3]Two orientations would actually be sufficient to generate a 3-d track; the third provides a check, especially useful in the case of multiple crossing tracks.
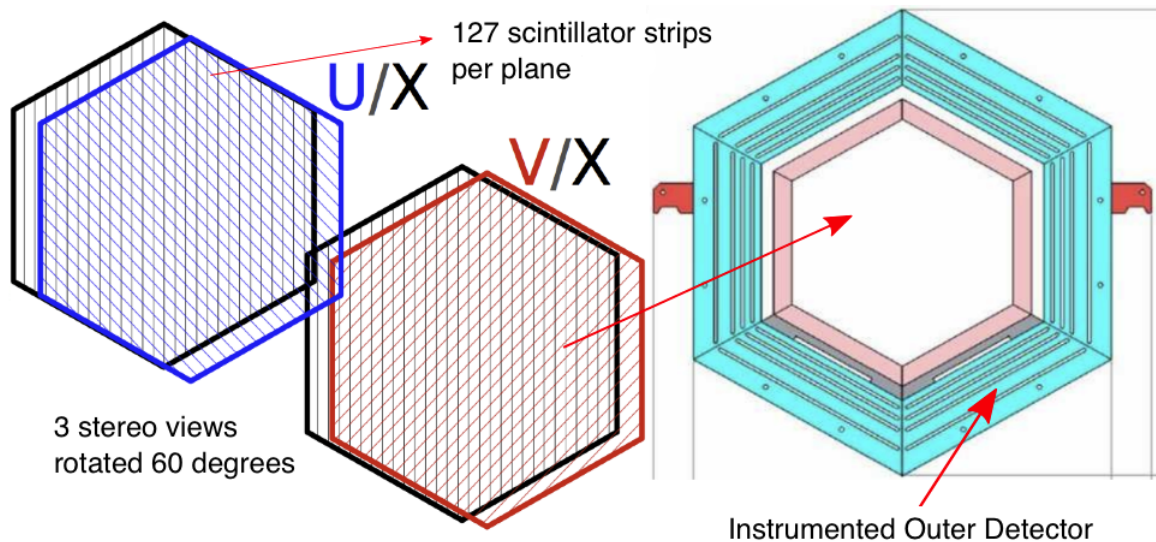
Figure 3.8: Detector active module, X, U and V planes. Note the $\pm\ 60^0$ rotation of the planes U and V relative to the X planes.[50]

module last plane, so that each plane of the ECAL has a lead absorber upstream of it. The fine granularity of the ECAL ensures excellent photon and electron energy resolution and provides directional measurements for these particles. There are 10 modules in the ECAL region of the detector.

### 3.2.5 Hadronic Calorimeter

The Hadronic Calorimeter (HCAL) region consists of 20 modules similar to the tracking region modules, however, instead of two scintillator planes, there is only one partnered with a 2.54 cm thick hexagonal steel plane as shown in Figure 3.11. The resolution of the hadron calorimeter is about $50\%/\sqrt{E}$ for hadron energies above 1 GeV. The resolution can drop to half this value (or less) for low energy particles. The primary reason for the poor resolution is the likely interaction of the particle with a nucleus before stopping, that frequently produces one or more energetic neutrons whose energies are unobserved, making it difficult to get good energy resolution.

### 3.2.6 Outer Detector

The outer detector (OD) is located on the six sides of the hexagonal modules. Its steel frame construction serves as both a supporting structure for the detector modules, and as a hadronic calorimeter. It is also used as a constraint for the plane alignment. Each MINER$\nu$A module consists of an ID and an OD component (the OD is colored blue in Figure 3.8). Plates of iron 55.9 cm thick, with fives slots, each 2.5 cm wide, filled with scintillator. The total iron thickness
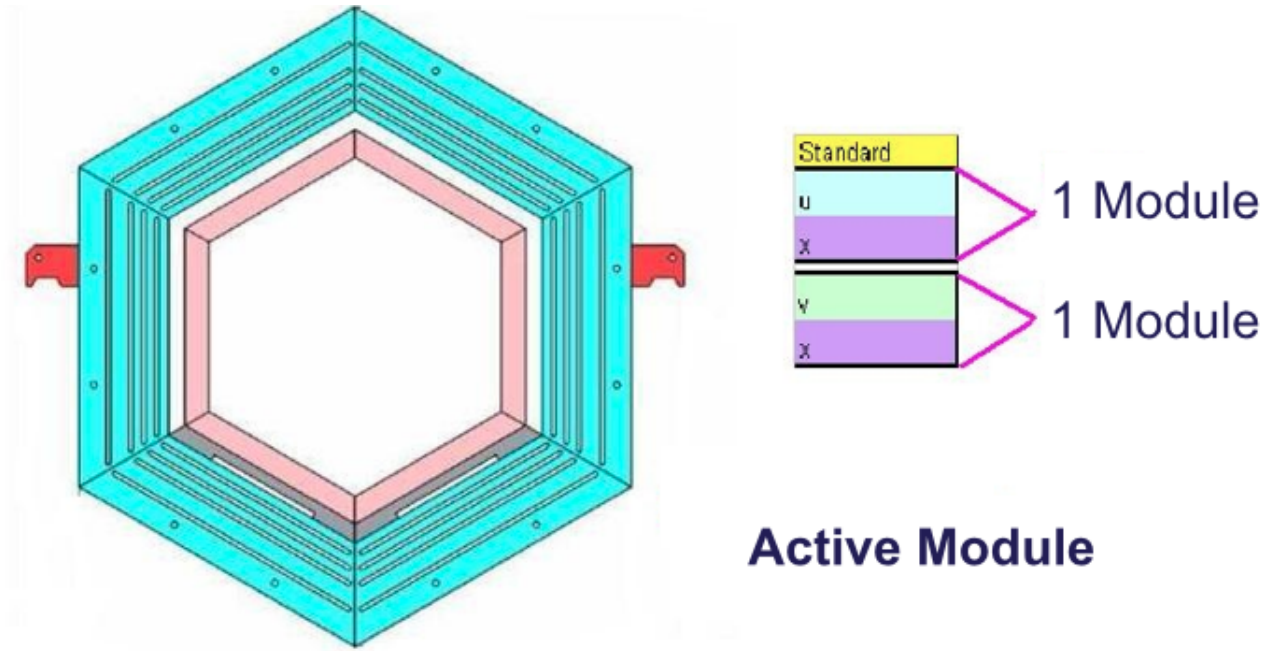
Figure 3.9: Detector active module. Structure of a module is depicted on the right.[50]

is 43.4 cm, or 340 g/cm$^2$, which can stop, from ionization losses alone, nearly all 1 GeV protons entering at an angle of 30$^o$ and all up to 750 MeV protons entering at 90$^o$ with respect to the longitudinal axis. The steel of the outer detector is interleaved with bars of scintillator. The steel enables us to contain hadronic showers generated in the ID; the scintillator enables us to measure the energy produced by these hadrons.

### 3.2.7 Photodevices

The light collected in the scintillators must be converted into electric pulses whose characteristics are related to the deposited energy. The light signal is intense enough to be detected by photodevices with 15% quantum efficiency. MINER$\nu$A uses 507 Hamamatsu Photonics H8804MOD-2 multi-anode PMTs to amplify the scintillation light[4]. Each multi-anode PMT is a collection of 64 individual PMTs distributed in an 8x8 grid measuring 4 $cm^2$. The pixels consist of a bialkali photocathode with a borosilicate glass window and a twelve stage dynode amplification chain. The photocathode quantum efficiency is required to be at least 12 %, at 520 nm and the maximum to minimum pixel gain ratio can be no more than three. The gain of the dynode chain, defined as the number of electrons collected at the anode divided by the number of photoelectrons arriving at the first dynode, is $\sim 5 \times 10^5$. The scintillation light

---

[4]essentially the same PMTs used by MINOS [51] and [52]
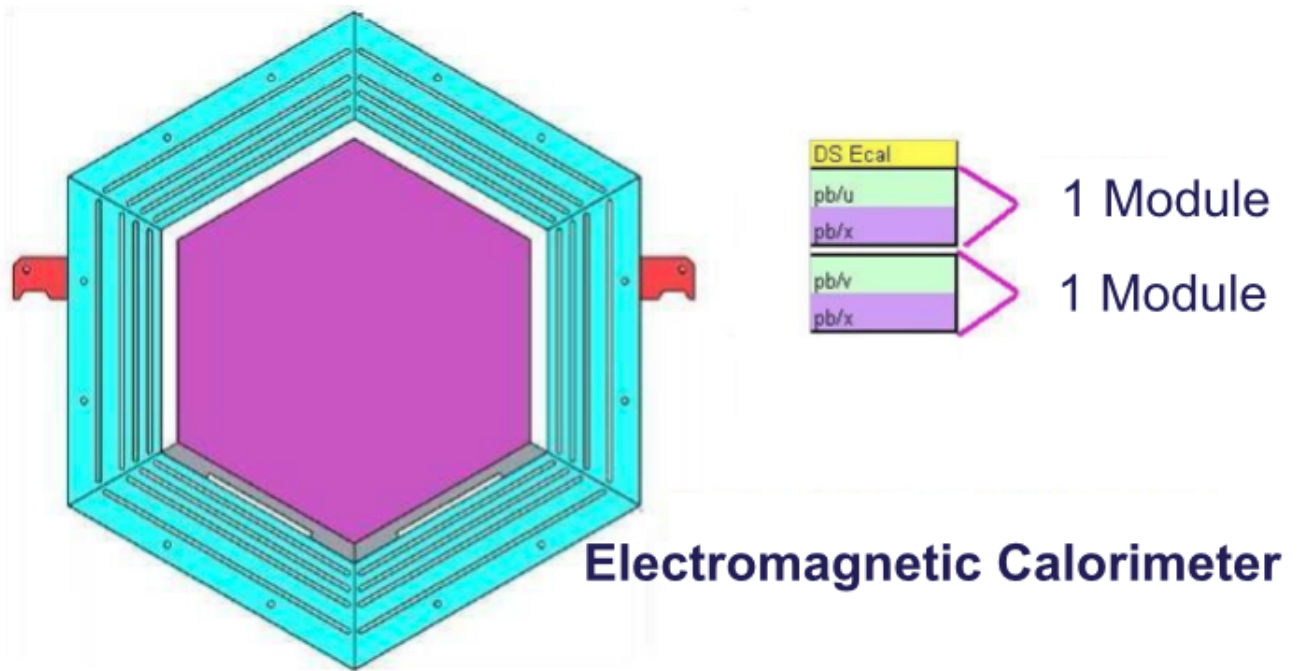
Figure 3.10: Module of the electromagnetic calorimeter. Structure of modules is depicted on the right.[50]

from a minimum ionizing particle typically produces a few photoelectrons at the photocathode resulting in a few-hundred fC electrical signal at the anode.

The PMT and base circuit board are installed inside a 2.36 mm thick steel cylindrical box that provides protection from ambient light, dust, and residual magnetic fields. The PMT boxes are mounted onto racks directly above the detector. A total of 63 clear optical fibers (each one corresponding to a strip in a detector module) are connected to the faceplate of each PMT box. In the interior of the box, light is delivered from the faceplate connector to each pixel by clear optical fibers. An 8x8 cookie, mounted onto the face of the PMT, ensures the alignment of each fiber with its corresponding pixel. The fibers are mapped such that the light from adjacent scintillator strips is not fed to adjacent pixels in the PMT, what minimizes the effect of PMT cross talk, the process by which signal in one pixel can induce a signal in neighboring pixels, on event reconstruction. Figure 3.12 diagrams the fiber mapping.

The MINOS detector magnetic coil creates magnetic fields in the vicinity of MINER$\nu$A that can be around 30 gauss. The performance of the PMTs is adversely affected by magnetic fields higher than 5 gauss, so shielding is necessary. The PMT box itself provides some magnetic shielding. Additionally, the PMTs are oriented perpendicular to the residual field and the 40 PMT boxes closest to the MINOS detector are fitted with a high permeability metal shielding.
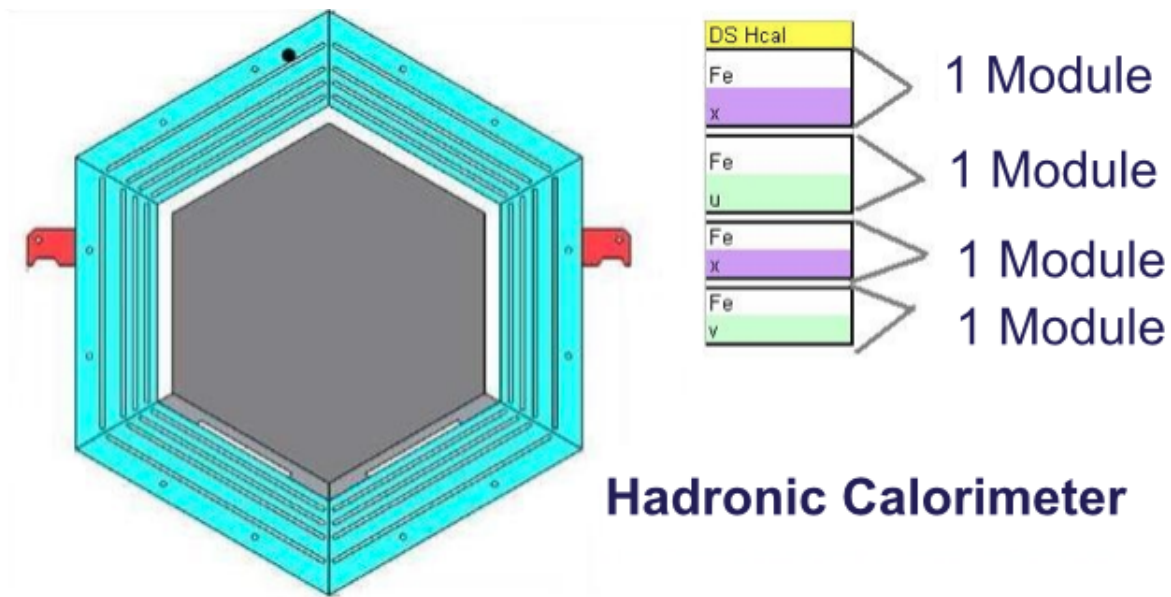
Figure 3.11: Module of the hadronic calorimeter. Structure of the modules with alternating Fe and scintillating planes is depicted on the right.[50]

### 3.2.8 Electronic and data acquisition (DAQ)

The MINERνA data acquisition system is described in detail in [53]. Table 3.3 summarizes the requirements of the electronics of the MINERνA detector that are motivated by the following objectives:

- Fine spacial resolution taking advantage of the light sharing between adjacent scintillating bars;

- $\pi$ and $p$ identification by $dE/dx$;

- Efficient patern recognition using timming to identify the direction of the trajectory and to identify interactions that occur during the same spill;

- Ability to identify strange particles and muon decays through coincidence techniques;

- Neglegible dead time in each spill.

MINERνA DAQ requirements are modest due to the relatively low event rate (about 100 kBytes/s), although the intensity of the beam and number of interactions had a significant raise during the NuMI Beam Medium Energy configuration run.
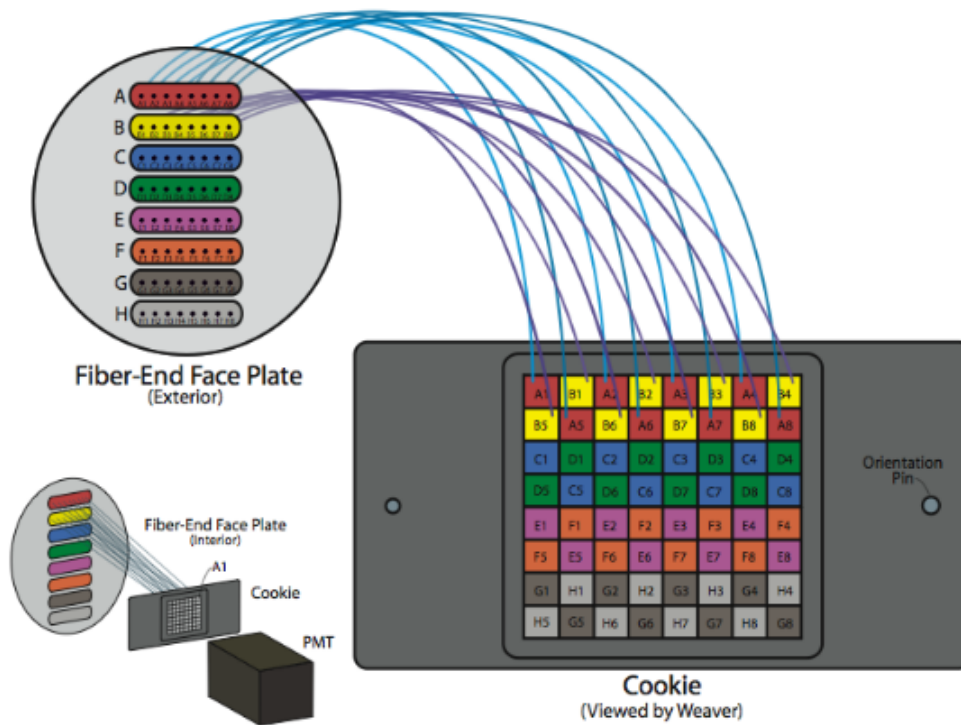
Figure 3.12: Fiber mapping of MINER$\nu$A PMT. [50]

**DAQ hardware**

MINER$\nu$A active elements have their signals sent to multianode photomultipliers (MAPMT). Information about amplitude and time is digitalized by the electronics and stored for readout by the data acquisition system (DAQ). Each readout electronic front-end board (FEB) is connected to one single photomultiplier.

Groups of up to 10 FEB are read and the result sent to a crate read-out controller (CROC) housed in a VME crate. Each CROC can accommodate 4 chains of FEB readout. A total of 12 CROCs is needed for the whole MINER$\nu$A detector. The VME crates also house a CROC

| Parameter | value |
|---|---|
| spill | 12 $\mu$s |
| Repetition time | >1.9 s |
| Number of channels | 30,972 |
| Occupation per spill | 2% |
| gain variation of the photodevice | 4.5 dB |
| Time resolution | 3 ns |

Table 3.3: Some parameters and requirements for the electronics at MINER$\nu$A .

interface module (CRIM), a MINER$\nu$A timing module (MTM) and a 48 V power supply. There are no CPUs in the VME crates. The DAQ works during the whole spill. After a period of 12 $\mu$s the DAQ reads all channels that have a signal above a predefined threshold. Even with a high occupancy rate the total number of bytes that are read in each spill is below 200 kB with zero suppression (1 MB without zero suppression).

The photomultipliers are powered by 48 V power supplies. MINER$\nu$A uses the same hardware for data acquisition and for the detector control system (DCS). A single connection is used for the FEB readout and as communication channel for the control of the detector as, for instance, the control of the MAPMT voltages. The main computers for the DAQ and for the slow control system (the system that controls and monitors the slow varying variables) are close to the VME electronics and are connected to Fermilab network by two high speed TCP/IP lines. A two CPU server controls the whole system: one CPU dedicated to data acquisition and the other dedicated to control and monitoring. All DAQ machines run on Scientific Linux.

**DAQ software**

MINER$\nu$A software runs in the GAUDI [54] framework originally developed for the LHCb collaboration. The expected average of data without data suppression is only 100 kB/s and a two second window is available for each 10 $\mu$ spill. The highly predicable beam time makes a complex trigger system unnecessary and we simply have a gate signal that opens immediately before the arrival of the beam and all charge an time information from the whole detector is registered just after the end of the spill. The slow control system is also simple with each MAPMT having its own local power supply and with the FEB being in charge of reading the high voltages, temperatures and other parameters used for monitoring and control. A schematic diagram of the DAQ is shown in figure 3.13.

## 3.3   The MINOS Near Detector

The Main Injector Neutrino Oscillation Search (MINOS)[22], the original experiment in the NuMI beamline, has been running since 2005. Its extensive program of analysis has included measurements of $\theta_{23}$ [55] through $\nu_\mu$[56] and $\bar{\nu}_\mu$ [57][58] disappearance, and of $\theta_{13}$[59] through $\nu_e$ appearance, as well as searching for sterile neutrinos [60]. The MINOS near detector (henceforth referred to as 'MINOS') is located 2.1 meters downstream of MINER$\nu$A , and is used as a muon spectrometer. MINOS is of key importance to this analysis, as in order to identify antineutrino charged-current events, we require that the muon produced is matched as a $\mu^+$ in MINOS.

The 1kTon MINOS near detector [61], shown schematically in figure 3.14, is composed of 2.54 cm-thick steel planes, interspersed with 1cm-thick layers of scintillator. The scintillator planes
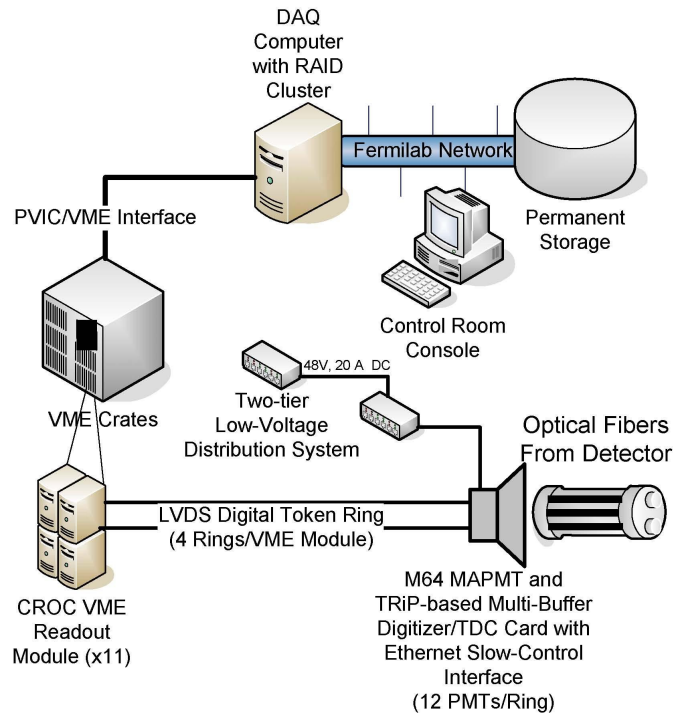
Figure 3.13: Schematic diagram of MINER$\nu$A data acquisition system.

are formed from 4.1 cm-wide parallel strips, with orientation of the strips alternating between $+45°$ and $-45°$ to the vertical in successive planes. The first 120 planes are instrumented for fine sampling; in this region, every fifth steel plane is followed by a fully-instrumented scintillator plane, while all other steel planes are followed by a partially-instrumented scintillator plane. These areas can be seen in Figure3.14. The coarse-sampling region, further downstream, has only the fully-instrumented scintillator every five planes; there are no partial scintillator planes in this region.

The MINOS detector is magnetized by a coil that runs in a loop passing through the detector (see the coil hole in 3.14). This generates a toroidal field with an average strength of 1.3 T. This field causes charged particle tracks to curve; the direction of curvature indicates the particle's charge, while its radius of curvature can be used to estimate the particle's momentum. If a particle ranges out within the calorimeter region, the range of the particle can also give a momentum estimate. Both of these methods are used to obtain the muon momenta used in this analysis; thus uncertainties on the MINOS reconstruction and simulation contribute to our systematic uncertainty on muon energy scale.

The requirement of a muon charge-matched in MINOS significantly aids our purity, by
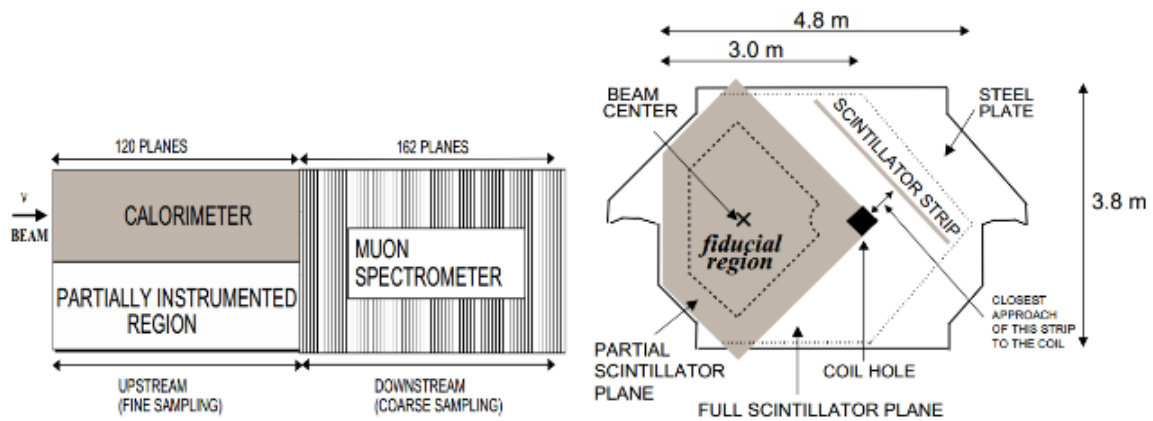
Figure 3.14: Two views of the MINOS near detector: 1. Left from above and 2. Right in the beam direction.[62].

removing almost all wrong-sign neutrino events. The price for this is a limitation on our angular acceptance, as muons must be sufficiently forward-going to intercept the front of the MINOS detector. They must also have sufficient energy to traverse any material between the MINER$\nu$A and MINOS detectors. While this decreased acceptance is also dependent on the position within the MINER$\nu$A detector where an interaction took place (muons produced at the downstream end are more likely to reach MINOS), the approximate result of the MINOS-matching restriction is that we can only reconstruct events with a muon energy above 1.5 GeV and an angle of less than 20° with respect to the beam direction.

In the summer of 2016 the MINOS collaboration ended it's data taking. The Near Detector is still operational under the MINER$\nu$A operations team responsibility.

# Chapter 4

# Simulation

MINER$\nu$A uses several Monte Carlo (MC) packages to model all the steps necessary to simulate the data. The G4numi (Geant4 [63] version 9.2.p03 NuMI) beam Monte Carlo is used to predict the neutrino flux. The flux is then fed to GENIE (Generates Events for Neutrino Interaction Experiments version 2.6.2 [27]) that generates neutrino interactions and transports the recoil hadrons through the nucleus. Geant4 (version 9.2.p03) [63] is used to propagate all particles through the detector[1]. Finally, the particles that exit MINER$\nu$A are propagated to MINOS, where Geant3 version 21.14a is used for the MINOS simulation. This section gives an overview of this simulation chain. Figure 4.1 shows a schematic view of the simulation chain briefly described here.
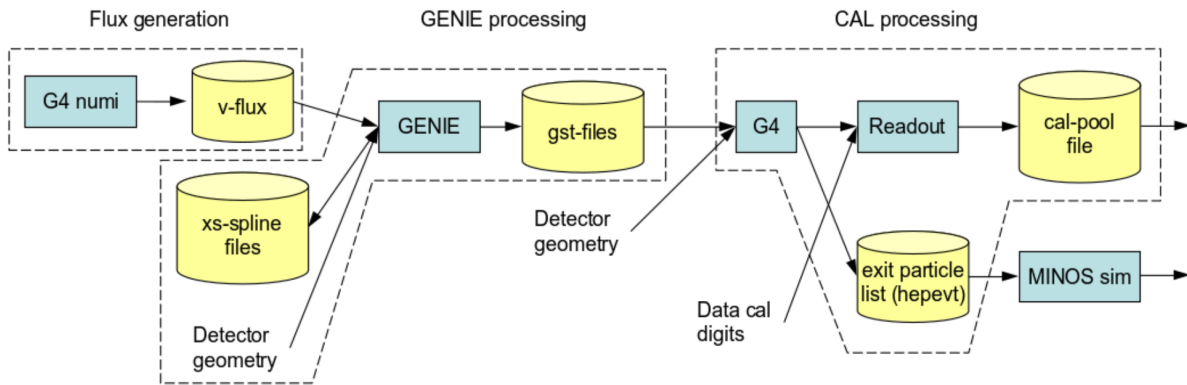


Figure 4.1: Schematic view of the stages necessary to generate MINER$\nu$A MC data.

---

[1]Additional MINER$\nu$A simulation codes that more accurately describe the detector and electronic responses of the particles is also used in this step.

## 4.1  NuMI flux simulation

The NuMI neutrino beamline (section 3.1) has been simulated to provide an estimation of the flux of neutrinos incident upon the MINERνA detector. The components of this simulation are summarized below, and explained in detail in [64]. GEANT4 simulation software is used to simulate the NuMI beamline.

### 4.1.1  Hadron production

Hadron production cross sections for the NuMI proton beam on the graphite target are simulated by the G4numi package, that uses the FTFP_BERT (FRITIOF Precompound - Bertini cascade) inelastic scattering model. This is constrained with proton-carbon scattering data from CERN's NA49 experiment [65] and cross-checked against results from the lower-energy experiment NA61 [66]. NA49 used a 158 GeV proton beam (as opposed to the 120 GeV NuMI beam) incident on a short graphite target (as opposed to NuMI's long rod-shaped target). NA49's data is scaled to NuMI energies using the FLUKA Monte Carlo simulation [67] [68], which assumes Feynman scaling. NA49 data is used when the Feynman scaling variable $x_F < 0.5$, where

$$x_F = \frac{2p_L}{\sqrt{s}} \tag{4.1}$$

and $s$ is the Mandelstam variable corresponding to the squared center of mass energy and $p_L$ is the forward momentum. For $x_F > 0.5$, measurements from the Fermilab Single Arm Spectrometer are used [69]; NA49's measurement takes precedence where data overlaps. It is also used to re-weight kaon production cross sections for $x_F < 0.2$, and nucleon production for $x_F < 0.95$. NA49 cross sections agree with the FTFP simulation to about $\pm 10\%$ for antineutrino production. For $0.2 < x_F < 0.5$, the NA49 pion yields are scaled using the $K/\pi$ ratios measured on a thin carbon target at the MIPP experiment [70].

The PPFX (Package to Predict the FluX) package, released in 2015, is used to implement the reweighting scheme described above. For this analysis, we use PPFX version 1. It includes uncertainties on the hadron production cross sections, as well as on attenuation of the pions, kaons and protons due to re-interaction in the target, or with the materials of the horn and decay pipe (not carbon). Additionally, there is uncertainty due to $K^0$ production and for the estimated contribution of isoscalar conjugate of the $pC \to \pi X$ interaction, $nC \to \pi X$, which has not been directly measured.

PPFX accounts for uncertainty in several components of hadron production, evaluated using the many-universe method, where uncertainties are evaluated by looking at how simulated distributions vary when input parameters are varied within their uncertainties.

### 4.1.2 Beam focusing

Two magnetic horns (described in session 3.1) are used to focus pions and kaons produced in the proton-carbon target interaction. These horns take a maximum current of 200kA, and can be run in a forward or reverse current configuration to favor neutrino or antineutrino production respectively. Whether a given particle is focused sufficiently such that it will produce a neutrino that hits the MINERνA detector depends on its initial momentum and angle, as well as on its charge. The horn system is modeled by GEANT4 [63] using the g4numi package.

Parameters affecting the beam focusing are listed below:

- **Horn transverse offset**: There is a 0.3 mm uncertainty on horn 1 position and 0.5 mm on horn 2.

- **Baffle scraping**: at the tails of the beam transverse position distribution, the beam may hit ('scrape') the walls of the baffle. There is a 0.25% uncertainty [71] on how much of the beam scrapes the baffle.

- **POT counting**: number of protons on target delivered by the NuMI beam is known to 2% [71].

- **Horn current uncertainty**: uncertainty on the current delivered to the horns (nominally -185 kA for this analysis) has 1% uncertainty [71].

- **Horn inner conductor shape**: two different implemetations of the inner conductor shape model change give flux differences similar to changing the horn current by 0.8%. We use 100% of this as an uncertainty on the inner conductor shape.

- **Target longitudinal offset**: Target position changed at different times during the low-energy run, affecting the falling edge of the focusing peak. This accounts for residual uncertainty on the offset.

- **Water layer uncertainty**: A $1.0 \pm 0.5$ mm layer of water on the inside surface of the inner conductor cools the horns. We simulate a 1 mm layer and use the difference between that and 0.5 mm as an uncertainty.

## 4.2 GENIE MC Neutrino Event Generator

After the simulation of the NuMI beamline flux the next step is to simulate the neutrino interactions. MINERνA uses GENIE (Generates Events for Neutrino Interaction Experiments) [27] version 2.8.4 to model the physics process within the detector. The GENIE flux driver uses

a spatial window to predict neutrino flux at a specific location. The flux window is located upstream of the MINERνA Detector, and its position is given in terms of beamline coordinates [72]. The window size is optimized to prevent unnecessary inefficient generation.

A cross section spline file is used for efficient generation. The cross section spline file is pre-generated for each interaction type, each neutrino flavor and each different material in the target. A geometry analyser calculates path lengths through volumes for each material [72]. The neutrino interaction is predicted using density and cross section probability. Once the interaction is determined, GENIE selects the interaction process considering relative likelihood for each process $P_p(E_\nu) = \sigma p(E_\nu)$. Finally event kinematics are determined according to the corresponding physical model.

### 4.2.1  Quasi-Elastic Scattering

The quasi-elastic scattering is modeled according to the Llewellyn-Smith formalism. The electromagnetic form factors are parametrized using the BBBA2005 model [73]. The pseudo-scalar form factor is assumed to have the form suggested by the partially conserved axial current (PCAC) hypothesis, leaving the axial form factor as the only remaining unknown factor. GENIE assumes a dipole form with the axial vector mass MA remaining as the sole free parameter with a default value of 0.99 GeV/c$^2$.

### 4.2.2  Resonance Scattering

The Rein-Sehgal Model is used to simulate this kind of interaction process. The double differential cross section for single meson production in this model is given by [43]:

$$\frac{d^2\sigma}{dQ^2 d\nu} = \frac{1}{32\pi m_N E_\nu^2} \frac{1}{2} \sum_{spins} |T(\nu N \to l N^*)|^2 \delta(W^2 - M^2) \tag{4.2}$$

where $|T(\nu N \to l N^*)|^2$ is the amplitude of a given resonance production, which is calculated via the Feynman-Kislinger-Ravndal model [74] and $W$ is the hadronic invariant mass.

From the 18 resonances of the Rein-Sehgal model original paper [43], GENIE includes the 16 that are listed as unambiguous at the latest PDG baryon tables and all resonance parameters have been updated. Interference between neighboring resonances has been ignored in this implementation of the Rein-Sehgal model. The default value for the resonance axial vector mass $M_A$ is 1.12 GeV/c$^2$ as determined in the global fits carried out in [75].

### 4.2.3  Coherent Pion Production

The coherent neutrino-nucleus interactions are also modeled according to the Rein-Sehgal model [43].

Since the coherence condition requires a small momentum transfer to the target nucleus, it is a low-$Q^2$ process which is related via PCAC to the pion field. The Rein-Sehgal model begins from the PCAC form at $Q^2 = 0$. Based on the PCAC formalism, the differential cross section for $Q^2 = 0$ is given by:

$$\frac{d^3\sigma(\nu A \to lA\pi)}{dxdydt}\Big|_{Q^2=0} = \frac{G_F^2}{\pi^2}f_\pi^2 m_N E_\nu(1-y)\frac{\sigma(\pi A \to \pi A)}{dt}\Big|_{E_\nu y = E_\pi} \tag{4.3}$$

where $G_F$ is the weak coupling constant, $f_\pi$ the pion decay constant, $m_N$ is the nucleon mass, $\nu$ is the energy transfer, $t$ the square of the four-momentum transferred to the nucleus and the bjorken kinematic variables $x$, $y$ are expressed as:

$$x = \frac{Q^2}{2m_N\nu} \quad y = \frac{\nu}{E_\nu} \tag{4.4}$$

For values of $Q^2 \neq 0$ the model assumes a dipole dependence with $M_A = 1.00 \text{GeV/c}^2$ and calculates the relevant pion-nucleus cross section from measured data on total and inelastic pion scattering from protons and deuterium. The GENIE implementation uses the modified PCAC formula described in a recent revision of the Rein-Sehgal model that includes lepton mass terms [27].

### 4.2.4 Deep Inelastic Scattering

The deep inelastic scattering (DIS) process is calculated in an effective leading order model using the modifications suggested by Bodek and Yang at low $Q^2$ [76]. The double differential cross section for this process is calculated as:

$$\frac{d\sigma^2}{dxdy} = \frac{G_F^2 m_N E_\nu}{\pi}[(1 - y + \frac{1}{2}y^2 + C_1)F_2(x) \mp y(1 - \frac{1}{2}y + C_2)xF_3(x)] \tag{4.5}$$

where:

$$C_1 = \frac{m_l^2(y-2)}{4m_N E_\nu x} - \frac{m_N xy}{2E_\nu} - \frac{m_l^2}{4E_\nu^2} \quad C_2 = -\frac{m_l^2}{4m_N E_\nu x} \tag{4.6}$$

$x, y$ are the bjorken scaling variables defined in a DIS process as:

$$x = \frac{Q^2}{2m_N(E_\nu - E_t) + m_N^2} \quad y = \frac{E_\nu - E_t}{E_\nu} \tag{4.7}$$

$E_\nu$ is the energy of the final state lepton, and $F_2(x)$, $xF_3(x)$ the nucleon structure functions calculated with the GRV98 parton distribution functions [77].

**Transition region to DIS**

GENIE restricts the resonance production using a hadronic invariant mass cut of $W > 1.7$ GeV and restricts the DIS production using a hadronic invariant mass cut of $W > m_{\Delta^{++}}$ where

$m_{\Delta^{++}} = 1.232$ GeV [78] so that the RES/DIS mixture in this region agrees with the inclusive cross section data. GENIE also follows NEUGEN procedure [79] for supressing DIS interactions with resonance-like final states $(1\pi, 2\pi)$ in order to avoid double counting.

### 4.2.5 Hadron Production

The hadronization model determines the final state particles and 4-momenta given the nature of a neutrino-nucleon interaction (CC/NC, $\nu$, $\bar{\nu}$, target neutron/proton) and the event kinematics $(Q^2, W, x, y)$. GENIE uses the AGKY model [80]. This model is now the default hadronization model in neutrino Monte Carlo generators. GENIE includes a phenomenological description of the low invariant mass region based on the Koba-Nielsen-Olesen (KNO) scaling [79] and the PYTHIA/JETSET model for higher masses. The transition from the KNO-based model to the PYTHIA/JETSET model takes place gradually, at an intermediate invariant mass region, ensuring the continuity of all simulated observables as a function of the invariant mass. The reference [27] gives a detailed description of these models

## 4.3 Nuclear Effects

As discussed in Section 2.2.4 the Monte Carlo generator need to use models to simulated the nucleus enviroment where the neutrino scatters. GENIE describes the Neutrino-nucleon scattering processes considering the relativistic Fermi Gas Model to account for the corresponding nuclear effects and Intranuke to take FSI into account.

### 4.3.1 Relativistic Fermi Gas Model

In this model, protons and neutrons are considered as moving freely within the nuclear volume. The system obeys the Fermi-Dirac statistics leading to the Pauli exclusion principle. Neutrons and protons are distinguishable fermions and are therefore situated in two separate potential wells (see Figure 4.2).

The number of states that nucleons in a volume $V$ and momentum interval $dp$ can have is given by:

$$dn = \frac{4\pi p^2 V}{(2\pi h/2\pi)^3} dp \tag{4.8}$$

For the nucleus in its ground state, all states from the minimum momentum up to the maximum momentum will be filled. The maximum level is called the Fermi momentum $(p_F)$. The total number of states is obtained integrating from 0 to $p_F$:

$$n = \frac{V p_F^3}{6\pi^2 (h/2\pi)^3} \tag{4.9}$$
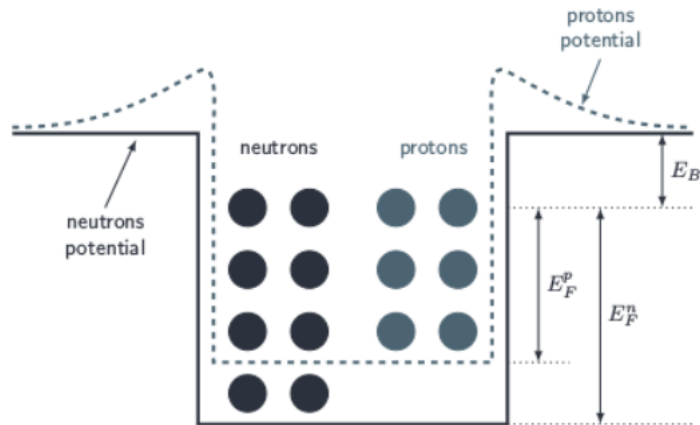
Figure 4.2: Proton and neutron potential wells and states in the Fermi gas model. $E_F^p$, $E_F^n$ are the Fermi energy of the proton and neutron respectively.

As the nucleons have spin-1/2, there are two nucleons for each energy level and hence for each of the nucleon types

$$N = \frac{V(P_F^n)^3}{3\pi^2(h/2\pi)^3} \; , \; Z = \frac{V(P_F^p)^3}{3\pi^2(h/2\pi)^3} \tag{4.10}$$

where $P_F^n$, $P_F^p$ are the fermi momentum for neutrons and protons respectively. If we consider a spherical volume of radius $R = 1.21$ fm in the last presented equation, as well as $Z = N = A/2$ and consider that the potential wells for protons and neutrons have the same radius, we get:

$$V = \frac{4}{3}\pi R^3|_{R=1.21fm} \rightarrow P_F = P_F^n = P_F^p = \frac{h}{2\pi}\frac{1}{R}(\frac{9\pi}{8})^{1/3}|_{R=1.21fm} \approx 250 MeV/c \tag{4.11}$$

and the Fermi energy $E_F = \frac{P_F^2}{2m_N} \approx 33$ MeV. The difference between the edge of the potential and the fermi energy is called binding energy and is constant for most nuclei and equal to the average binding energy per nucleon (see Figure 4.2).In the Fermi gas model a neutrino-nucleon interaction occurs only when the nucleon receives a momentum above the Fermi momentum (because all the states are already occupied). This suppression is called Pauli blocking.

Although this model provides a good description of the nuclear response it does not account for the effects of dynamical nucleon-nucleon correlations in the initial and final states, which play an important role in specific kinematical regions.

### 4.3.2 Final State Interactions

GENIE uses Intranuke to simulate final states interactions. When the neutrino interacts with a bound nucleon, the product of these interactions can also interact intra-nuclearly with other

nucleons. This is called FSI (final state interactions). The intra-nuclear interactions of nucleons and mesons produced in neutrino interactions are important nuclear effects to take into account. In particular, pion absorption interactions are events in which pion is not observed in the final states. A rescattering of protons can also modify the momentum of the particle.

Since all this happens inside the nucleus, it cannot be seen by the detector and it can potentially affect the classification of the event type in the analysis (pions absorbed, for example, are an irreducible background in quasi-elastic scattering). For this reason this analysis focuses on a "QE-like" definition, that considers any number of nucleons in the final state but no pions.

## 4.4   Detector Simulation

The analysis and simulation for MINER$\nu$A are implemented in the GAUDI Framework [54] where GEANT4 is used to simulate the detector. Each event generated by GENIE has no time stamp and is distributed randomly according to the NuMI Beamline time structure and later handed by GEANT4. The default GEANT model is used for electromagnetic interactions and the QGSP BERT model is used for hadronic interactions.

A proper detector simulation requires a geometry definition. This consists of the definition of shapes and materials as well as the structural placements of all the parts that compose the MINER$\nu$A detector. The framework permits the unlimited use of the same shapes, what is very useful since MINER$\nu$A is composed by several mostly equal modules. All the important aspects related to the real detector have been included in the geometry simulation, from the scintillator strips definition (including accurate shape, coating and glue) to the massive Outer Detector towers.

The geometry used by the MC codes is based on XML. Due to the flexibility of the XML structure, different detectors configurations can be easily used by the simulation framework. This feature is very important since the detector had several different configurations during it's first set of runs and the liquid targets are in constant maintenance.

## 4.5   Data Overlay

Many aspects of the real detector are not simulated by the steps mentioned in the previous sessions. Some of them are: the event overlap in the detector, events in the side calorimeters, rock muons, dead time and miscalibrations. Instead of developing complex and extensive addendum to the simulation these effects are directly imported from the real data. The overlay of MC with Data includes all non-simulated effects in a reliable way.

MC data samples are generated for specific run periods and the data used for the overlay

is randomly selected from the data taken in the same specific period. The idea is to take into account time variation and hardware updates for the corresponding running conditions.

## 4.6   MINOS Simulation

The positions and momenta of simulated particles that exit MINERvA from the back are fed into a MINOS -owned GEANT3 simulation of the MINOS near detector [81]. The simulation includes the passage of charged particles through the magnetic field and the readout of energy deposited in active elements. Reconstruction is then performed using the hits generated by these simulated particles. Hit and track information is retained from the MINOS gate (called a snarl) that corresponds to the MINERvA gate used in the data overlay procedure. In doing so, the confusion during the process of matching a reconstructed track from MINERvA into MINOS that occurs due to event overlap is simulated. Overlap during track finding in MINOS is not simulated, because the reconstruction only considers the hits on generated particles.

# Chapter 5

# Reconstruction

We apply reconstruction algorithms to both the callibrated data and Monte Carlo simulation in order to analyze the patterns of the energy deposits and to identify particle tracks. This procedure identifies tracks and distinct groups of energy deposit in the MINER$\nu$A detector as well as accounts for the dispersed energy. This reconstructed data is saved in the form of ROOT ntuple files, which are then made available for further analysis-specific processing.

The analysis presented in this thesis is dependent on the correct reconstruction of the kinematics of the muons created in the MINER$\nu$A detector and matched to muons in the MINOS detector. In order to reconstruct a muon, we must:

- Divide a gate's data into *time slices* corresponding to individual interactions or events

- Identify energy *clusters* within a time slice

- Group clusters to generate *track* candidates

- Identify which track represents the muon, and identify the *interaction vertex*

- Identify muon tracks in MINOS

- Match the MINER$\nu$A track to a MINOS track to reconstruct its charge and energy

In the following sections we explain the reconstruction of proton tracks and Michel electrons, another significant point in this analysis. A more detailed description can be found in [49].

## 5.1 Time Slicing

Neutrinos have a very small cross section but the NuMI beam is the most intense neutrino beam active in the world. A single NuMI beam spill can produce multiple event interactions in the detector. It is then important to break the time spill into several slices. In order to do this,

a time window of 30 ns is initially taken. If the integrated number of photoelectrons in that window is greater than 10 a candidate time slice is created. The subsequent hits continue to be added to the time slice until the total integrated number of photoelectrons is less than 10. Figure 5.1 shows the time distribution of the hits within a single NuMI beam spill. Different colored peaks identify different time slices.
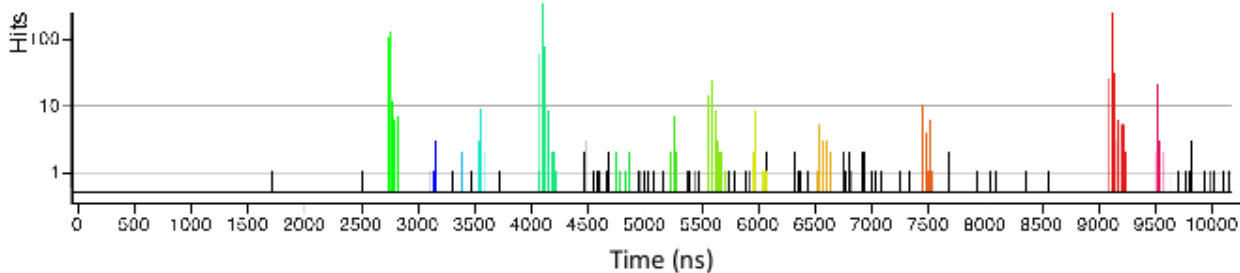


Figure 5.1: Time distribution of hits in a NuMI beam spill. Colored peaks represent the time slices created.[82]

## 5.2 Clustering

Hits are spatially classified by first grouping all contiguous ones in position within a plane. Isolated hits compose its own cluster. The time and energy of a cluster are defined as follows:

- **Time:** the cluster time is equal to the most energetic hit time in that cluster.

- **Energy:** the energy of the cluster is calculated as the total sum of all energy hits in that cluster.

Additionally, it is known that the topology of each cluster will be different depending on the particles that compose the cluster. These topologies are classified in the following way:

- **Low Activity:** any cluster with an energy less than 1 MeV.

- **Cross Talk:** each hit in the detector is registered by a specific pixel on one of the PMTs. There's always the possibility of optical cross talk given the proximity of the pixels in the PMT. Each hit is mapped to its corresponding PMT pixel and then compared to the neighbor pixels in that PMT. If the photoelectrons measured are consistent with cross talk, the cluster is tagged as such.

- **Heavy Ionizing:** clusters with an energy greater than 12 MeV and less than 5 hits. Additionally, at least one hit (but less than four) energy needs to be greater than 0.5 MeV and they all have to be contiguous.

- **Trackable:** clusters whose energy is between 1 and 12 MeV and have less than 5 hits. In addition, at least one hit (but less than three) must have energy between 0.5 MeV and 12 MeV and hits have to be contiguous in space

- **Superclusters:** clusters that do not pass the previous categories criteria. These clusters are consistent with electromagnetic or hadronic showers

## 5.3 Tracking

Clusters that fall into the trackable and heavy ionizing category, go through a series of algorithms in order to have a track reconstructed. In this analysis we aim at the reconstruction of muons and hadrons trajectories. Muons are minimum ionizing particles that travel through the detector without having their trajectories changed by interactions with the detector. Hence, a single track is enough for reconstruction. Hadrons, on the other hand, tend to interact more and we must be able to reconstruct multiple tracks.

The MINER$\nu$A framework, designed to reconstruct these trajectories, is composed of the LongTracker and two ShortTrackers algorithms. The first is used to reconstruct the muon and a combination of the three (LongTracker+ShortTrackers) is used to reconstruct hadron trajectories. The sequence in the reconstruction code is the following:

- The Anchor Track: the LongTracker algorithm is used to select the longest track (that, most of the time, is the muon) as the anchored track. This track must have traveled at least 25 planes through the detector or else the event is discarded. The event vertex is defined as the origin of the selected anchored track. The clusters not related to this track are then freed to be used by any algorithm.

- The Anchored Tracks: after the anchor track is created, the LongTracker and Short-Tracker algorithms are run on the clusters that were freed and are kept if they are compatible with the event vertex. Compatible here means that: (a) the anchored track projection has to be no more than 100 mm away from the event vertex and (b) its origin has to be less than 250 mm away from the event vertex. This is repeated multiple times until there are no more free clusters meeting these requirements.

- The Secondary Tracks: after the anchor track and all the anchored tracks are created, the search of tracks continue by looking at the end position of the anchored tracks. The procedure is similar to the anchored tracks with the difference that the anchor point is the end of a track instead of the event vertex. This sequence continues in a loop until no more secondary tracks can be found.

### 5.3.1 The LongTracker

This algorithm looks for tracks in all seeds within a single time slice. A seed is a group of 3 trackable or heavy ionizing clusters that meet the following criteria: two clusters in the same plane are not allowed; each cluster plane has to be in the same orientation (X, U or V); clusters must be in consecutive planes; cluster need to be fitted in a two-dimensional line. Additionally, only a single cluster is allowed to belong to multiple seeds.

These requirements limit seeds to reconstruct tracks within 70 degrees from the longitudinal axis. The seeds with the same plane orientation are then merged to form track candidates if they meet the following criteria: the slope of the seeds linear fits are consistent; the seeds share at least one cluster; the seeds do not contain different clusters in the same scintillator plane. Each seed can only be used by a single track candidate. After all track candidates are formed they can also be merged[1]. The existence of gaps allows the track candidates to accurately follow particle trajectories that intersect dead regions in the detector.

Two routines are used in the attempt to form three-dimensional track objects from the track candidates [49]:

- The first routine looks for all possible combinations of three candidates in which no two candidates share the same plane orientation. These combinations form a 3D-track if they overlap longitudinally and are mutually consistent with the same three-dimensional line. This routine also searches for particular topologies in which a particle trajectory bends in only two views. In that case, the longer candidate is broken into two shorter candidates and kinked tracks are found.

- The second routine examines all remaining candidates to form all possible combinations of two candidates which do not share the same plane orientation. These are then used to construct a three-dimensional line if they have a similar longitudinal overlap. After this, a search for unused clusters with a position consistent with the candidate pair is performed in the remaining view in order to form a three-dimensional track. This technique is specially powerful for tracking particle trajectories that are obscured by detector activity in one of the three orientations

The three-dimensional tracks are then fit by a Kalman filter. Figure 5.2 shows the tracking position resolution after the Kalman filter fit. The track found is then submitted to a procedure called track cleaning that removes the energy that is likely to be unrelated to the track, and improves the vertex energy measurement.

---

[1]Track candidates are not required to share clusters.
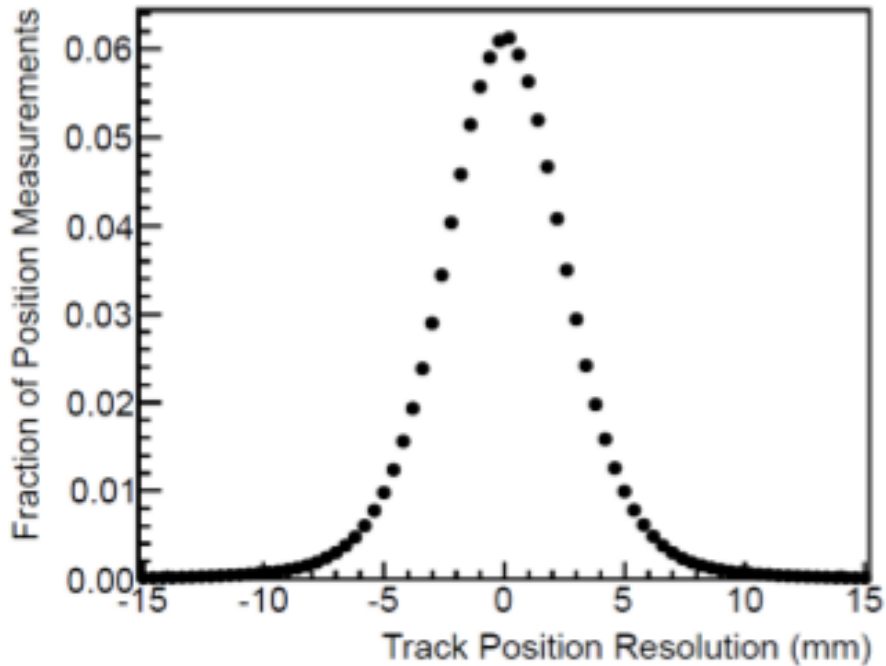
Figure 5.2: Resolution of the fitted positions along a track relative to the measured cluster positions for a sample of data rock muons

## 5.3.2 The ShortTracker

The short tracker algorithms are effective especially in hadron-like track particles because the energy deposition is greater than the muon and they tend to interact more with the detector and, consequently, are more likely to travel shorter distances. This analysis uses two short tracker algorithms that can reconstruct short trajectories starting with 5 planes or more: the *Vertex Anchored Short Tracker* and the *Vertex Energy Study Tool*.

**Vertex Anchored Short Tracker**

MINER$\nu$A needs at least four clusters to form a three-dimensional track. This algorithm uses three-dimensional seeds constructed from four clusters in consecutive planes as long as they follow one of the following patterns: XUXV, XVXU, UXVX, VXUX. Once the seeds are constructed, the short tracker tries to merge the seeds into longer tracks.

The following conditions are necessary:

- Seeds need to share one or more clusters

- Polar angles have to be of similar order

- Resemble a straight line

- Pass a Kalman filter fit with a $\chi^2 < 10$

The proccess is repeated until no more seeds can be merged.

**The Vertex Energy Study Tool**

This short tracker uses a Hough transform to reconstruct three-dimensional tracks. It works as an angle scanner between the anchor track and the ID Clusters. This algorithm increases the reconstruction efficiency especially near the vertex, since the track needs to pass through the anchor vertex and have a cluster near the reconstructed vertex.

## 5.4   Muon Reconstruction

Since MINER$\nu$A is not magnetized we must rely on the MINOS near detector to determine the charge and momentum of muons exiting the MINER$\nu$A detector and entering MINOS. In order for tracks in MINER$\nu$A and MINOS to be matched and merged into a muon candidate, the following conditions are required: the difference in time between both tracks has to be less than 200 ns, the MINER$\nu$A track must have activity in at least one of the five last modules of the detector, the MINOS track must start within one of the four first planes of MINOS.

Due to these requirements this technique accepts muons within 20 degrees scattering angle with respect to the longitudinal axis. There are two methods used to match tracks [49]:

- **Track projection method:** the MINOS track is extrapolated to the plane that contains the last activity on a MINER$\nu$A track and the MINERA track is extrapolated to the plane that contains the start of the MINOS track. The distance between the most downstream activity from the MINER$\nu$A track and the start of the MINOS track must be smaller than 40 cm to be considered as a matched

- **Closest Approach method:** if the previous method does not find matched tracks, the MINOS track is projected towards MINER$\nu$A and the MINER$\nu$A track towards MINOS and the point of the closest approach of the two tracks is found. This is especially useful if the muon undergoes a hard scatter in the passive material between the two detectors.

The charge is inferred by the deflection of the muon due to the MINOS magnetic field. The momentum in MINOS is determined by two different methods:

- **The Range method** this is based on the total energy loss through interactions in the MINOS detector and is applied to muons contained inside the calorimeter region. The momentum is calculated by integration of this energy loss.

- **The Curvature method:** this methods reconstructs the momentum by relating the curvature of the track ($K$), the magnetic field ($B$) and the momentum component perpendicular to the field ($P$) as $K = 0.3B/P_\mu$

## 5.5  Proton Reconstruction

The fine granularity and light yield of the MINER$\nu$A detector makes it possible to use $dE/dX$ profiles near the ends of the reconstructed tracks to identify particles that stop in the detector [49]. In cases where the hadron loses energy via electromagnetic processes, decays in flight, elastic scattering or minimum inelastic hadron scattering, the $dE/dX$ can differentiate between minimum and heavily ionizing particles. However, hadrons can interact or be absorbed in the detector too, which affects the performance of this technique for such cases. For each track found using the algorithms described in the previous sessions, a $\chi^2$ is determined by comparing the energy deposited per scintillator plane to templates derived from the $dE/dX$ profile expected in the detector for different momenta and for two different types: protons and pions. Figure 5.3 shows the $dE/dx$ profile for a proton compared to the pion and proton templates. The profile is gotten from a reconstructed track in data, where the measured proton momentum is 1 GeV/c and the $\chi^2/ndf = 29/33$.

A particle score is computed as:

$$\text{particle score}_{p(\pi)} = \frac{(\chi^2/ndf)^2_{p(\pi)}}{\sqrt{(\chi^2/ndf)^2_p + (\chi^2/ndf)^2_\pi}} \tag{5.1}$$

and it's used later for signal selection.

## 5.6  Michel Electrons Reconstruction

A Michel electron is an electron produced by the decay of a muon. The dominant muon decay is also known as the "Michel decay", named after Louis Michel (See reference [83]), and it happens as:

$$\mu^+ \rightarrow e^+ + \nu_e + \overline{\nu}_\mu \ , \ \mu^- \rightarrow e^- + \overline{\nu}_e + \nu_\mu \tag{5.2}$$

In this analysis, Michel electrons are reconstructed in order to veto events with soft pions in the final state that decay into Michel electrons

A Michel electron is identified by searching for a delayed signal near the endpoint of a stopped muon track. However, isolated energy depositions in time slices with no other detector activity are found predominantly due to delayed Michel electrons. Because of this, the full sample of such energy depositions can be used without requiring a precursor muon.
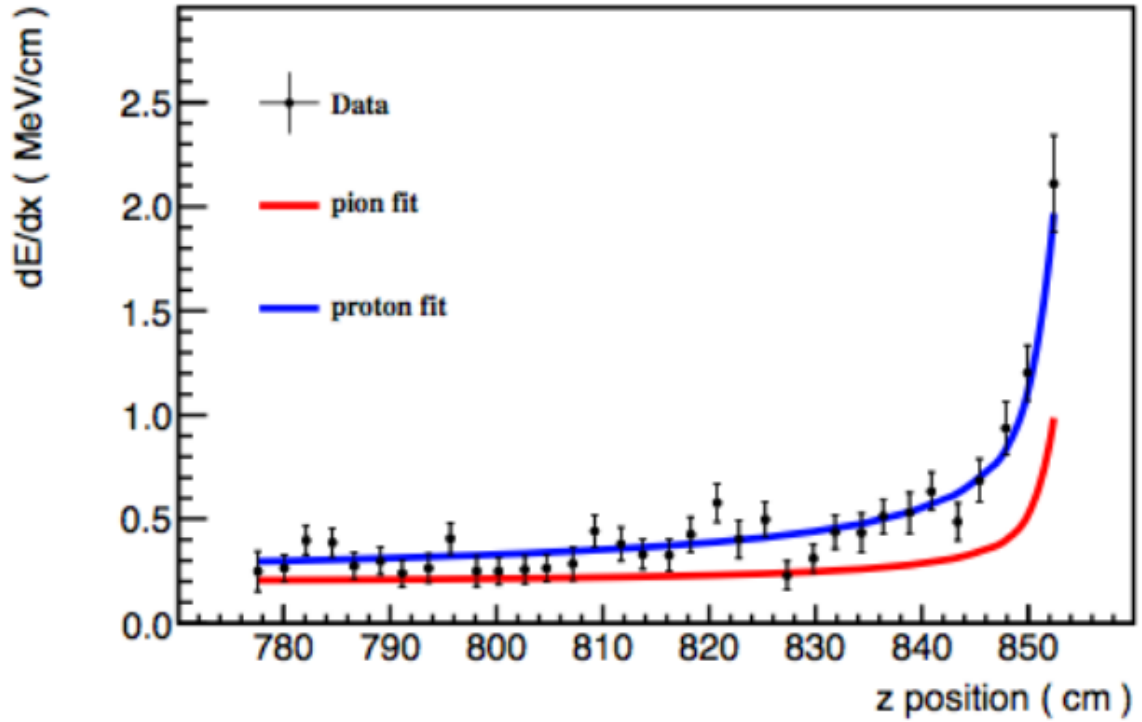
Figure 5.3: $dE/dx$ profiles for an identified proton in data

## 5.7 Recoil Energy Reconstruction

The recoil energy is calculated using a simple calorimetric sum of the clusters not associated with the muon. In this analysis, the selected clusters are outside a region near the vertex because the MonteCarlo does not fully simulate some of the potential hadronic final states in the event. By isolating this region the analysis remains insensitive to those effects. For a more detailed definition of the constants see reference [49]

# Chapter 6

# Event Sample Selection

Once simulation and reconstruction are done we must go to the proccess of selecting the events that are relevant for the physics analysis. We apply different cuts and vetos based on topological, physical or experimental arguments. These selection cuts are applied to both Monte Carlo and data.

## 6.1   Event Sample

The simulated event sample used in this analysis corresponds to $1.17 \times 10^{21}$ protons on target (POT), which is equivalent to about 4.15 times the data amount. Chapter 4 presents details of the Monte Carlo used for this analysis. When Monte Carlo and data are presented together, Monte Carlo is POT normalized with a scale defined as:

$$MC_{scale}^{POT} = \frac{POT_{data}}{POT_{MC}} \tag{6.1}$$

Data used in this analysis represents the first set of data taken in the Medium Energy (ME) run as shown out in Figure 6.1. This data was taken from September of 2013 to September of 2014, which corresponds to around 30% of the Medium Energy run total data.

## 6.2   The Quasi-Elastic-Like Signal

As discussed in section 2.2.1 a neutrino CCQE event is defined by the scattering of a neutrino with a free or bound nucleon via the exchange of a charge vector $W^{\pm}$. However, the vector boson can be absorbed by a nucleon-nucleon correlation. Since the detector can only see the final state particles we choose in this analysis to use the definition of quasi-elastic-like events. A quasi-elastic scatter from a correlated pair can cause the ejection of additional nucleons. Final
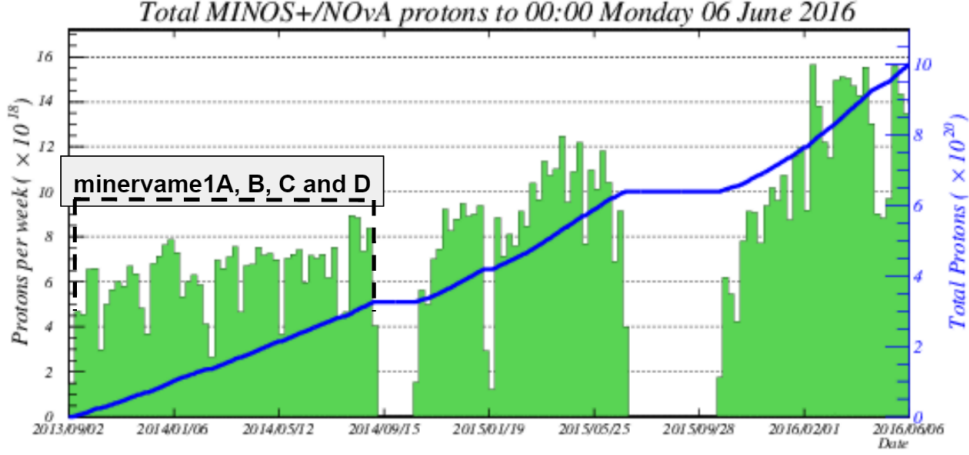
$99.81 \times 10^{19}$ POT - Sep 6, 2013 – Jun 5, 2016

Figure 6.1: Medium energy run Protons Per Target delivery by the accelerator division. The period indicated by the dotted line shows the data used in this analysis

state interactions in which hadrons produced in an initial interaction may re-interact as they propagate through the nucleus.

Figure 6.2 shows a artistic representation of Final-state interactions. A neutron, resulting from the primary QE antineutrino proton interaction, need to escape the nucleus before leaving a signal in the detector. A secondary interaction may produce a final state that include an extra pion. This final state cause the event to be excluded in the CCQE-Like signal definition (figure 6.2a). Conversely, a Ressonant antineutrino proton interaction produces a Delta ressonance, withim the nucleous the $\pi^0$ can be absorbed leaving a muon and neutron final state. This event would be selected into the CCQE-Like signal definition (figure 6.2b).

There is thus no direct one-to-one correlation between final states (which we can attempt to detect) and the initial interaction type that we are attempting to identify. Quasi-elastic-like events are those whose final-state signature matches that of a quasielastic scatter. Our quasi-elastic-like signal definition is neutrino events that have a final state with:

- one negative muon

- any number of nucleons (protons or neutrons)

- no pions, kaons or mesons in the final state

- no heavy baryons in the event

This signal definition permit the proton produced to be above or below the tracking threshold of the MINER$\nu$A detector. We accept events with any number of reconstructed tracks.

54
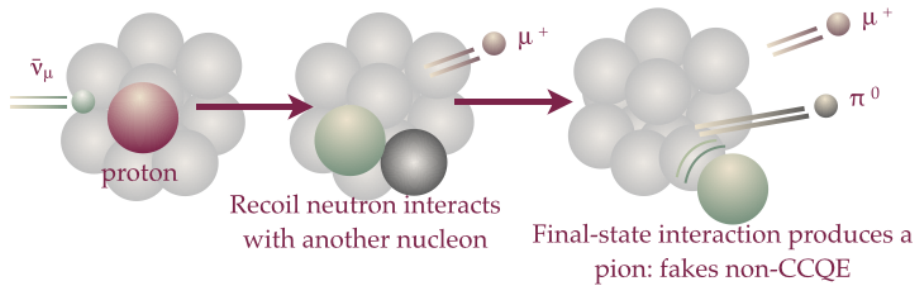
(a) A neutron produced in a quasi-elastic interaction could produce a pion by interacting with another nucleon as it exits the nucleus.
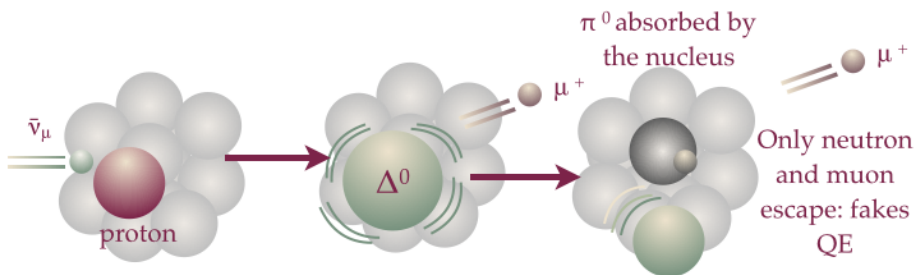


(b) A pion produced in an initial resonant interaction may re-interact and become absorbed within the nucleus, leading a quasi-elastic-like final state of just the muon and neutron

Figure 6.2: Final-state interactions. (a) QE process with pion in the final state and (b) Resonant process with a QE-like final state. Reproduced from [84].

The number of tracks distributions in the selected sample is shown in Figure 6.3. The sample selection process we treat differently samples with different multiplicity, see section 6.3.8 for more details.

## 6.3   CCQE-like Event Selection

Charged current events originating from neutrino interactions inside MINER$\nu$A are the starting point of the event selection procedure needed for this analysis. The ultimate goal is to obtain charged current events that bear a topology that defines the quasi-elastic like interaction events. A number of selection criteria are imposed for events that meet this requirement.
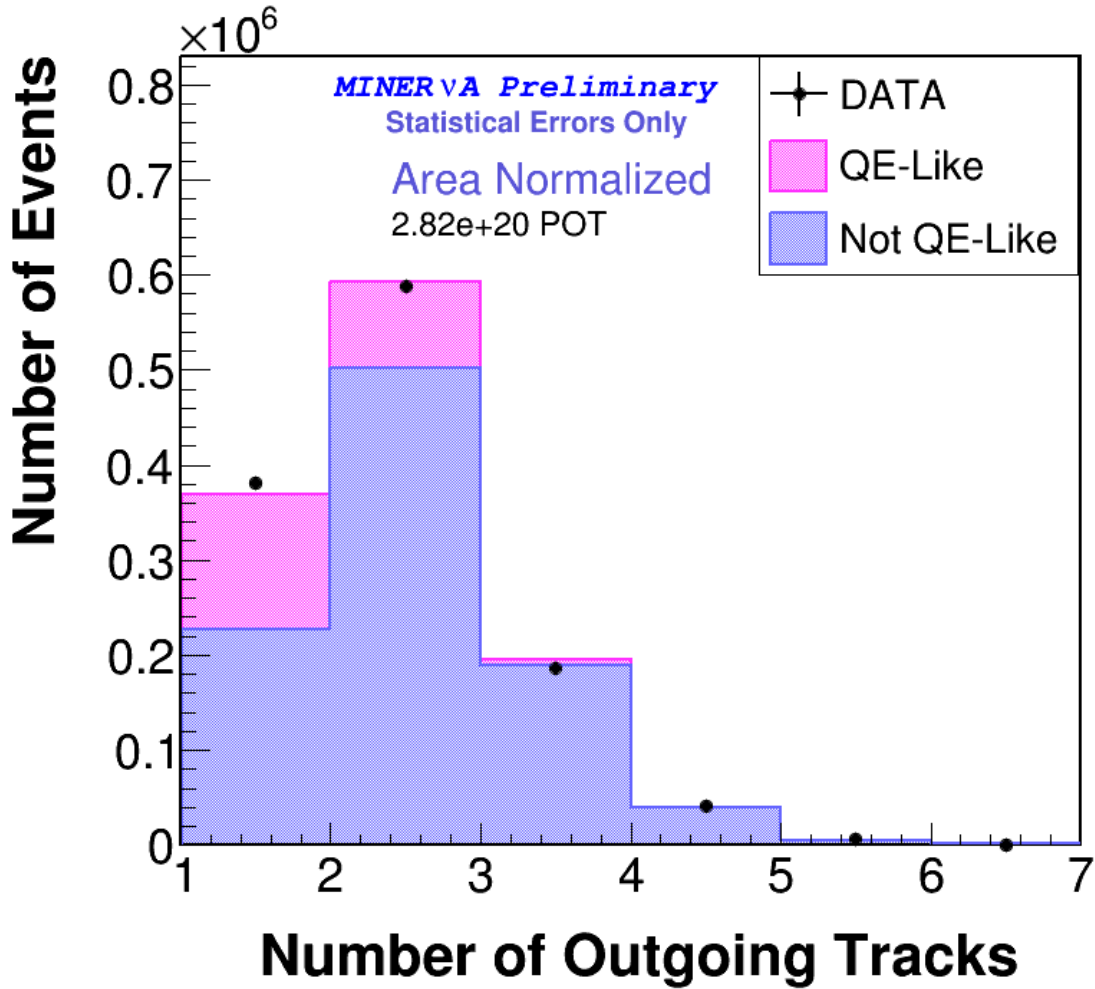
Figure 6.3: Number of outgoing tracks in events after first steps of sample selection.

### 6.3.1 Fiducial Volume

As described in section 3.2.3 the MINERνA detector has an active tracker region core. The first criteria applied to this analysis is to consider only events that include interactions originated in this region.

The fiducial volume is several modules long, along the length of the detector. It extends from module 27 to module 80. Based on a coordinate system that has its origin just before the veto detector this extends for almost 2.5 m (from 5990.0 mm to 8410.0 mm). The maximum extent in the X-Y plane, perpendicular to the length of the detector (Z axis), is required to be no more than 850.0 mm. This is referred to as the apothem. This fiducial volume requirement leads to most of the event information being present inside a well understood and calibrated region of the detector and avoids edge effects or escape of considerable information near the edges of the detector.

## 6.3.2 MINOS Matching

The core of the analysis presented here is the measurement of the $Q^2$, based on the kinematics of the charged lepton originated in a charged current neutrino interaction. Since the NuMI beam line is designed to produce muon neutrinos we need to identify and measure the produced muon kinematics. Each muon originating from a neutrino interaction vertex inside MINER$\nu$A is considered as the primary muon and must be matched to a corresponding muon track in the MINOS detector. Figure 6.4 shows a schematic of a quasi-elastic event, with a muon going into the MINOS near detector. See section 5.4 for details about the muon reconstruction.
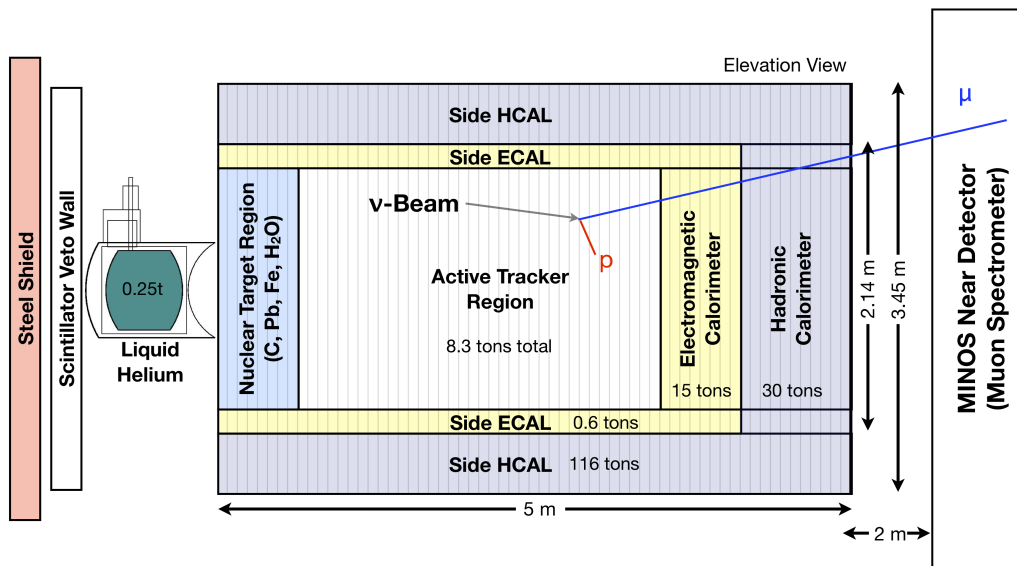


Figure 6.4: Schematic of a quasi-elastic event in the MINER$\nu$A detector. The event interaction vertex is inside the fiducial volume, the muon is going into the MINOS Near Detector and the proton is contained in the MINER$\nu$A detector.

## 6.3.3 Dead Time

The detector readout electronics can experience some dead time after an event has been recorded. A consequence of this can be that the upstream part of a track may not be detected. This can be especially problematic in the case of rock muons. If dead time leads to the upstream part of one of these tracks not being detected, it will appear as if this muon track started part way through the detector, mimicking the signal of a CCQE event.

We can measure this projecting the muon track upstream by two modules and checking whether the electronics corresponding to each of the strips intersected by the projection or their immediate neighbors were experiencing dead time. If two or more of these strips were in dead time during the event, the event is rejected.

## 6.3.4 Helicity

To protect the analysis of the antineutrino contamination present in the beam, we require the events to contain the proper charged lepton helicity. The MINOS detector is magnetized so the muon momentum and charge can be obtained from the track curvature inside MINOS. A metric based on the derived charge ($q$) and momentum ($p$) information is used for selecting muons (as compared to anti-muons).

## 6.3.5 Michel Electron

The event selection requires a search for these Michel electrons in the event (see Section 5.6 for details on the reconstruction). The searches are conducted at the neutrino interaction vertex and at the end of each non-primary-muon track. If a Michel electron is found, the event is tagged.

Michel electrons are created in the Muon decay. The leptonic decay of pion produce muons, which will decay into Michel electrons. Protons do not have any kind of channel to produce Michel electron into the detector, thus the presence of Michel electrons are a distinguishing indicator of the presence of muons and/or pions in the event. Events bearing a Michel tag are are not considered for this analysis.

Figure 6.5 shows the $Q^2$ of the events that were vetoed by this criteria.

## 6.3.6 Isolated Blobs

From a expected CCQE-like topology there is a minimum number of shower-like activity regions that can be present in the event. The term *blob* is used by MINERνA to identify a group of clusters that arise from shower-like activity in the detector material. If this group is distinct and away from other groups and the interaction vertex is classified as an isolated blob.

This analysis use this isolated blobs as a topological cut for selecting quasi-elastic-like events (see Figure 6.6). Only one such isolated blob is permitted by event.
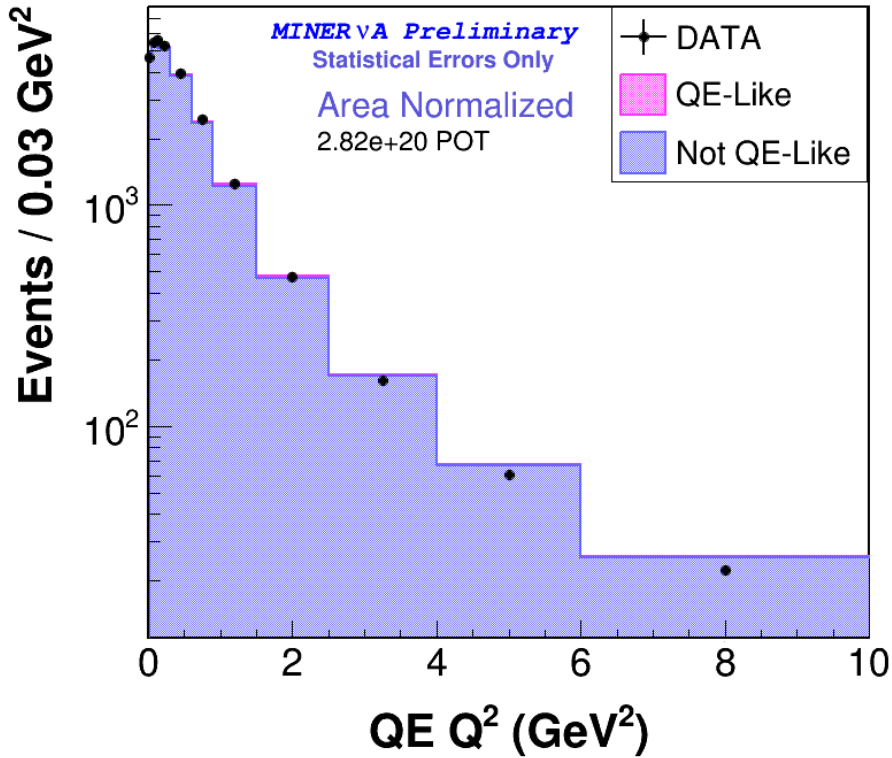
Figure 6.5: Events with at least one Michel Electron identified, all events in this plot were vetoed from the selection.

### 6.3.7 Proton Identification

All reconstructed non-primary-muon tracks are required to pass the proton identification selection criteria. This identification is based on a metric derived from the energy loss profile ($dE/dx$) tool. Based on how closely the energy loss profile of a non-primary muon track resembles that of a decelerating pion or proton, the dE/dx tool returns its best guess of the type of particle associated with the track. This metric is referred to as the proton "$dE/dx$ score" (see Equation 5.1) and it ranges in values from 0.0 to 1.0. High proton scores, e.g. 0.8 or higher, signify a well identified proton track. Low proton scores, e.g. 0.2 or lower, point to particle tracks that are probably not protons but, maybe pions or electrons. The most energetic proton in the event is designated as the primary proton.

The identification on the basis of proton scores is a sliding cut and depends on the four-momentum transfer ($Q^2$) of the event as shown in Table 6.1. Figure 6.7 shows the proton range score for each $Q^2$ range in the table. This sliding cut is introduced in an effort to include protons from high $Q^2$ events which might endure multiple scattering or interactions and then be identified with low scores. As larger the four-momentum transfer of the event, lower is the score for protons reconstructed in that event. Including these protons improves the efficiency
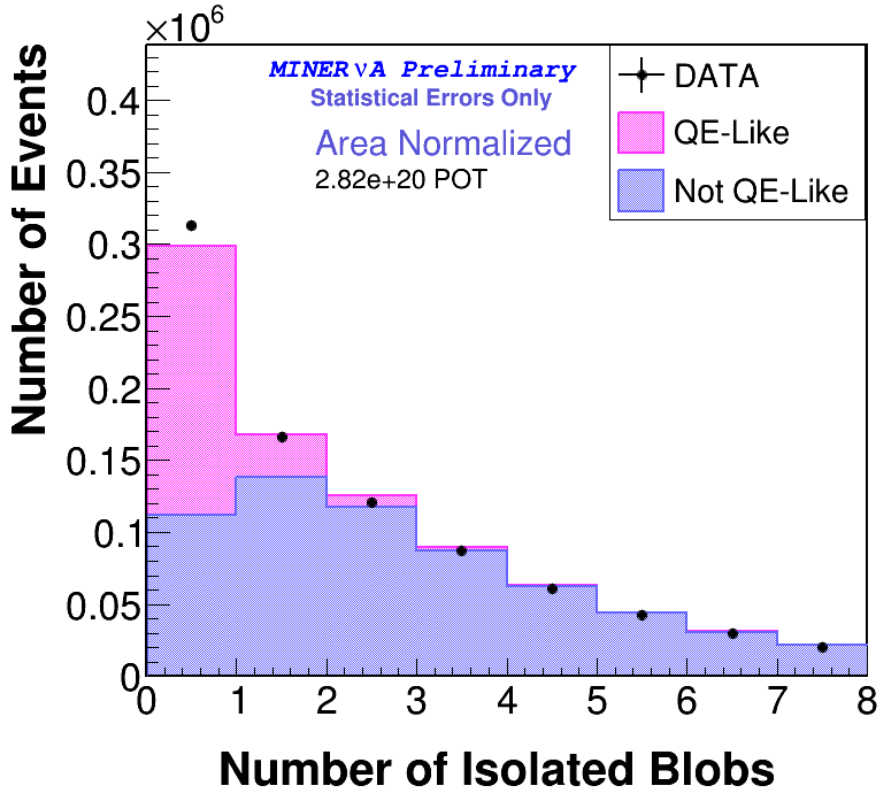
Figure 6.6: Number of isolated blobs. Events with more then one isolated blob are rejected.

of the event selection.

In the case of an event having more than one reconstructed non-primary muon track, all the tracks are subject to the proton identification proccess. The $dE/dx$ scores criteria for identifying the secondary protons is exactly the same used for the primary protons. The secondary protons have less kinetic energy than the primary proton in the event.

| $Q^2$ $(GeV^2)$ | Proton Range Score |
|---|---|
| $0.0 - 0.2$ | 0.30 |
| $0.2 - 0.3$ | 0.25 |
| $0.3 - 0.5$ | 0.20 |
| $0.5 - 0.6$ | 0.15 |
| $0.6 - 10$ | 0.00 |

Table 6.1: Proton Target score accepted versus $Q^2$ in $GeV^2$.

(a) $Q^2 GeV^2$ 0.0-0.2      (b) $Q^2 GeV^2$ 0.2-0.3      (c) $Q^2 GeV^2$ 0.3-0.5

(d) $Q^2 GeV^2$ 0.5-0.6      (e) $Q^2 GeV^2$ 0.6-10.0
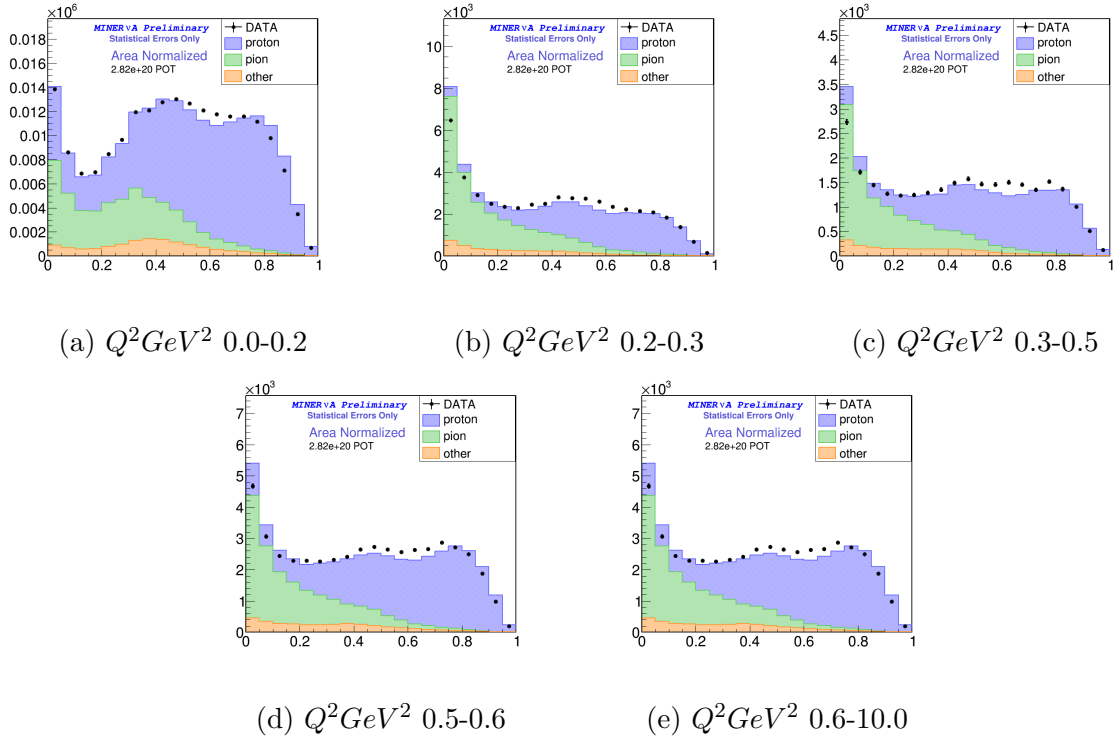
Figure 6.7: Proton range score as a function of $Q^2$

## 6.3.8 Recoil Energy

Quasi-elastic interactions are consistent with low recoils. For this analysis the recoils in the reconstructed events are classified into two groups according their location relative to the interaction vertex. The recoil within a certain designated radius of the interaction vertex is designated as the *vertex recoil* as opposed to the "non-vertex recoil" that lays away from the designated vertex region. To avoid biases arising due to differences between the simulation and data the event selection criteria is insensitive to this vertex recoil. The "non-vertex recoil" is used for deciding which events to keep.

A parametrization of the non-vertex recoil as a function of the reconstructed $Q^2$ of the event is obtained by studying the non-vertex recoil of events whose topologies are similar to those of quasi-elastic interactions. If the event under consideration possesses a non-vertex recoil that is less than that predicted by the parametrization at its reconstructed $Q^2$, it passes this selection criteria. If the non-vertex recoil is larger than what the parametrization predicts, the event is discarded. Figure 6.8 shows the parametrization split in two sub-samples: the first sub-sample is for events with only one muon reconstructed and the second sub-sample is for events where there is at least one proton reconstructed.

(a) QE-like 1 track

(b) non-QE-like 1 track

(c) QE-like 2 track

(d) non-QE-like 2 track
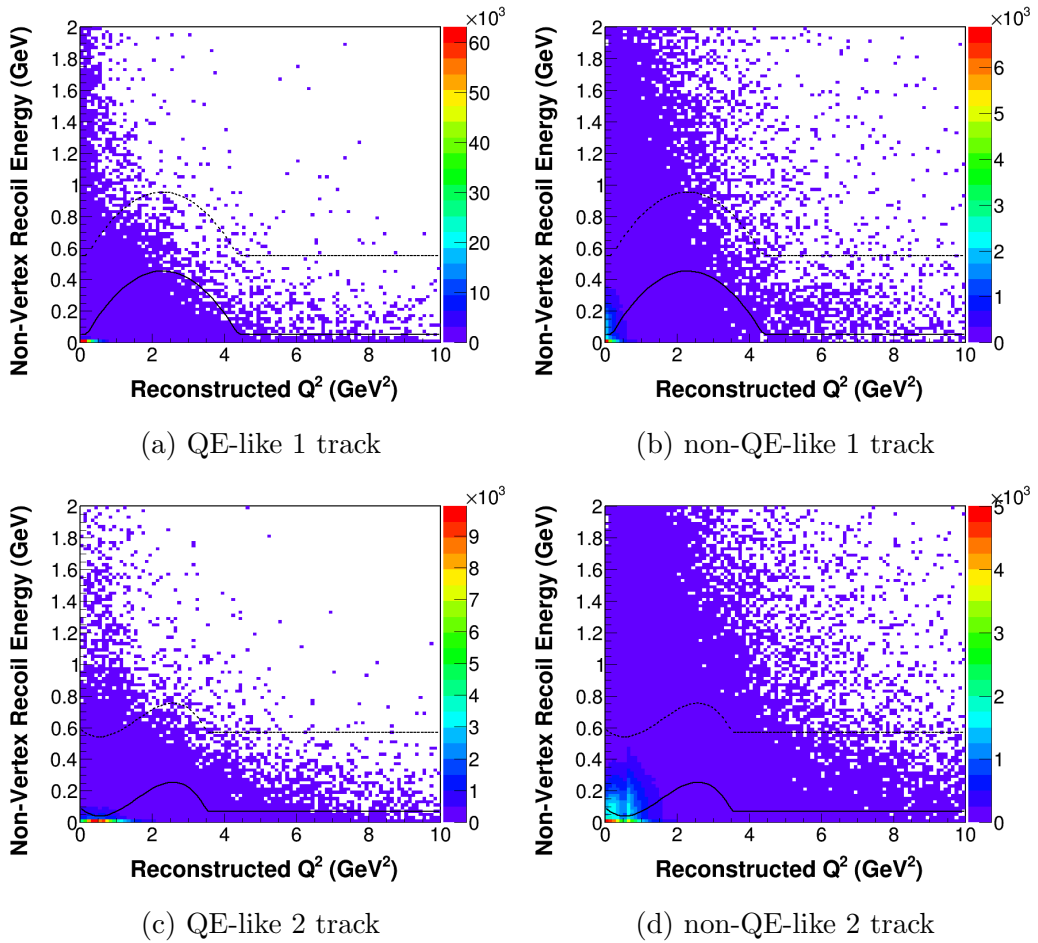
Figure 6.8: Recoil Energy cut as a function of $Q^2$. The plots on the left show the quasi-elastic like events (blue dots) in this phase space and the plots on the right the background (not quasi-elastic-like events). Events below the solid line are accepted. The dotted line is just a reference above 500 MeV.

### 6.3.9 Final sample

Each one of the cuts has an effect in the signal selection efficiency and purity of the sample as shown in Figure 6.9.

Figure 6.10 shows an event candidate after passing all event selection cuts. The long track is the muon going into MINOS and the short track is the proton candidate. Figures 6.11 shows the data and Monte Carlo after all event selection cuts for the sub-sample where only the muon was reconstructed and for the sub-sample where the muon and at least one proton was reconstructed . The total number of quasielastic like event candidates is 75,312 and the estimated purity is 78%.
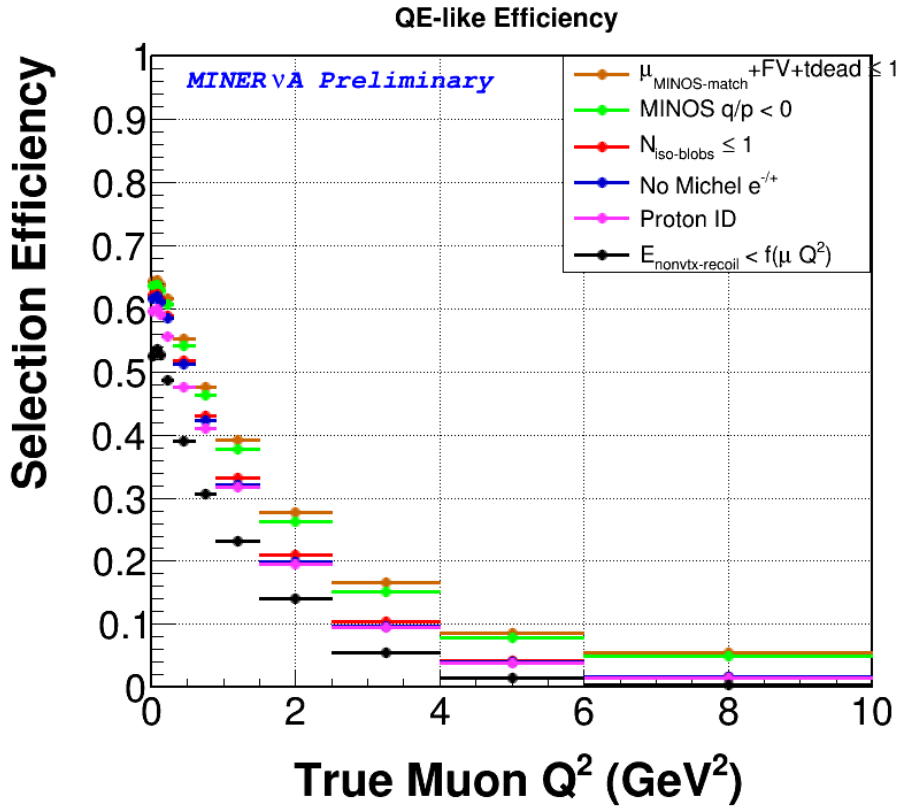
(a) QE-like selection efficiency
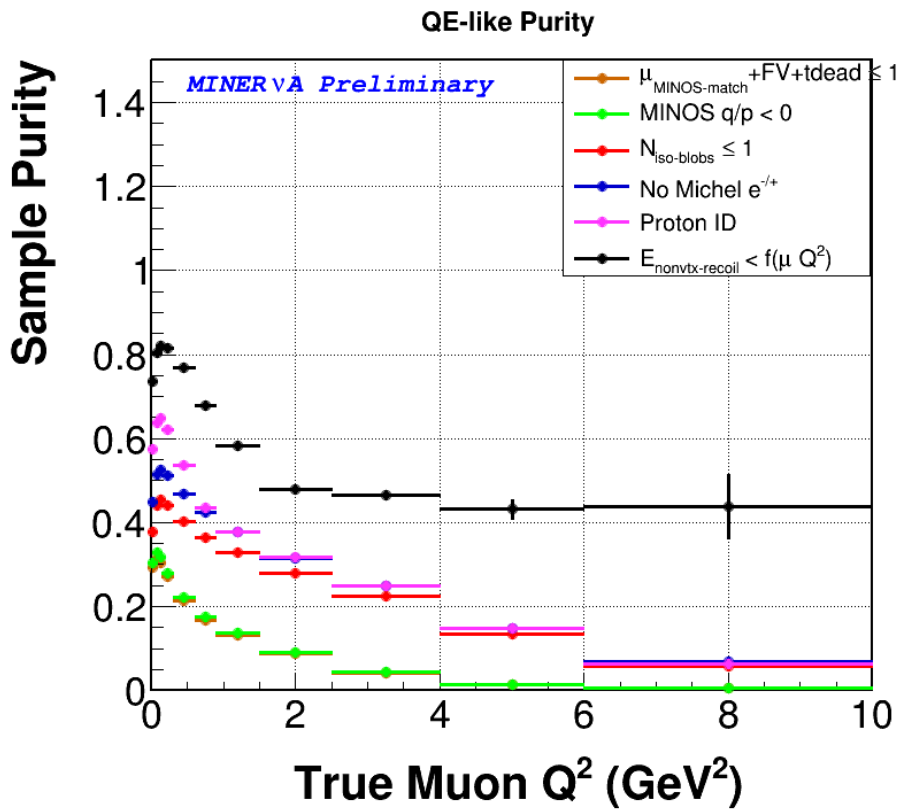


(b) QE-like signal sample purity

Figure 6.9: Efficiency and purity of the selected sample cut by cut

64
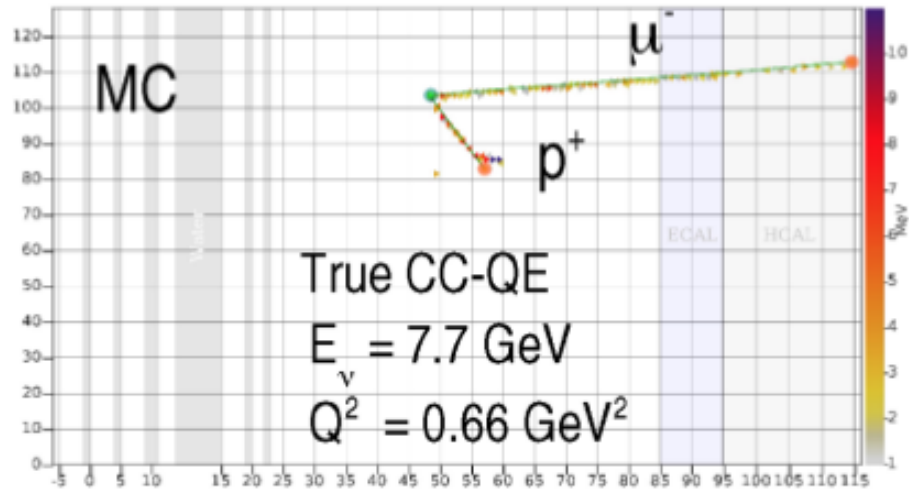
Figure 6.10: Event display candidate after passing all selection criteria
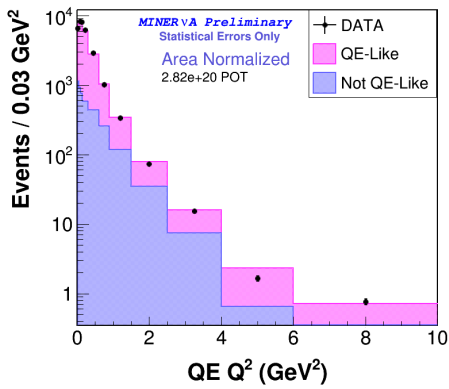


(a) QE-like 1 track
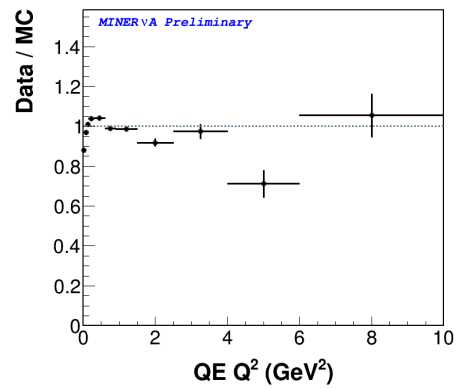


(b) QE-like 1 track ratio
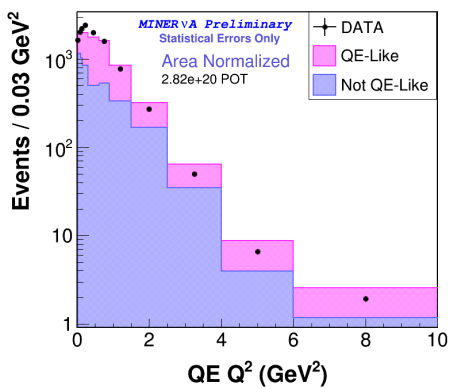


(c) QE-like 2 track
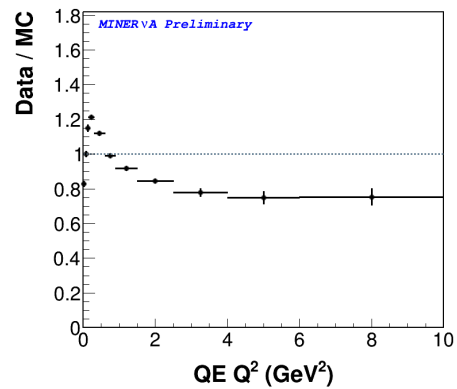


(d) QE-like 2 track ratio

Figure 6.11: $Q^2$ after all sample selection cuts for both multiplicity samples

# Chapter 7

# Measuring the Differential Cross section $d\sigma/dQ^2_{QE}$

This chapter describes the measurement of the $\nu_\mu$ differential cross section of charged current quasi-elastic-like (CCQE-like) interactions on plastic scintillator in the MINER$\nu$A detector.

The quasi-elastic-like diferential cross section in the $i^{th}$ bin of $Q^2$ is given by:

$$\left(\frac{d\sigma}{dQ^2_{QE}}\right)_i = \frac{1}{\Phi_\nu \times T_n} \times \frac{1}{(\Delta Q^2_{QE})_i} \frac{\sum_j U_{ij}[N_j^{data} - N_j^{bg}]}{\varepsilon_i} \tag{7.1}$$

where:

- $\Phi_\nu = \int \phi(E_\nu)dE_\nu$ is the total neutrino flux over the region which contributes to the event sample.

- $T_n$ is the total number of neutron targets in the considered fiducial volume.

- $(\Delta Q^2_{QE})_i$ is width of the $i$th $Q^2_{QE}$ bin.

- $N_j^{data}$ is the measured distribution of selected CCQE-like event in bin $j$ of reconstructed $Q^2_{QE}$.

- $N_j^{bg}$ is an estimate of the distribution of background events present in the selected sample in bin $j$ of reconstructed $Q^2_{QE}$.

- $U_{ij}$ is a matrix that describes the migration from the true $Q^2_{QE}$ bin $j$ to the reconstructed $Q^2_{QE}$ bin $i$, due to finite resolution and relistic biases of the reconstruction.

- $\varepsilon_i$ is the efficiency for reconstructing and selecting signal events as a function of the true variable.

In order to calculate the cross section from the number of reconstructed events identified as CCQE-like candidates we make a correction for expected background rates, detector acceptance, efficiency and known kinematic smearing effects in the reconstruction. The resulting distribution is then normalized for flux and number of targets.

# 7.1 Background Tuning and Subtraction ($[N_j^{data} - N_j^{bg}]$)

The MC simulation allows us to predict the level of background that was not suppressed completely by the QE event selection described in Chapter 6. This background consists, in a large scale, of resonance pion production and deep inelastic scattering interactions where the recoil final state particles (mostly pions):

- were wrongly reconstructed as protons,

- are contained in the region around the interaction vertex or

- are absorbed before exiting the atomic nucleus.

the background events mimic the topology of the signal.

An acceptable way to predict the amount of background in the data is to assume this fraction was the same as the simulation for the same bin. However, in doing this, we are very reliant on the simulation's ability to correctly predict the strengths of signal and background processes. MINER$\nu$A 's charged pion production analysis [85] suggests that GENIE over-predicts the rate of resonant pion production, our most common background. In order to protect against this, we instead use a data-driven fitting procedure to determine the relative fractions of signal and background in our data, by determining the fractions of signal and background processes that would best match our data's shape.

The result of background subtraction is reconstructed distributions corresponding to only CCQE-like events, plotted vs the reconstructed variables (without correction for any mis-reconstruction due to detector effects, or for loss of efficiency due to the detector's or the reconstruction algorithm's limitations).

## 7.1.1 Background Tuning

In order to constrain the background predictions a template fit of background distributions in the simulation is done. The fit is performed on Recoil Energy distributions, which are divided into *signal* and *background*. Due to the fact that the kinematics of events without a reconstructed proton and with one or more reconstructed protons are different, the fits are done independently for both sub-samples and merged after subtracting the background.

For both sub-samples, 11 bins of $Q^2_{QE}$ are used: 0.00-0.05, 0.05-0.10, 0.10-0.15, 0.15-0.30, 0.3-0.6, 0.6-0.9, 0.9-1.5, 1.5-2.5, 2.5-4.0, 4.0-6.0, 6.0-10.0, in units of $GeV^2$. Figure 7.1 shows the ratio between Monte Carlo and data distributions before and after the fit for the first $Q^2$ bin for both sub-samples.

The fit returns the best relative normalization factors for each signal and background template. A weight for each fit is then computed in the following way:

$$w_i = \frac{f_i^{\text{after fit}}}{f_i^{\text{before fit}}} \tag{7.2}$$

where $w_i$ is the computed weight in the bin $i$ and $f^{\text{before fit}}$ ($f^{\text{after fit}}$) represent the fraction of simulated background in the selected recoil sample before (after) the fit.

This procedure is the same applied in MINER$\nu$A previous CCQE results [84] [86] [87].

### 7.1.2 Background Subtraction

Once we have the background constrain weights, the estimated background in data is given by:

$$N_{j,data}^{bg} = w_j \frac{N_{j,MC}^{bg}}{N_{j,MC}} N_{j,data} \tag{7.3}$$

where $N$ is the number of events for bin $j$ and $w$ is the corresponding weight as calculated in the last section. The background subtracted data for each sub-sample is:

$$N_{j,data} - N_{j,data}^{bg} = (1 - w_j \frac{N_{j,MC}^{bg}}{N_{j,MC}}) N_{j,data} \tag{7.4}$$

Figure 7.2 and 7.3 show the $Q^2$ distributions for both sub-samples before and after the background subtraction. Figure 7.4 present the $Q^2$ and ratio after the merging of the two sub-samples.

## 7.2 Unfolding Detector Smearing ($U_{ij}$)

In a experimental set no quantity can be reconstructed with infinite precision. Reconstructed quantity (such as the muon energy) may be measured somewhat higher or lower than its true value, and may therefore be reconstructed into a different bin. Without unfolding, a measurement cannot be compared with the results of other experiments.

In this analysis, the quantities we measure are the muon energy ($E_\mu$) and the muon angle $\theta_\mu$ (with respect to the bin longitudinal direction), from which $Q^2_{QE}$ is calculated. The finite resolution in $E_\mu$ and $\theta_\mu$ generates bin migration in $Q^2_{QE}$. We first use MC simulation to construct a migration matrix that contains the probability of the bin migration. This matrix is

specific for each experiment and depends on the design and properties of the detector. Figure 7.6 shows the migration matrix for the chosen $Q^2_{QE}$ bins in the MINER$\nu$A detector. After background subtraction, we correct for $Q^2_{QE}$ bin migration effects due to detector resolution using an unfolding technique based on Bayes theorem [88]. The resulting distribution is shown in Figure 7.5.

## 7.3 Efficiency Correction ($\varepsilon_i$)

We correct the unfolded distribution using the selection efficiency as a function $Q^2_{QE}$ after all selection cuts. The result is shown in Figure 7.7.

The efficiency is the rather complicated convolution of the MINER$\nu$A (and MINOS) detector acceptances, the muon tracking efficiency in both detectors, the muon track matching efficiency between MINER$\nu$A and MINOS, and the signal event selection efficiency of the applied selection. This procedure and calculation is described in Chapter 6 and shown in Figure 6.9 for the $Q^2_{QE}$ for each one of the sample selection criteria.

## 7.4 Flux and Target Normalization ($\frac{1}{\Phi_\nu \times T_n} \times \frac{1}{(\Delta Q^2_{QE})_i}$)

The final step in order to get the cross section is to normalize by:

- flux integrated over acceptance;

- number of neutron targets

- $Q^2_{QE}$ bins width

The flux is simulated as described in section 4.1 and the number of neutron targets within the fiducial volume is $T = 1.516 \times 10^{30}$.

## 7.5 Systematic Errors

The cross section measurement is sensitive to several parameters of the simulation models and the reconstruction. The uncertainties on each of these parameters lead to a systematic error for the cross section.

MINER$\nu$A uses the *Many Universes* method to evaluate the systematic errors. The nominal value of a parameter is shifted by its uncertainty and the cross section is re-calculated in this new scenario. This new scenario is defined in the experiment as a "universe", and each universe cross section can be expressed as:

$$\left(\frac{d\sigma}{dQ_{QE}^2}\right)_{i,universe} = \frac{1}{\Phi_\nu \times T_n} \times \frac{1}{(\Delta Q_{QE}^2)_i} \frac{\sum_j U_{ij}[N_j^{data} - N_j^{bg}]}{\varepsilon_i} \tag{7.5}$$

Equation 7.5 is a variation of equation 7.1 where each of the components in the latest expression with the subscript *universe* can be impacted by these uncertainties. There are different universes for each parameter shifted. If they are shifted once or twice, the $\pm\sigma$ uncertainties are used, otherwise 100 different shifts are selected from a Gaussian distribution with a mean equal to 0 and a width equal to $\sigma$. Each universe has to pass the event selection criteria described in Section 6.3 in order to take into account the effect of such a shift in the selection. In other words we repeat the whole sample selection and cross section calculation for each one of the universes.

For each error a covariance matrix is calculated using the information from these universes:

$$cov_{i,j} = \frac{1}{N} \sum_{k=1}^{N} (x_{ki} - \bar{x}_i)(x_{kj} - \bar{x}_j) \tag{7.6}$$

where, $i,j$ label the bins, $k$ is the universe index, $\bar{x}$ represents the mean value of a particular bin. The systematic uncertainty for a specific bin, is the square root of the covariance matrix

$$\sigma_i = \sqrt{cov_{i,j}} \tag{7.7}$$

The shape component of the systematic uncertainty can be obtained by normalizing each universe to the area of the central value before calculating the covariance matrix.

Although this thesis presents a complete cross section calculation, we does not include a final systematic error calculation. As seen in previous MINER$\nu$A CCQE results [84] [86] [87][89] we expect the uncertainty related to the flux to be dominant in this analysis[1]. The cross section and final state interaction models are the next most important sources of uncertainty. It's clear that nuclear models still do not reproduce the data. Models used in the Monte Carlo affect the background rejection. The known primary sources of systematic uncertainties are: the flux; cross section and FSI models; the muon reconstruction; the detector energy response; the proton reconstruction and the detector mass scale.

## 7.6   Final Result

Figure 7.8 shows the final measured differential cross section in terms of $Q^2$ within the $0-4GeV^2$ interval. The plot includes statistical errors only as can be seen in Figure 7.9.

---

[1]Recent advances with the flux simulation and new studies in progress for the Medium Energy era are expected to have a considerable effect in this component.

## 7.6.1 Comparison to previous MINER$\nu$A results

Figure 7.10 reproduces the CCQE cross section result published by MINER$\nu$A in 2013 [86] for the low energy beam configuration. Although the signal definitions between these two results are similar but not the same a comparison is valid since the analysis presented on this thesis is a natural evolution from the one developed by G. A. Fiorentini. The result from 2013 includes only CCQE events while we use the CCQE-like definition in this thesis. This thesis also includes the proton reconstruction not present in the low energy analysis.

We can notice an expected difference in scale of the cross sections since, as shown in Figure 2.1, the CCQE cross section experiences a strong decline with the increase of the neutrino energy. Moreover, the ratio between data and the GENIE MC presents a similar shape for both results, as expected since the same GENIE model is used for CCQE. Future versions of this analysis will present a more direct comparison with different signal definitions, systematic errors and comparison to different models.
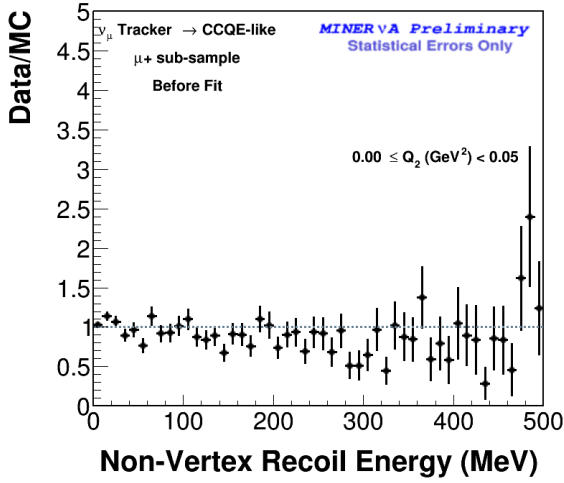
(a) 1 track only sample before tunning
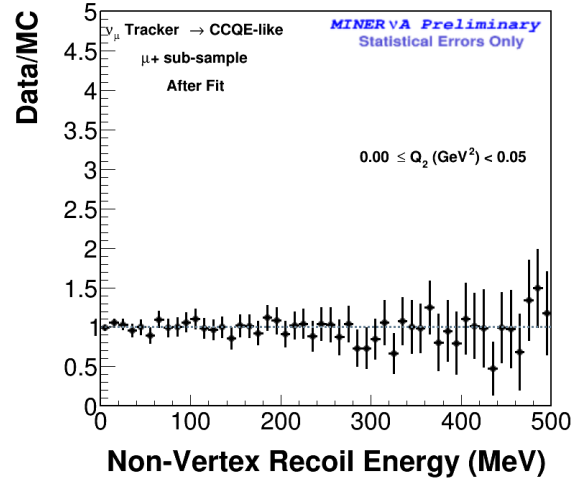
(b) 1 track only sample after tunning
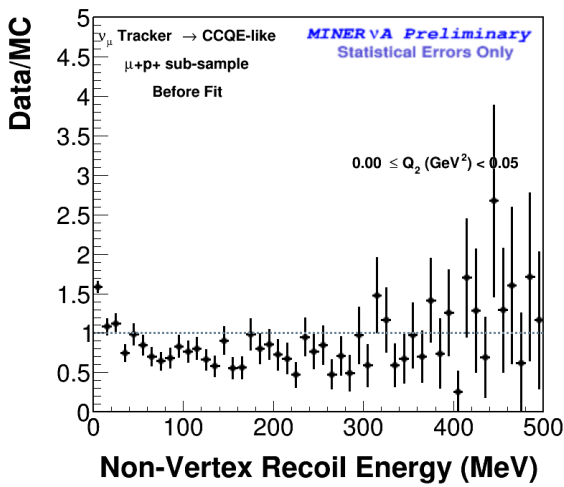
(c) 2 or more tracks sample before tunning
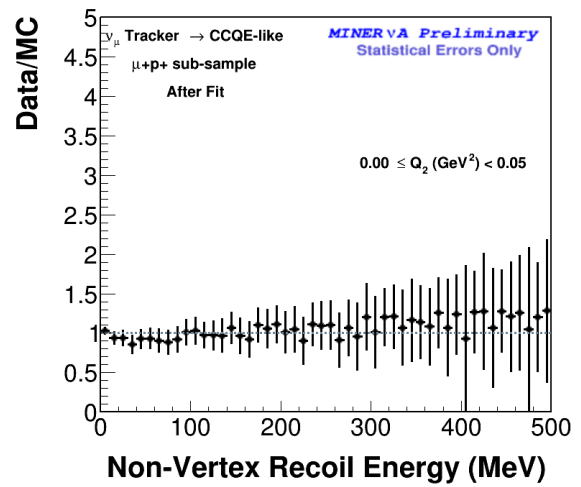
(d) 2 or more tracks sample after tunning

Figure 7.1: Data/MC ratio in the bin $0.00 < Q^2(GeV^2) < 0.05$ for both samples, before and after backgroung tunning
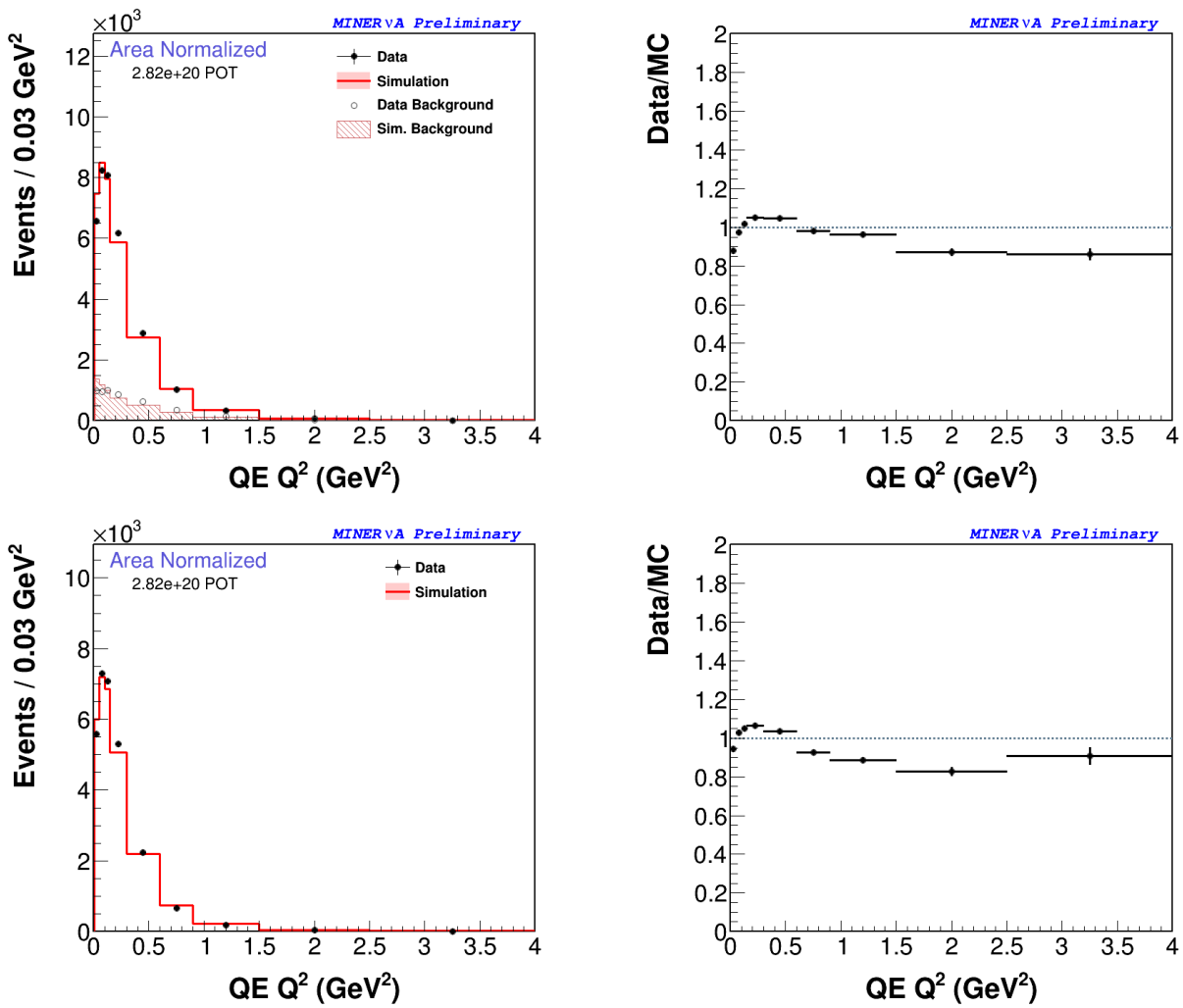
Figure 7.2: $Q^2$ Data and Monte Carlo distribution before (top) and after (bottom) background subtraction for the 1 track only sample
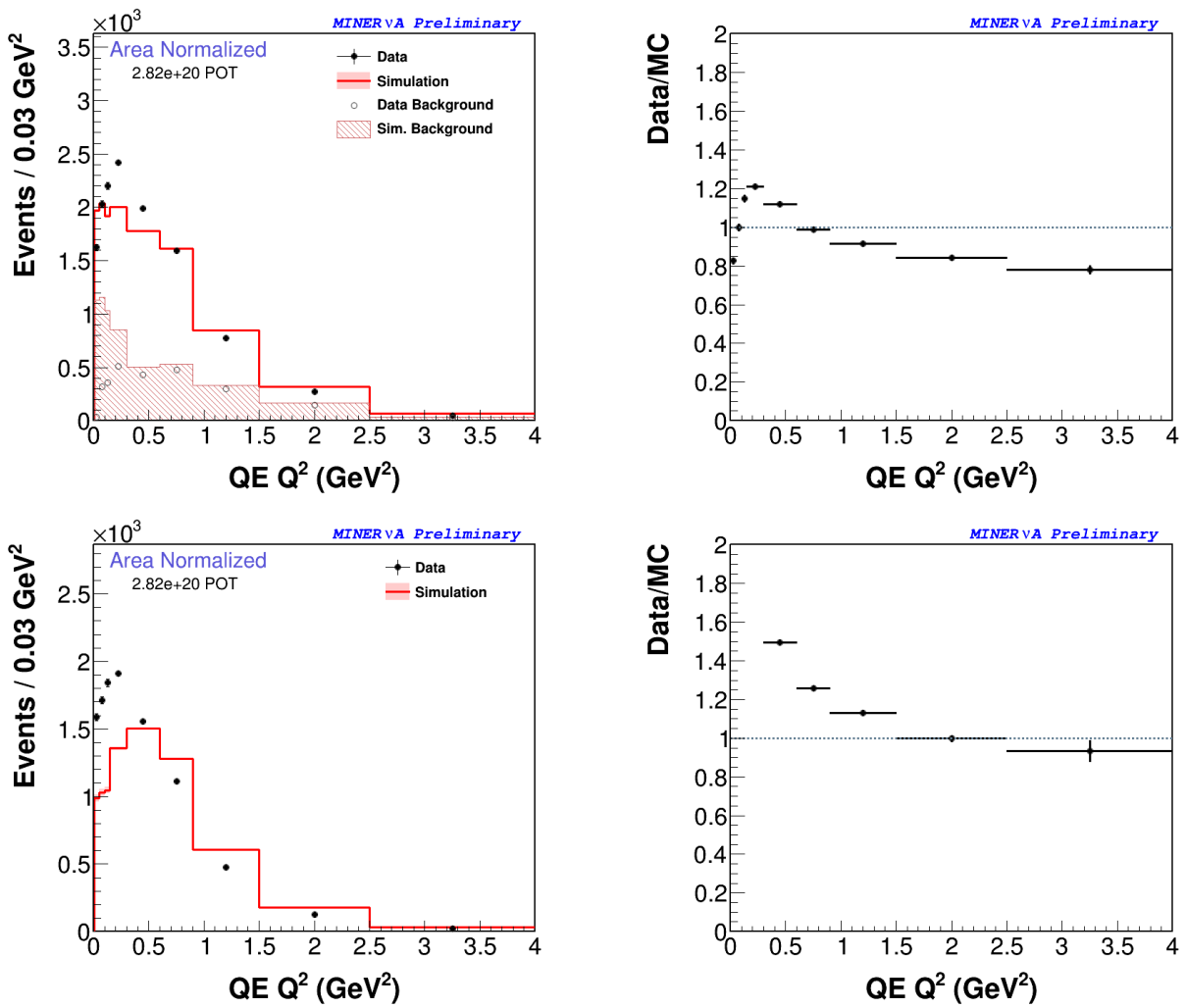
Figure 7.3: $Q^2$ Data and Monte Carlo distribution before (top) and after (bottom) background subtraction for the 2 or more tracks sample
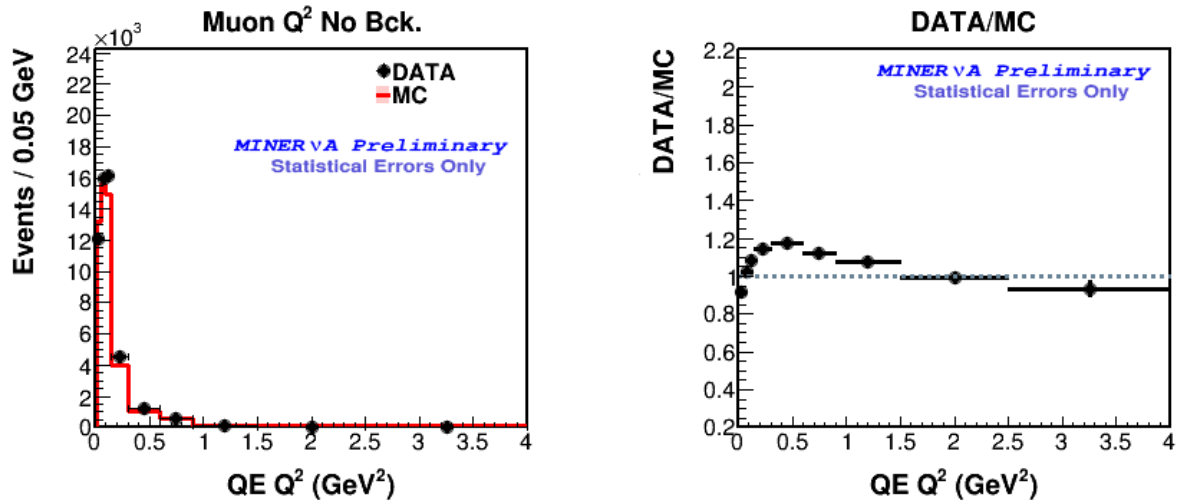
Figure 7.4: Background subtracted distribution of events in bins of reconstructed $Q^2_{QE}$ (left) and ratio between data and MC (right) with statistical errors only after the merging of the two sub-samples
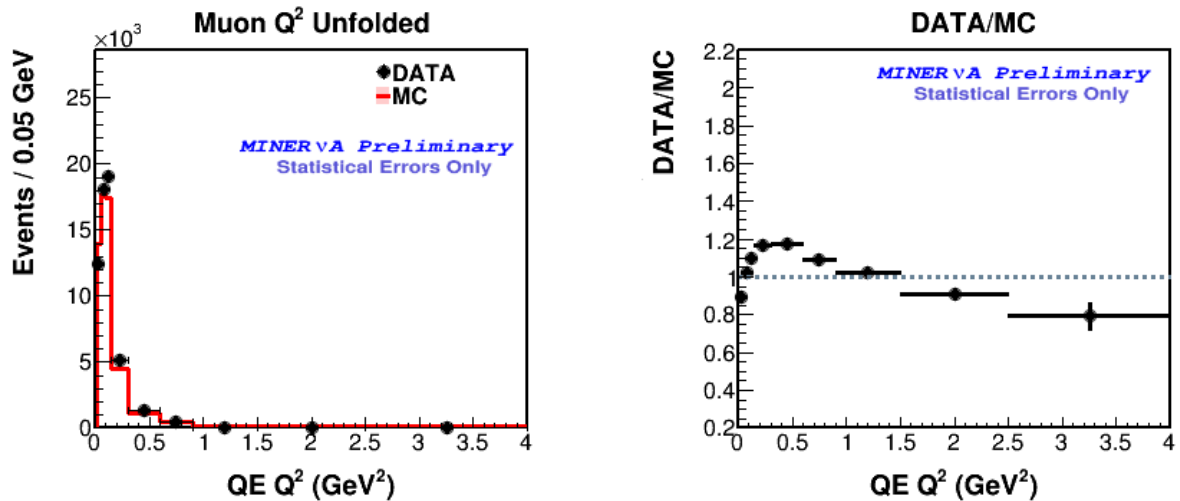


Figure 7.5: Background subtracted and unfolded distribution of events in bins of reconstructed $Q^2_{QE}$ (left) and ratio between data and MC (right) with statistical errors only
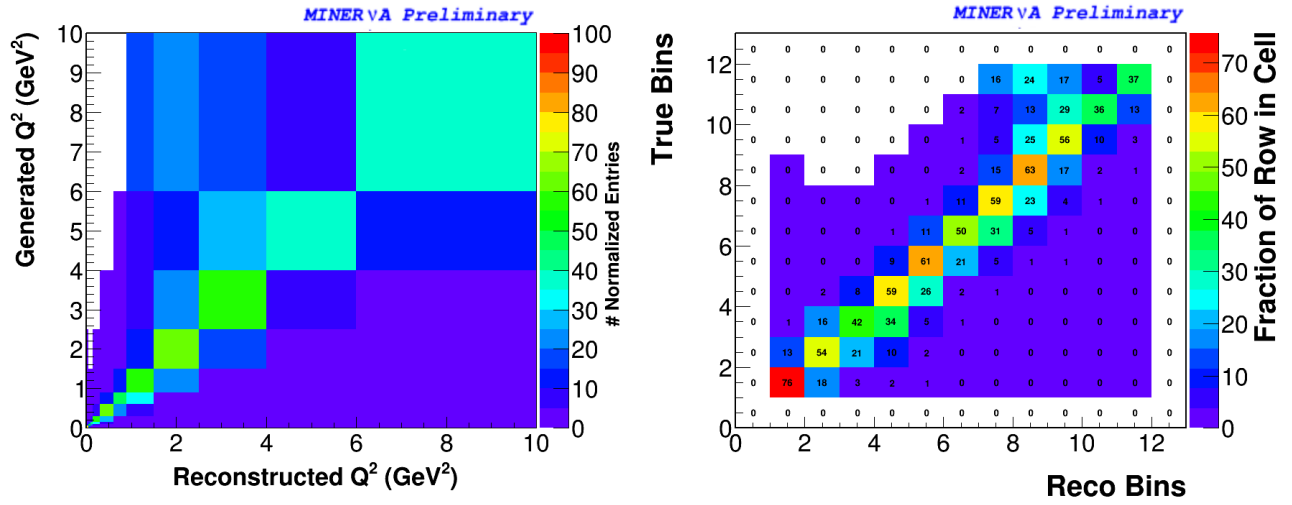
Figure 7.6: Migration matrix for the $Q^2$ bins in the MINER$\nu$A detector. Right plots axis shows the actual $Q^2$ bins in $GeV^2$. Left plots axis shows the number of bins. Notice that underow and overow bins are considered.
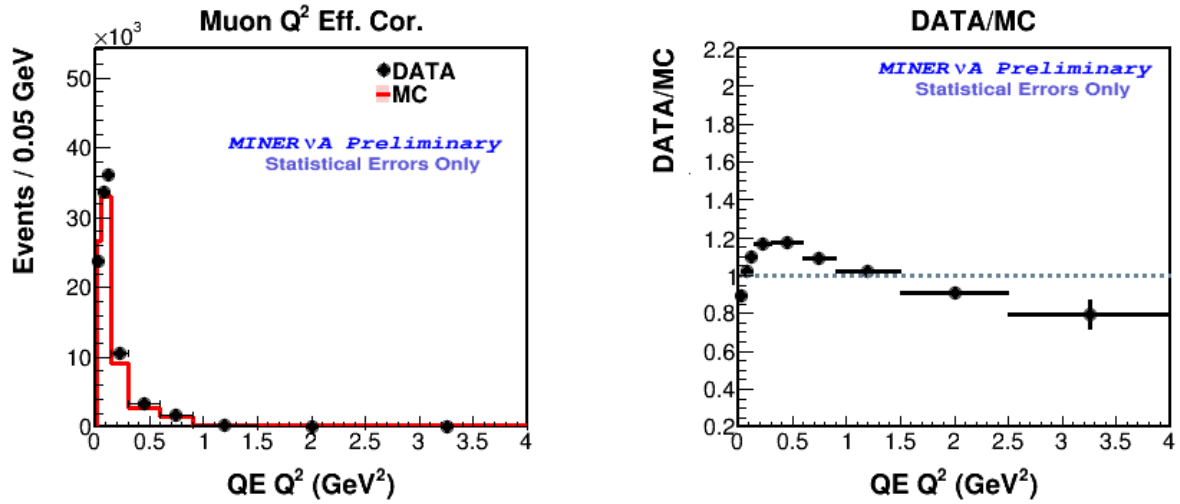


Figure 7.7: Background subtracted, unfolded and efficiency corrected distribution of events in bins of reconstructed $Q^2_{QE}$ (left) and ratio between data and MC (right) with statistical errors only

76
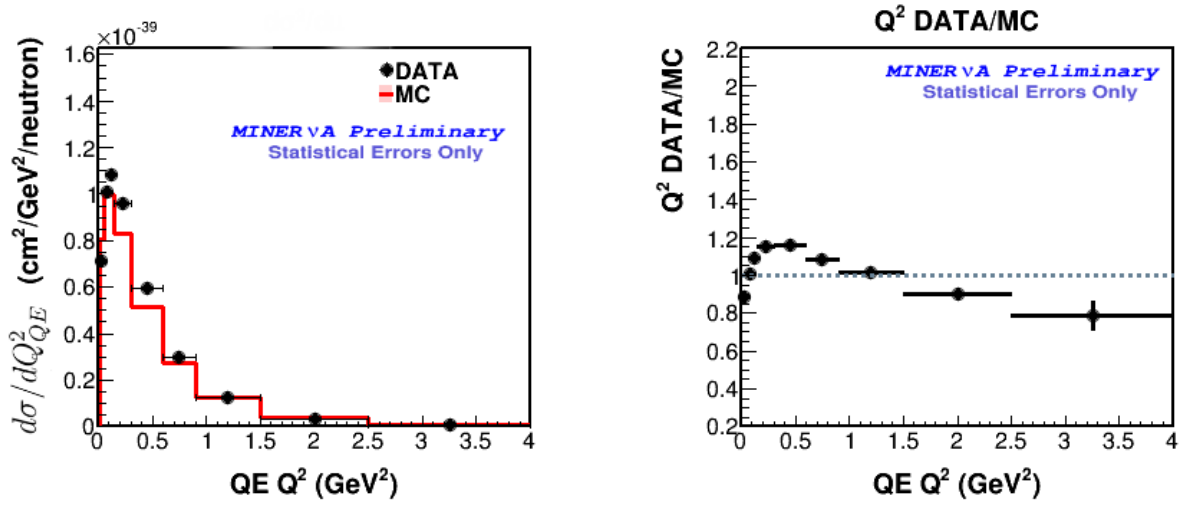
Figure 7.8: CCQE-like cross section for neutrinos in bins of reconstructed $Q^2_{QE}$ (left) and ratio between data and MC (right) with statistical errors only
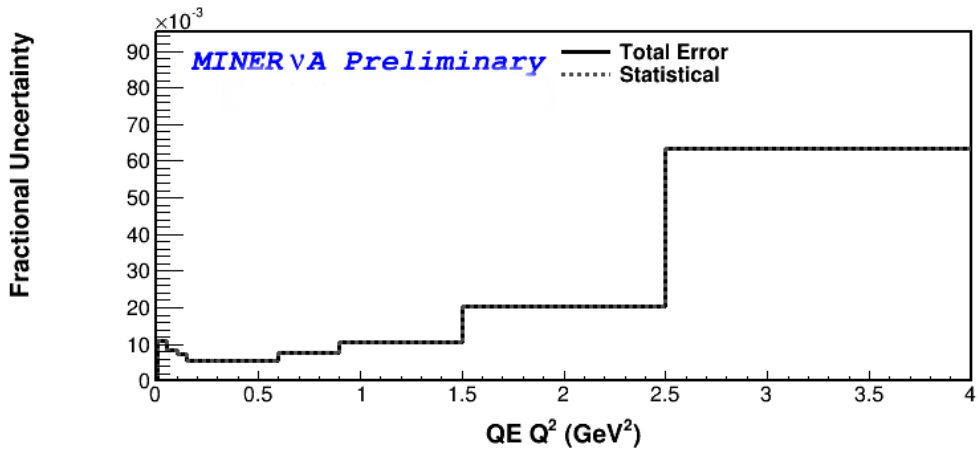


Figure 7.9: Statistical error in the final cross section distribution per $Q^2$ bin
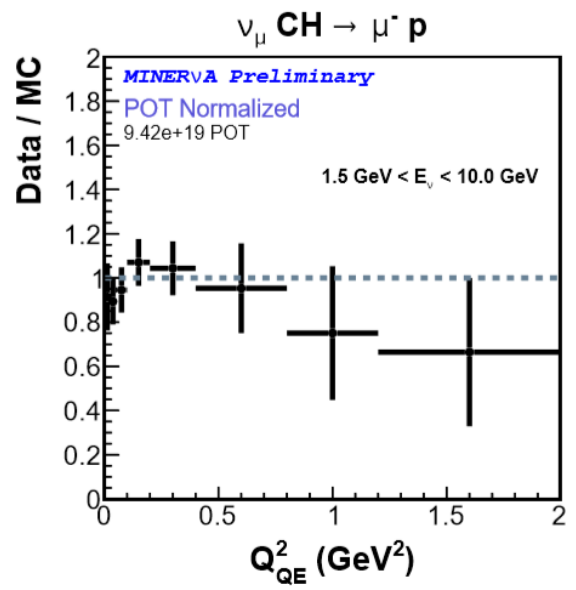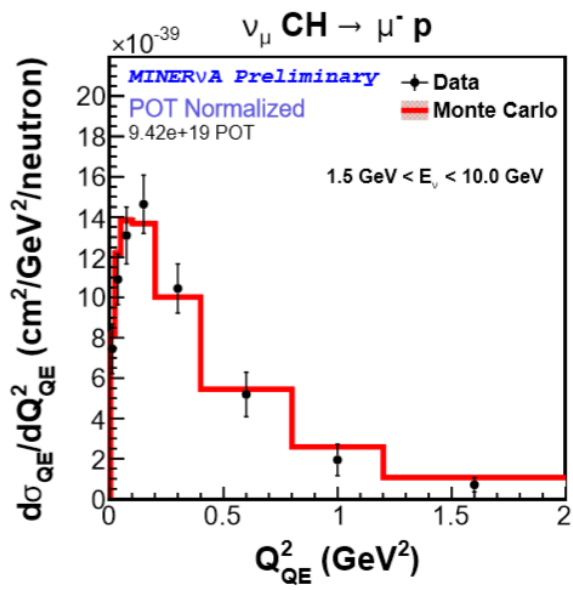
Figure 7.10: CCQE cross section for neutrinos in bins of reconstructed $Q^2_{QE}$ (left) and ratio between data and MC (right) with statistical errors only as published in [86].

# Chapter 8

# Conclusions

In this thesis, we present the first measurement of the single (flux-averaged) differential cross section, $d\sigma/dQ_{QE}^2$, for muon neutrino charged-current quasielastic-like (CCQE-Like) interactions on a hydrocarbon (CH) target using the MINER$\nu$A detector in the NuMI neutrino beam with the new medium-energy ($E_\nu \sim 6$ GeV) configuration at Fermilab. The data used in this analysis represents 1/3 of the total data collected by MINER$\nu$A in the medium-energy configuration of the NuMI neutrino beam.

The selection of muon neutrino CCQE-like interactions is based on the identification of a negative muon and the requirement of low calorimetric recoil energy separated from the interaction vertex. By looking at the calorimetric recoil energy separeted from the interaction vertex, we include in the measurement CCQE-Like interactions with more than one nucleon in the final state that may be due to intranuclear rescattering or correlations between target nucleons. Although this is an analysis in terms of muon observables, the proton is also reconstructed and identified, and Michel electrons are tagged and rejected from the event selection in order to improve the statistics and purity of the sample.

We calculate the single differential cross section $d\sigma/dQ_{QE}^2$ of muon neutrino CCQE interactions and compare it to the current GENIE MC model. This is the first cross section measurement done with the new energy configuration of the NuMI beam and it is a big step forward this new generation of results, not just for MINER$\nu$A but for the whole Fermilab Neutrino program. This result also shows MINER$\nu$A robust reconstruction algorithm as well as simulation procedure.

MINER$\nu$A can use the preliminary results presented in Chapter 7 to address the discrepancies in the cross section measurements reported by NOMAD and MiniBooNE as described in section 2.2.1. Our cross section results can be used to check models implemented in several event generators. Future versions of this analysis will include several improvements. The use of the full data from the NuMI medium-energy configuration will provide a higher statistics and a

better identification of Michel electrons ($\pi^+ \to \mu^+ \to e^+$) will improve efficiencies and sample purities by allowing the rejection of background events with pions in the final state.

# Appendix A

# Summary of contributions to the MINER$\nu$A experiment

This session briefly lists the work and service tasks performed in the MINER$\nu$A Collaboration during the time relevant for the production of the analysis presented in this thesis.

## A.1  Commissioning of the MINER$\nu$A Test Beam II

Following the first MINER$\nu$A project at the Test Beam [90], this new version aims to study the MINER$\nu$A detector response to charged particles in the medium energy era. A smaller version of the MINER$\nu$A detector sits in front of secondary beam in the Fermilab test beam facility. The facility permits the users to ask for specific outputs from the secondary beam. The MINER$\nu$A Test Beam II Project took data of protons and pions in the range of 1 to 8 GeV. The detector is composed by square shaped scintillator planes (build exactly like the ones in the main detector, see session 3.2.3) in different positions to emulate the MINER$\nu$A main detector. Time of flight TOF scintillator counters measure transit time of particles. Hits on Wire Chamber help reconstruct the trajectory of the charged particles.

During commissioning I took part in the following tasks:

- Hardware assembling and testing

- cabling

- Veto wall design assembling test and operation

## A.2  PMT Testing

I participated in the testing of crosstalk of the multianode PMTS that are used for the readout of MINER$\nu$A detector and whose function is described in chapters 3 and 4. Figure A.1 shows that in average we find a crosstalk of 4.8 % for the 4 nearest pixels.
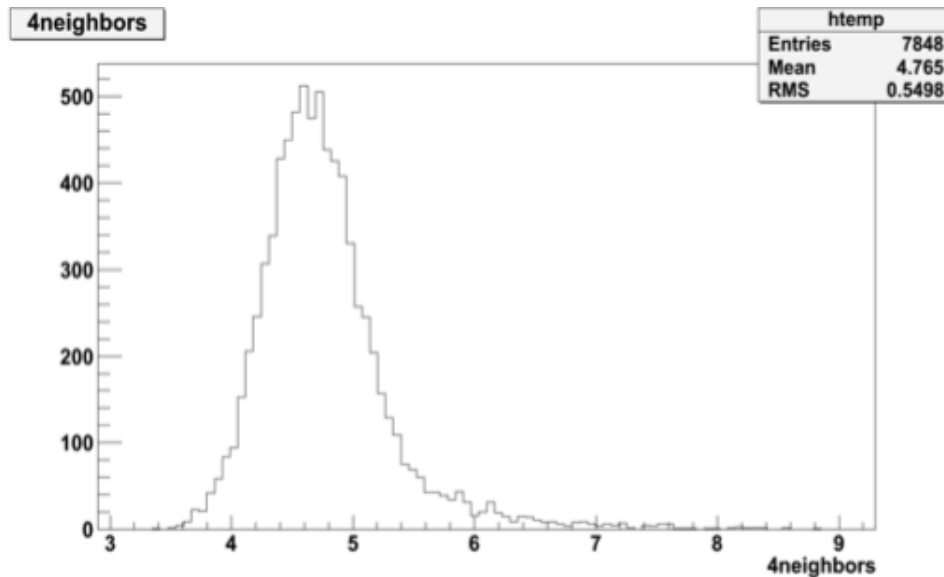


Figure A.1: Crosstalk distribution for the 4 neirest neighborhoods.

## A.3  Cross talk studies

Using the cross talk rejection algorithms on small samples of data and see the effect over different reconstructed kinematic variables (work done with Jeremy Wolcott see figure A.2).

## A.4  Hardware and DAQ maintenance

MINER$\nu$A keeps experts on call weekly. The expert needs to be familiar with all the hardware and software described in Chapter 3 as well as has the knowledge necessary to fixing problems and, eventually, swap hardware parts. I played this expert role several times during my work at MINER$\nu$A .

## A.5  Geometry simulation

As described in session 4.4 we need a detector simulation well functioning in terms of correct geometry. I was the responsible for fixing and assuring the correctness of this simulation.

**Nu Energy**

| | h1 | |
|---|---|---|
| Entries | 15340 |
| Mean | 7.677 |
| RMS | 4.899 |
| Underflow | 0 |

| | h2 | |
|---|---|---|
| Entries | 15140 |
| Mean | 7.745 |
| RMS | 4.898 |
| Underflow | 0 |

*le010z185i no xtalk && clean (1.69e+19)*

*le010z185i xtalk && clean (1.69e+19)*

Area normalized
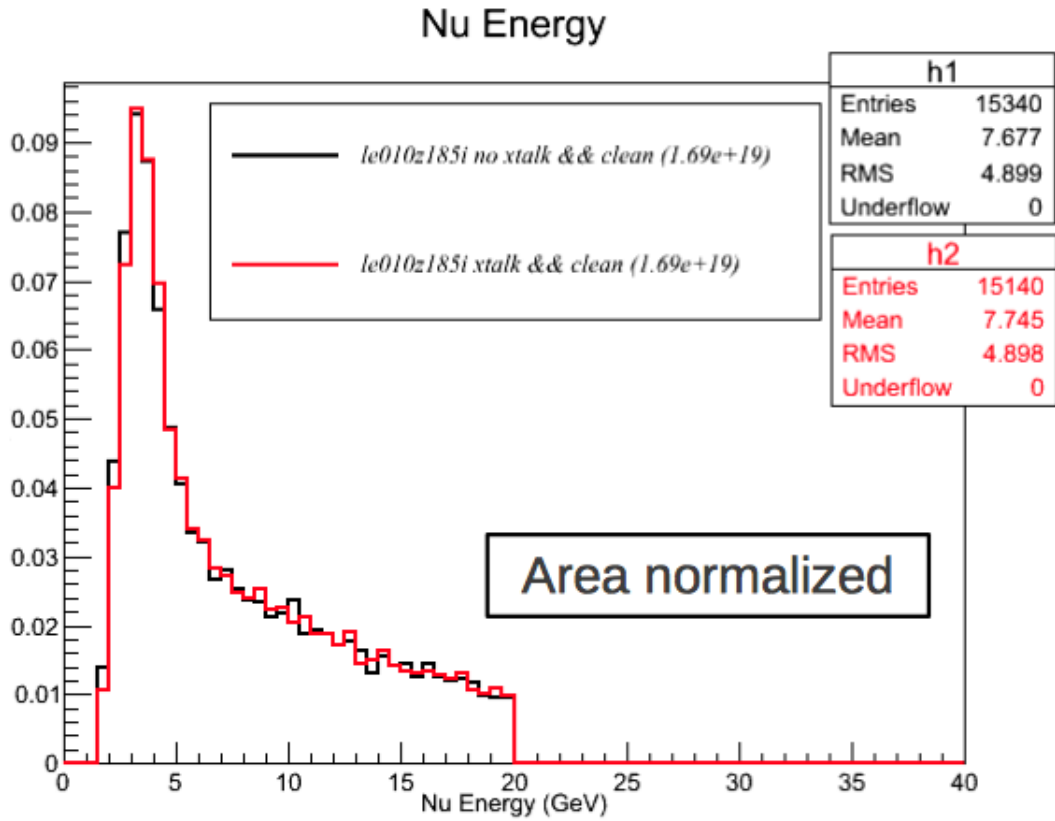
Figure A.2: Neutrino enery distribution for a subsample with (RED) and without (BLACK) cross talk rejection.

## A.6  Data taking Shifts

As any other MINER$\nu$A collaborator I took several hours of shifts during the medium energy configuration run of the NuMI Beam.

Finally it is important to mention that all of the previous studies and algorithms were necessary for the current and future publication goals of MINER$\nu$A .

# Bibliography

[1] Pontecorvo, B., Sov. Phys. JETP, 6, 1957

[2] von Bayer, O. Hahn, L. Meitner, Phys. Zeitschrift, 12, January, 1911, p. 378

[3] Pontecorvo, B., Sov. Phys. JETP, 26, 1968, p. 984-988

[4] Super-Kamiokande Collaboration, Phys. Rev. Lett., 81, 8, p. 1562–1567, 1998

[5] Glashow, S. L. and Iliopoulos, J. and Maiani, L., Phys. Rev. D, 2, 7, p. 1285-1292, 1970

[6] Cabibbo, Nicola, Phys. Rev. Lett., 10, 12, p. 531–533, 1963

[7] Kobayashi, Makoto and Maskawa, Toshihide, Prog. Theor. Phys., 49, p. 652-657, 1973

[8] Pontecorvo, B., Sov. Phys. JETP, 7, p. 172-173, 1958

[9] Maki, Ziro and Nakagawa, Masami and Sakata, Shoichi, Progress of Theoretical Physics, 28, 5, p. 870-880, 1962

[10] DUNE Collaboration, FERMILAB-DESIGN-2016-02, 2015

[11] Zee, A., Phys. Rev. D, 68, 9, 2003

[12] M.C. Gonzalez-Garcia and Michele Maltoni and Thomas Schwetz, Nuclear Physics B, 908, 2016

[13] Double Chooz Collaboration, JHEP, 10, 2014

[14] RENO Collaboration, Phys. Rev. Lett., 108, 2012

[15] Daya Bay Collaboration, Phys. Rev. Lett., 115, 11, 2015

[16] T2K Collaboration, Phys. Rev. Lett., 112, 18, 2014

[17] KamLAND Collaboration, Phys. Rev., D88, 3, 2013

[18] Formaggio, J. A. and Zeller, G. P., Rev. Mod. Phys., 84, 3, p. 1307–1341, 2012

[19] D. Casper, Nuclear Physics B - Proceedings Supplements, 112, 13, p. 161 - 170, 2002

[20] MiniBooNE Collaboration, Nucl.Instrum.Meth., A599, p. 28-46, 2009

[21] T2K Collaboration, Phys. Rev. D, 87, p. 28-46, 2013

[22] D.G. Michael et al. (MINOS collaboration). The Magnetized steel and scintillator calorimeters of the MINOS experiment. Nucl. Inst. and Meth., Phys. Res. Sect. A, 596:190228, (2008).

[23] NOvA Collaboration, FERMILAB-DESIGN-2007-01, 2007

[24] J. Hylen et al., NuMI Technical Design Handbook, Internal NuMI report (2003).

[25] R.A. Smith and E.J. Moniz, Nuclear Physics B, 43, p. 605 - 622, 1972

[26] Whitney, R. R. and Sick, I. and Ficenec, J. R. and Kephart, R. D. and Trower, W. P., Phys. Rev. C, 9, 6, p. 2230 - 2235, 1974

[27] C. Andreopoulos et al., Nuclear Instruments and Methods in Physics Research Section A: Accelerators, Spectrometers, Detectors and Associated Equipment, 614, 1, p. 87 - 104, 2010

[28] Liu, L.C., Phys. Rev. C, 79, 1, 2009

[29] Llewellyn Smith, C.H., Physics Reports, 5, Vol. 3, 1972

[30] K.A. Olive et al. (Particle Data Group), Chin. Phys. C, 38, 090001 (2014)

[31] Wilkinson, Denys H., Nucl. Phys., A377, 1982

[32] Bastian Märkisch, arXiv:1107.3422 [nucl-ex], 2011

[33] NOMAD Collaboration, Eur. Phys. J., C63, p. 355-381, 2009

[34] MiniBooNE Collaboration, Phys. Rev. D, 88, 3, 2013

[35] Juszczak, Cezary and Sobczyk, Jan T. and Żmuda, Jakub, Phys. Rev. C, 82, 4, 2010

[36] Grange, Joe M., PhD Thesis, Florida U., 2013

[37] K2K Collaboration, Phys. Rev. D, 74, 5, 2006

[38] Espinal, X. and Sanchez, F., AIP Conf. Proc., 967, p. 117-122 2007

[39] Dorman, M. and MINOS Collaboration, AIP Conference Proceedings, 1189, 1, p. 133-138, 2009

[40] Aguilar-Arevalo, A. A. and others, Phys. Rev. D, 81, 9, 2010

[41] T2K Collaboration, Phys. Rev. D, 92, 11, 2015

[42] R. Placakyte, Proceedings 31st International Conference on Physics in collisions, 2011

[43] Dieter Rein and Lalit M. Sehgal. Annals Phys., 133, p. 79153, 1981

[44] Rodrigues, P. A, AIP Conf. Proc., 1663, 2015

[45] MINERvA Collaboration, Phys. Rev. D, 91, 7, 2015

[46] Maury Goodman, Advances in High Energy Physics, 2015

[47] D.S. Ayres et al. NOvA: Proposal to build a 30 kiloton off-axis detector to study $\nu_\mu \rightarrow \nu_e$ oscillations in the NuMI beamline. In: (2004). arXiv:hep-ex/0503053

[48] R. M. Zwaska, PhD thesis University of Texas at Austin, 2005.

[49] MINERvA Collaboration, Nucl.Instrum.Meth., A743, p. 130159, 2014

[50] MINERvA Collaboration, FERMILAB-PROPOSAL-0938, FERMILAB-P-938, 2004

[51] Hamamatsu Photonics K.K., Hamamatsu Photonics K.K., Electron Tube Division, 2007

[52] N. Tagget al., Nucl. Inst. and Meth., Phys. Res. Sect. A, 539, p. 668678, 2005

[53] MINERvA Collaboration, Nucl. Instrum. Meth, A694, p. 179-192, 2012

[54] Barrand, G. and others, Proceedings, 11th International Conference on Computing in High-Energy and Nuclear Physics, p. 92-95, 2000

[55] MINOS Collaboration, Phys. Rev. Lett., 112, 19, 2014

[56] MINOS Collaboration, Phys. Rev. Lett., 106, 8, 2011

[57] MINOS Collaboration, Phys. Rev. Lett., 107, 2, 2011

[58] MINOS Collaboration, Phys. Rev. Lett., 110, 25, 2013

[59] MINOS Collaboration, Phys. Rev. Lett., 110, 17, 2013

[60] MINOS Collaboration, Phys. Rev. D, 81, 5, 2010

[61] MINOS Collaboration, Nuclear Instruments and Methods in Physics Research Section A: Accelerators, Spectrometers, Detectors and Associated Equipment, 596, 2, p. 190 - 228, 2008

[62] MINOS collaboration, Phys. Rev. D, 81, 7, 2010

[63] GEANT4 Collaboration, Nucl. Instrum. Meth., A506, p. 250-303, 2003

[64] Aliaga, L., PhD Thesis, College of William and Mary, 2016

[65] C. Alt et al., Eur. Phys. J. C, 49, p. 897-917, 2007

[66] The NA61/SHINE Collaboration, Phys. Rev. C, 84, 3, 2011

[67] Ferrari, Alfredo and Sala, Paola R. and Fasso, Alberto and Ranft, Johannes, CERN-2005-010, SLAC-R-773, INFN-TC-05-11, 2005

[68] T.T. Böhlen and F. Cerutti and M.P.W. Chin and A. Fass and A. Ferrari and P.G. Ortega and A. Mairani and P.R. Sala and G. Smirnov and V. Vlachoudis, Nuclear Data Sheets, 120, p. 211-214, 2014

[69] Barton, D. S. and others, Phys. Rev. D, 27, 11, p. 2580-2599, 1983

[70] Lebedev, Andrey V., PhD Thesis, Harvard U., 2007

[71] Pavlovic, Zarko, PhD Thesis, Texas U., 2008

[72] MINERvA Collaboration, Phys. Rev. D, 93, 11, 2016

[73] A. Bradford, A. Bodek, H. Budd and J. Arrington, Nucl. Phys. Proc. Suppl., 159, 127, 2006

[74] R. P. Feynman, M. Kislinger and F. Ravndal, Phys. Rev. D3, 2706, 1971

[75] K.S. Kuzmin and V.V. Lyubushkin and V.A. Naumov, Eur. Phys. J. C, 54, p. 517-538, 2008

[76] A. Bodek and U. K. Yang, J. Phys., G29, p. 18991906, 2003

[77] M. Gluck, E. Reya, and A. Vogt, Eur. Phys. J., C5, p. 461470, 1998

[78] R. Gran, J. Nieves, F. Sanchez and M. J. Vicente Vacas, Phys. Rev. D, 88, 2013

[79] H. Gallagher, Nucl. Phys. Proc. Suppl., 112, p. 188194, 2002

[80] T. Yang, AIP Conf Proc, 967, p. 269-275, 2007

[81] R. Brun, A.C. McPherson, P. Zanarini, M. Maire, and F. Bruyant, CERN-DD-EE-84-01, 65, 1987

[82] MINERvA Collaboration, Nucl. Instrum. Meth., 676, p. 44-49, 2012

[83] W. Fetscher and H.-J. Gerber, Particle Data Group Reviews, 2011

[84] Patrick, C., PhD Thesis, Northwestern U., 2016

[85] MINERvA Collaboration, Phys. Rev. D, 92, 9, 2015

[86] MINERvA Collaboration, Phys. Rev. Lett., 111, 2013

[87] MINERvA Collaboration, Physical Review Letters, 111, 2, 2013

[88] G. D' Agostini, Nucl. Instrum. Methods in Phys. Res. Sect. A, 362, 1995

[89] K. Hurtado, PhD Thesis, Centro Brasileiro de Pesquisas Fisicas (CBPF), 2013

[90] MINERvA Collaboration, Nucl. Instrum. Meth., A789, p.28-42, 2015